

Dottorato di Ricerca in Fisica  
XIX ciclo

Alma Mater Studiorum  
Università degli Studi di Bologna

SETTORE DISCIPLINARE: FIS/03

TESI PER IL CONSEGUIMENTO DEL  
TITOLO DI DOTTORE DI RICERCA

PHOSPHORUS ION IMPLANTATION IN  
SiC: INFLUENCE OF THE ANNEALING  
CONDITIONS ON DOPANT ACTIVATION  
AND DEFECTS

Candidata: Mariaconcetta Canino

Supervisore: Chiar.mo Prof. Anna Cavallini

Correlatore: Dott. Antonella Poggi

Coordinatore: Chiar.mo Prof. Fabio Ortolani







## Introduction

Semiconductor technology is presently dominated by silicon. The need for different semiconductors is only limited to niche applications, where the use of silicon is prevented. Such fields include high temperature operation, high power and high frequency applications, and optical emission and detection in the UV spectrum. In these fields the development and commercialization of WBG semiconductor- based devices would represent a revolution. On the other hand, switching from silicon technology to a WBG technology is still a challenge because the availability of good substrate material, the fabrication of low-resistance ohmic contacts, and the growth of good quality oxide are still unsolved problems. Furthermore, low-cost process technology, and long term reliability are mandatory for device commercialization.

Among WBG semiconductors SiC represents a promising solution because it is the only one owing a native oxide and because it was thought in the past that SiC processing technology was relatively close to the well-established Si technology. Anyway many obstacles have to be overcome for the development of SiC microelectronics. In the past years much effort was spent in the growth of defect-free material, and recently CREE commercialized zero micropipe wafers (ZMP) [w-cree]. Furthermore the main technological steps for the fabrication of every kind of device, i.e. selective doping and contact manufacturing, need further investigation. The two issues are closely related [Svensson], since, in order to have ohmic contacts with specific contact resistance below  $10^{-5} \Omega\text{cm}^2$ , doping levels of the order of  $10^{19} \text{cm}^{-3}$  are required [Choyke].

Problems related with doping by ion implantation are stoichiometric disturbances in the crystal, difficulty in restoring the lattice order, and evaporation and re-deposition of Si resulting in step bunched surfaces. The electrical activation of dopants requires high temperature post implantation annealing, which, on the other hand induces step bunching insurgence [Chen]. Furthermore, even a high temperature annealing is not completely effective in restoring the lattice, thus ion implantation is often performed at high temperature. In case of phosphorus, ion implantation temperatures around 600-700 °C are reported as mandatory [Rao]. The major drawback of performing the implantation at high temperature is that so high temperatures are not feasible in industrial ion implanters.

Step bunching negatively affects device performance. In fact, an increase of the leakage current in the gate of a MOSFET with the gate oxide grown on a step bunched surface was reported in [Capano2001]; the formation of conductive paths among n+/p diodes when a deposited oxide was used as a passivation layer was observed as well [Poggi2002]. Thus, the choice of the annealing temperature must be a compromise between the aim of achieving high electrical activation of dopants and the need to preserve the surface

smoothness. The influence of the heating ramp of the annealing cycle on surface morphology and electrical activation was also reported for Al [Poggi2006] implants, N [Raineri] implants, and N and P [Blanqué] co-implants.

Performing the annealing at low temperature could leave residual implant damage. A high concentration of defects could affect the long term stability of microelectronic devices, thus preventing their commercialization [Advances]. For example the presence of a high concentration of traps can affect the drain current of a MOSFET [Adajaye] resulting in higher threshold voltage and longer switching time [Millman]. Thus, it is important to characterize the electrically active defects in the substrate, and to determine whether they are induced or not by processing, in order to establish a process that does not introduce severe damage in the material.

In this work  $n^+/p$  diodes were manufactured and characterized by electrical measurements. A  $P^+$  ion implantation at 300 °C is proposed, since this temperature is intermediate between the high temperatures required by SiC technology, and industrial applications. The electrical activation of phosphorus and the effect of the annealing on the surface morphology were analysed for different annealing temperatures and for different heating rates.  $n^+/p$  diodes were made by combining 300°C  $P^+$  ion implantation and the most promising annealing cycle, i.e. 1300 °C for 20 minutes in argon, with a heating ramp equal to 40 °C/s. DLTS analyses were performed on the diodes and on Schottky diodes in order to study the electrically active defects in the material, either native or induced by processing.

A background to SiC is given in chapter 1. Chapter 2 describes the main issues of SiC ion implantation and annealing technology. In chapter three the process for device realization is described. Chapter 4 illustrates the experimental techniques employed in this thesis, i.e. sheet resistance measurements on Van der Pauw geometries, Scanning Capacitance Microscopy (SCM), current voltage (I-V), capacitance voltage (C-V), Deep Level Transient Spectroscopy (DLTS), and Secondary Electron Microscopy (SEM) in Electron Beam Induced Current (EBIC) mode. Results for the electrical activation of the implanted phosphorus, for the electrical performance of the diodes, and for the analyses of electrically active defects induced by the ion implantation are reported in chapter 5. Finally, conclusions are drawn.

# Summary

## 1. Silicon carbide

1.1 Lattice structure	p. 1
1.2 Defects	p. 3
1.3 Band structure and physical properties	p. 4

## 2. Ion implantation technology in SiC

2.1 ion implantation	p. 9
2.1.1 Physics of ion penetration in solids	p. 9
2.1.2 Ion distribution	p. 10
2.1.3 Simulation of ion implantation profiles	p. 12
2.2 Recovery of the ion implantation damage	p. 19
2.2.1 Hot ion implantation	p. 19
2.2.2 Annealing	p. 20

## 3. Fabrication of n<sup>+</sup>/p junctions in SiC

3.1 Starting material	p. 23
3.2 Photolithographic steps	p. 23
3.3 Fabrication of n <sup>+</sup> /p diodes	p. 25
3.3.1 Alignment marks	p. 25
3.3.2 Ion implantation	p. 25
3.3.3 Annealing	p. 26
3.3.4 Contacts	p. 27

## 4. Electrical characterizations: theory

4.1 Characterization of electrical properties of doped layers	p. 29
4.1.1 Sheet resistance	p. 29
4.1.2 Sheet resistance measurements on Van der Pauw geometries	p. 30
4.1.3 Scanning Capacitance Microscopy	p. 31
4.2 Electrical characterization of a p-n junction	p. 31
4.2.1 Properties of p-n junctions	p. 31
4.2.2 Current voltage measurements	p. 32
4.2.3 Capacitance voltage measurements	p. 39
4.3 Capacitance voltage measurements on Schottky diodes	p. 41

4.4 Characterization of electrically active defects in semiconductors:	
DLTS	p. 42
4.4.1 Physics of carrier capture and emission at a trap	p. 42
4.4.2 Majority carrier trap spectroscopy by DLTS	p. 45
4.5 Scanning Electron Microscopy	p. 48
4.5.1 Beam-sample interaction	p. 48
4.5.2 Images by secondary electrons	p. 50
4.5.3 Electron Beam Induced Current	p. 50

## **5. Electrical characterizations**

5.1 Experimental setup	p. 53
5.2 Devices and test geometries	p. 54
5.3 Dopant activation	p. 55
5.4 Electrical characterizations of the diodes with the emitter contact in nickel as deposited	p. 59
5.4.1 Current voltage measurements	p. 59
5.4.2 Capacitance voltage measurements	p. 63
5.5 Electrical characterizations of the diodes with the emitter contact in nickel silicide	p. 66
5.5.1 Effect of nickel silicide on the contact resistance	p. 66
5.5.2 Current voltage measurements	p. 68
5.5.3 Capacitance voltage measurements	p. 73
5.6 Defects introduced by the ion implantation process	p. 73

<b>Conclusions</b>	p.83
--------------------	------

<b>References</b>	p. 85
-------------------	-------

# Chapter 1

## Silicon Carbide

### 1.1 Lattice structure

Silicon carbide is made up of equal parts of silicon and carbon atoms. The unit cell is tetragonal, consisting of a carbon (silicon) atom, surrounded by four silicon (carbon) atoms at the vertices (fig. 1.1).

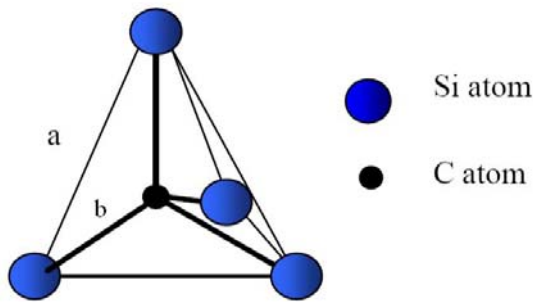


Figure 1.1. The tetragonal cell of SiC. The distance between two nearest neighbours is approximately  $3.08\text{\AA}$  (a) whereas the distance between a C atom and a Si atom is approximately  $2.52\text{\AA}$  (b).

The crystal planes are made up of a silicon atom and a carbon atom in the center and on the vertices of a hexagon. This structure is labeled A, and the upper plane can be oriented like B or C as explained in fig. 1.2.

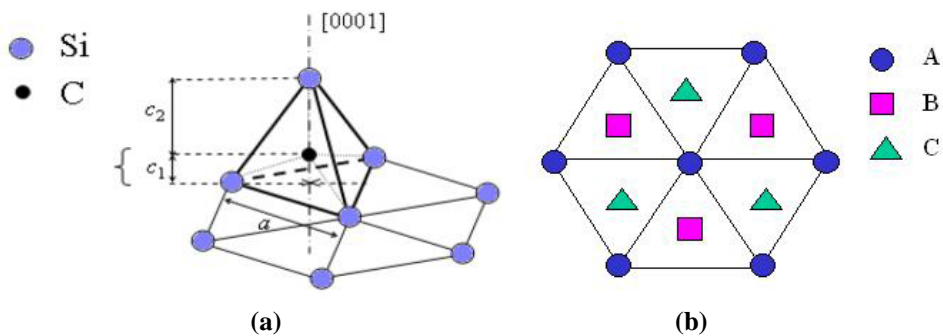
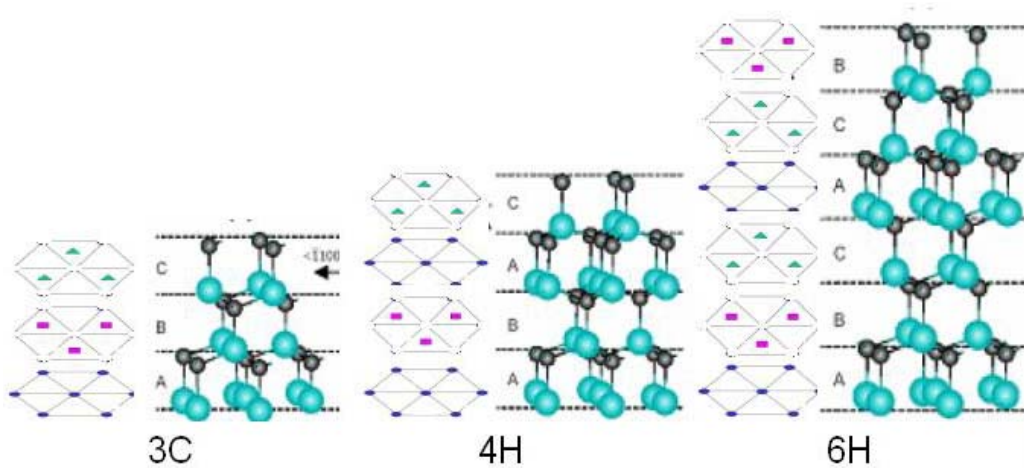


Figure 1.2. Disposition of the tetrahedral cell in the hexagonal plane (a) and possible combinations of the hexagonal planes.

SiC exists in more than 300 crystal structures, the so-called polytypes, which differ for the stacking sequence of the crystal planes. The stacking sequence of the crystal planes is codified through the Ramsdell notation: each sequence is labeled by a number, which represents the number of crystal planes in the periodic structure, and a letter, H, C, or R, indicating the lattice structure: H means hexagonal, C cubic, and R rhombohedral. In fig. 1.3 the stacking sequences of the 3C-, 4H-, and 6H- polytypes are shown. Among SiC polytypes, these are the most studied for device applications.



**Figure 1.3.** The stacking sequences of 3C-, 4H-, and 6H-SiC.

Each site can be defined as hexagonal or cubic depending on the symmetry of the neighbouring atoms (fig. 1.4). This inequivalence of lattice sites leads also to different energy levels of substitutional impurities, whether they occupy hexagonal or cubic sites.

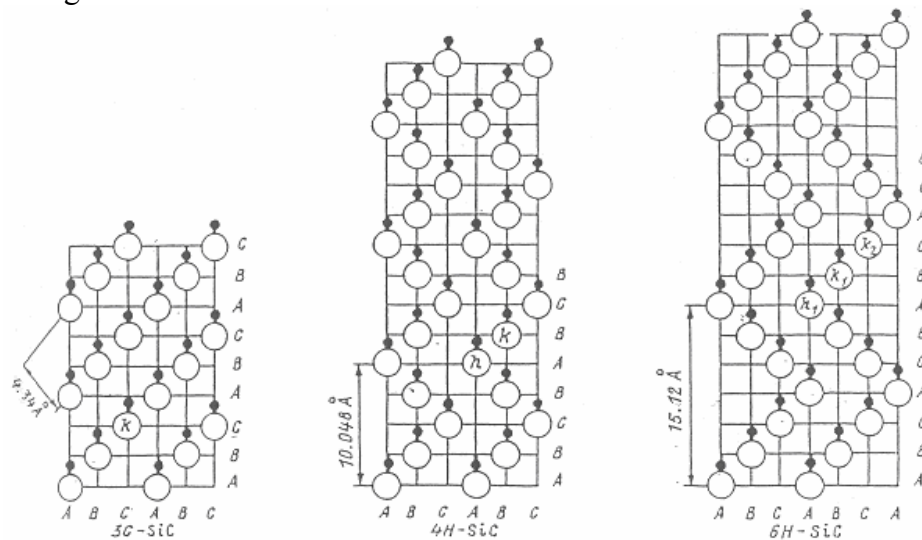


**Figure 1.4.** The stacking sequence of SiC lattice planes: hexagonal and cubic sites.

## 1.2 Defects

A defect is a portion of material featured by deviations from the ideal lattice structure. We can identify point defects, 2- dimensional defects (dislocations), and 3-dimensional defects.

Point defects can be vacancies, i.e. the absence of an atom at its lattice site, interstitial, i.e. the presence of an atom outside in a site that should be unoccupied. In biatomic crystals, like SiC, antisites, i.e. a Si (C) atom in the C (Si) sublattice, can also exist. Impurities can be observed when an atom of a different species is present in the lattice, either in substitutional or in interstitial position.

Line defects, also called dislocations, are observed when the periodicity of the lattice is broken along a line. Two types of dislocations exist: edge and screw dislocations (fig. 1.5). Edge dislocations can be schematically considered as the removal of a portion of a lattice plane, screw dislocations as a shift of a crystal plane in a direction parallel to the dislocation line.

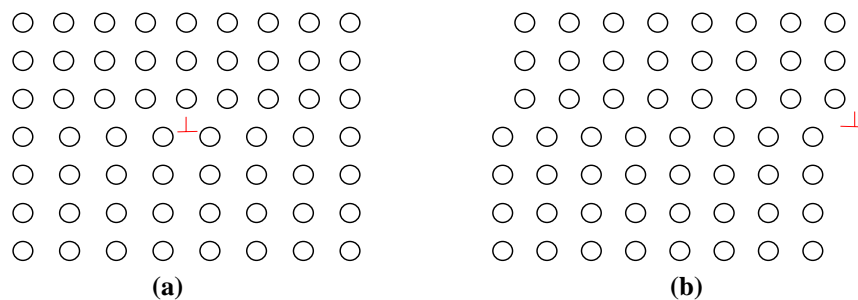


**Figure 1.5. Representation of edge (a) and screw (b) dislocations. The red symbols indicate the dislocation line.**

The amount of distortion can be expressed through the Burgers vector  $\mathbf{B}$ . In the case of edge dislocations  $\mathbf{B}$  is perpendicular to the dislocation line, whereas in the case of screw dislocations  $\mathbf{B}$  is parallel to the dislocation line and its length corresponds to the step height of the dislocation. It has been observed that if  $\mathbf{B} > 3c$  the dislocation forms an open core along the dislocation line. This kind of defect, labeled micropipe, is particularly detrimental for the operation of SiC devices. The progress in crystal growth has brought to a drastic reduction in micropipe density, leading to the commercialization of zero micropipe density [w-cree].

Among 2-dimentional defects that can affect SiC devices, stacking faults are worth a mention. Stacking faults are crystal planes where the stacking sequence of the lattice is broken. In the upper and in the lower regions the lattice is perfect. Stacking faults have been observed to be responsible of the increase of the forward voltage drop of SiC PiN diodes.

Complex defects can be clusters of defects, for example clusters of vacancies, interstitials, or impurities. They can be introduced during epitaxial growth or processing. Each kind of defect has an equilibrium concentration that depends on temperature and on the defect itself:

$$N_T = A \exp(-E_a / kT) \quad (1.1).$$

During the growth (at high temperature) a high quantity of impurities can be introduced. After cooling their solubility decreases and as a result precipitates are formed. Processing can induce the formation of clusters of vacancies and interstitials. For example, a heavy ion implantation process creates a high quantity of point defects in the crystal, and after annealing precipitates can be formed [Ohno].

### 1.3 Band structure and physical properties

Despite technological inconvenience, such as the lack of defect free material and the difficulties still present in processing, SiC is characterized by interesting physical and electrical properties.

The band structure of SiC depends on the polytype. In table 1.1 some properties of SiC, Si [Harris] and other WBG materials [Peréz] are reported.

**Table 1.1. Physical and electrical properties of 3C-SiC, 4H-SiC, and 6H-SiC. The properties of Si, GaN and C are reported for comparison.**

Material	3C-SiC	4H-SiC	6H-SiC	Si	GaN	C
Band gap $E_g$ (eV)	2.4	3.26	3.03	1.12	3.39	5.45
Intrinsic carrier concentration $n_i$ (cm <sup>-3</sup> ) @ 300 K	6.9	$8.2 \times 10^{-9}$	$2.3 \times 10^{-6}$	$1.5 \times 10^{10}$	$1.6 \times 10^{-10}$	$1.6 \times 10^{-27}$
Relative dielectric strength $\epsilon$	9.72	9.66	9.66	11.7	9	5.50
Critical electric field $E_{crit}$ (MV/cm) @ $N_d = 10^{17} \text{cm}^{-3}$	2	2.5	2.4	0.6	3.3	5.6
Drift saturation velocity $v_{sat}$ (cm/s)	$2.5 \times 10^7$	$2 \times 10^7$	$2 \times 10^7$	$10^7$	$2.5 \times 10^7$	$2.7 \times 10^7$
Electron mobility $\mu_e$ (cm <sup>2</sup> /Vs) @ $N_d = 10^{16} \text{cm}^{-3}$	750	800	400	1200	1000	1900
Hole mobility $\mu_p$ (cm <sup>2</sup> /Vs) @ $N_d = 10^{16} \text{cm}^{-3}$	40	115	90	420	<850	1600
Thermal conductivity $\kappa$ (W/cmK)	5.0	4.9	4.9	1.5	1.3	20

Some of these properties vary as a function of temperature and of the doping density.

The band gap amplitude decreases as temperature increases, due to increase of the amplitude of the thermal vibrations of the atoms of the lattice. The interatomic distance increases and the potential in the Schrödinger equation decreases. This results in an enlargement of the bands and thus the value of the band gap decreases. The dependence is given by:

$$E_g(T) = E_g(300) + \alpha \left( \frac{300^2}{300 + \beta} - \frac{T^2}{T + \beta} \right) \quad (1.2)$$

where  $\alpha$  and  $\beta$  are equal to  $3.3 \times 10^{-3}$  and 0 for 6H- and 4H-SiC [Sze, Sze-2, Bakowski].

The intrinsic carrier concentration depends on the temperature and on the band gap:

$$n_i^2 = N_C N_V T^3 \exp(-E_g/kT) \quad (1.3)$$

where  $N_C$  and  $N_V$  are the densities of states in the conduction band and in the valence band, given by:

$$N_C = 2 \left( \frac{2m_e^* kT}{\hbar^2} \right)^{3/2} \quad (1.4a)$$

and

$$N_V = 2 \left( \frac{2m_h^* kT}{\hbar^2} \right)^{3/2} . \quad (1.4b)$$

Intrinsic carrier concentration is one of the limiting factors of microelectronic devices operation. Wide band gap semiconductors are advantageous because of their capability of operation at higher temperatures than Si. In Si the intrinsic carrier concentration becomes comparable to the doping concentration at about 150°C. In SiC this phenomenon occurs at 900°C. This means that the maximum operating temperature of SiC based devices is not imposed by material properties, but by technological issues, such as contact fabrication or packaging.

In contrast, one of the disadvantages of SiC, and of WBG semiconductors in general, is due to the fact that the electronic levels of the doping species are not as shallow as in Si. This implies that at room temperature only a fraction of the dopants is ionized, *i.e.* the free carrier concentration,  $n$  or  $p$ , is lower than the doping concentration.

The fraction of ionised donors  $N_D^+$  with respect to the total number of electrically active donors can be calculated by considering the neutrality equation

$$n = N_D^+ + p \quad (1.5)$$

and the Boltzmann relation

$$n = N_C \exp\left(-\frac{E_C - E_F}{kT}\right), \quad (1.6)$$

where  $n$  is the free carrier concentration,  $p$  is the hole concentration,  $N_C$  is the density of states in the conduction band,  $E_C - E_F$  the distance of the Fermi level from the conduction band and  $T$  is the temperature.

In a non compensated a n-type material the hole concentration is very small, thus

$$n = N_D \left( 1 - \frac{1}{1 + \frac{1}{g} \exp\left(\frac{E_D - E_F}{kT}\right)} \right). \quad (1.7)$$

The fraction of ionised donors with respect to the total number of electrically active donors is given by

$$\frac{n}{N_D} = \frac{-1 + \sqrt{1 + 4 \frac{gN_D}{N_C} \exp\left(\frac{E_C - E_D}{kT}\right)}}{2 \frac{gN_D}{N_C} \exp\left(\frac{E_C - E_D}{kT}\right)}. \quad (1.8a)$$

A similar relationship can be obtained for acceptors [Ruff]

$$\frac{p}{N_A} = \frac{-1 + \sqrt{1 + 4 \frac{gN_A}{N_V} \exp\left(\frac{E_A - E_V}{kT}\right)}}{2 \frac{gN_A}{N_V} \exp\left(\frac{E_A - E_V}{kT}\right)}. \quad (1.8b)$$

This model takes into account only one ionisation level and is valid in the approximation of low compensation and up to concentrations lower than to  $10^{19} \text{cm}^{-3}$  because at higher concentration the degenerate regime is reached and the Boltzmann statistics is no longer valid.

**Table 1.2. Energetic levels of Al, B, N, and P, in 4H-, and 6H-SiC. The labels *h* and *k* refer to hexagonal and cubic sites, respectively.**

SiC polytype	E(Al)-E <sub>V</sub> (meV)	E(B)-E <sub>V</sub> (meV)	E(N)-E <sub>V</sub> (meV)	E(P)-E <sub>V</sub> (meV)
4H	190	300	42 (h) 82 (k)	53 (h) 93 (k)
6H	225	310	82(h) 137 (k)	82 (h) 115 (k)

In table 1.2 the energetic levels of some of the most common doping species are reported for the 4H-, and 6H- polytypes.

The breakdown field in SiC is around 5x higher than in silicon. This is critical for power switching devices, since the specific on-resistance scales inversely as the cube of the breakdown field. Thus, SiC power devices are expected to have specific on-resistances 100 – 150 times lower than comparable silicon devices [Purdue]. The critical electric field is also crucial for high blocking voltage devices (cfr eq. 4.6 ).

SiC devices can operate at high frequencies (RF and microwave) because of the high saturated electron drift velocity of SiC allows high frequency device application, like RF and microwave [w-cree].

The free carrier mobility is limited by the scattering with the fixed ions of the lattice. Since impurities act as scattering centres, the mobility decreases as a function of doping, according to the law [Bakowski, Arora, Schaffer, Schaffer-2]:

$$\mu_{n,p} = \mu_{n,p,\min} + \frac{\mu_{n,p,\max}}{1 + \left( \frac{N_D + N_A}{N_{n,p,\text{ref}}} \right)^{\gamma_{n,p}}} \left( \frac{T}{300} \right)^{\alpha_{n,p}} \quad (1.9)$$

where  $\mu_{n,p,\min}$ ,  $\mu_{n,p,\max}$ ,  $\alpha_{n,p}$ ,  $\gamma_{n,p}$ ,  $N_{n,p,\text{ref}}$  are characteristic parameters of the material. In table 1.3 their values are reported for 4H- and 6H-SiC and for Si. Electrons show higher mobility than holes because of their lower effective mass [w-colorado].

**Table 1.3. Parameters that rule the mobility in Si, 4H- and 6H-SiC [Arora].**

	Si	6H-SiC		4H-SiC	
		⊥ to c-axis	to c-axis	⊥ to c-axis	to c-axis
		μ[1-100]	μ[1000]	μ[11-20]	μ[1000]
μ <sub>n,min</sub> cm <sup>2</sup> /Vs	92	0	0	0	0
μ <sub>n,max</sub> cm <sup>2</sup> /Vs	1268	415	87	947	1136
N <sub>n,ref</sub> cm <sup>-3</sup>	1.3 x 10 <sup>17</sup>	1.1 x 10 <sup>18</sup>	1.1 x 10 <sup>18</sup>	1.94 x 10 <sup>17</sup>	1.94 x 10 <sup>17</sup>
γ <sub>n</sub>	0.91	0.59	0.59	0.61	0.61
α <sub>n</sub>	-2.2	-3	-3	-2.15	-2.0
μ <sub>p,min</sub> cm <sup>2</sup> /Vs	52	6.8	6.8	15.9	15.9
μ <sub>p,max</sub> cm <sup>2</sup> /Vs	453	99	99	124	124
N <sub>p,ref</sub> cm <sup>-3</sup>	1.9x 10 <sup>17</sup>	2.1 x 10 <sup>19</sup>	2.1 x 10 <sup>19</sup>	1.76 x 10 <sup>19</sup>	1.76 x 10 <sup>19</sup>
γ <sub>p</sub>	0.63	0.31	0.31	0.34	0.34
α <sub>p</sub>	-2.2	-3	-3	-2.15	-2.15



## Chapter 2

### Ion implantation technology in SiC

The fabrication of devices for commercial use needs the presence of differently doped regions in the material. The only way to achieve selective doping in SiC is ion implantation, due to the extremely high temperatures needed to have diffusion of most dopant impurities in SiC. Since ion beams are employed to modify the chemical or electrical properties of the material, a high amount of damage is created. Lattice recovery takes place during the high temperature annealing treatment performed to electrically activate the dopants. In this section the technological aspects of ion implantation and annealing are examined.

#### 2.1 Ion implantation

##### *2.1.1 Physics of ion penetration in solids*

When penetrating into a solid, an ion loses its energy through a series of collisions with the atoms and the electrons of the target. The stopping power of the target material is the spatial rate of energy loss of incident ions, and is due to two contributions, the nuclear stopping power and the electronic stopping power. The first is due to collisions between the incident ion and the nuclei of the target, in which the ion transfers part of its energy to the nuclei of the target, inducing their displacement. This contribution is thus closely related with the implantation damage. The electronic contribution is due to the energy transferred by the ion to the target electrons, which results in excitation or ionization of the target atoms, or excitation of conduction or valence band electrons. Nuclear collisions predominate in case of heavy ions incident with low energy, electronic collisions in case of incidence of very energetic light ions. In fig. 2.1 the dependence of the two interactions on the incident ion velocity is shown.

Since in ion implantation processes of crystalline solids the wafer is oriented in order to avoid channelling of the incident beam, simulations for the ion stopping are made by considering amorphous solids [Wong].

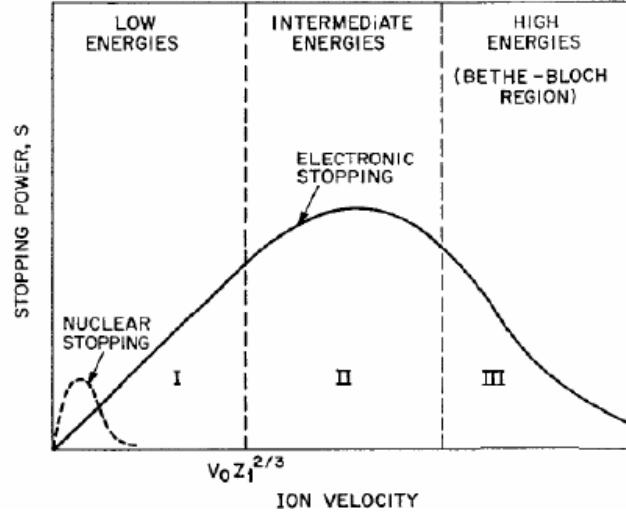


Figure 2.1. Nuclear and electronic stopping power vs incident ion velocity.  $V_0$  is the Bohr velocity ( $V_0 = q^2 / (4\pi\epsilon_0\hbar)$ ) and  $Z_1$  is the atomic number of the incident ion.

### 2.1.2 Ion distribution

The implantation process involves a huge number of events statistical concepts can be used to describe the final distribution of the implanted atoms. The range of an ion is the total distance that the atom travels before coming to rest. Actually the projected range, i.e. the total path length along the direction of incidence, is the quantity of interest. In fig. 2.2 a three-dimensional representation of ion penetration in a solid is shown. The ion enters the solid at the point (0,0,0) at an angle  $\alpha$  to the surface normal. It is then stopped at the position  $(x_s, y_s, z_s)$ . The range is labelled  $R$ , the projected range  $R_p$ . In the case of fig. 2.2, since the incident ion is not normal to the surface, we can define also the depth of penetration  $x_s$ , i.e. the perpendicular distance from the surface where the ion comes to rest.

The mean projected range is the most probable location for an ion to come to a rest:

$$R_p = \sum_i x_i / N \quad (2.1)$$

where  $x_i$  is the projected range of the  $i$ -th ion, and  $N$  is the total number of implanted ions.  $R_p$  is also referred to as the first momentum of the ion distribution.

The average fluctuation, i.e. the second momentum of the ion distribution, (the square root of the standard deviation from the mean projected range) is labelled "straggling".

$$\sigma = \left[ \frac{\sum_i (x_i - R_p)^2}{N} \right]^{1/2} \quad (2.2)$$

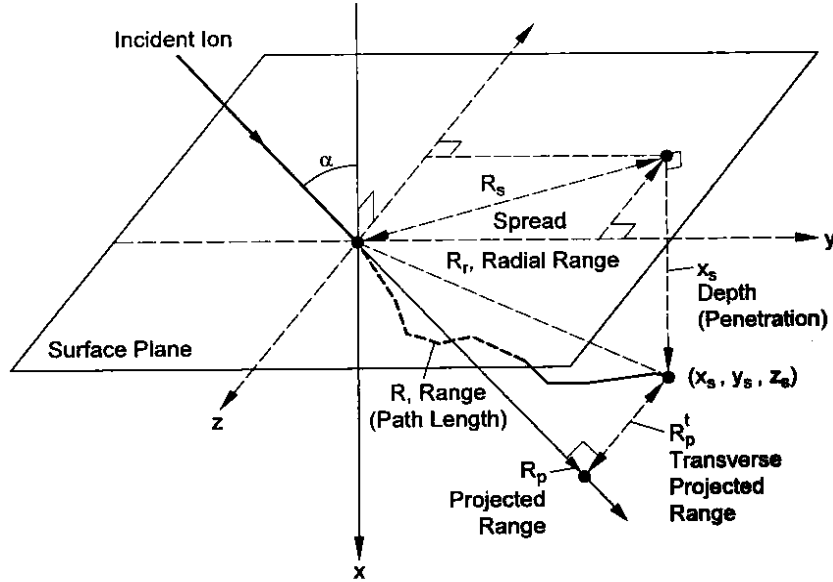


Figure 2.2. Schematic drawing for the definition of depth, projected range and path length of an incident ion [Eckstein1991].

The third and fourth moments of the ion distribution are calculated as follows:

$$\gamma = \frac{\sum_i (x_i - R_p)^3}{N\sigma^3} \quad (2.3)$$

$$\beta = \frac{\sum_i (x_i - R_p)^4}{N\sigma^4} \quad (2.4)$$

The skewness  $\gamma$  (eq. 2.3) indicates the symmetry of the distribution with respect to the Gaussian distribution:  $\gamma > 0$  indicates that the peak is closer to the surface,  $\gamma < 0$  indicates that the peak is far from the surface. Kurtosis  $\beta$  (eq. 2.4) indicates the extent of the distribution tails:  $\beta = 3$  indicates Gaussian distribution,  $0 < \beta < 3$  indicates abbreviated distribution, and  $\beta > 3$  indicates broad tails.

In fig. 2.3 the depth distributions of  $^4\text{He}$  implanted in Ni at three different energies are shown. The values of the skewness and kurtosis for the three distributions are: 0.1 keV  $\gamma = 0.8$ ,  $\beta = 3.4$ ; 10 keV  $\gamma = 0.1$ ,  $\beta = 2.5$ ; 1 MeV  $\gamma = -4.3$ ,  $\beta = 42.7$ .

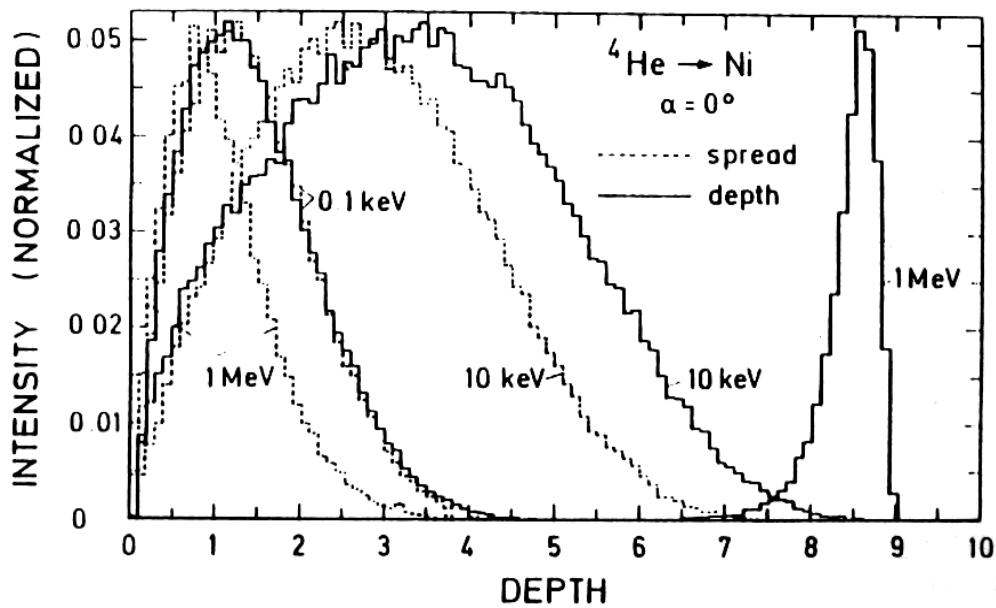


Figure 2.3 . Depth and spread distributions of He implanted in Ni at 0.1 keV, 10 keV and 1 MeV [Eckstein1991].

### 2.1.3 Simulation of ion implantation profiles

The accurate simulation of ion implanted profiles is one of the key issues in SiC ion implantation technology.

A calculation of implantation distributions can be made either by running computer programs which perform Monte Carlo simulations of the ion ranges, or by calculating the ion distribution functions using fitting parameters extracted from a database.

The first method makes use of physical models of the ion stopping process. The understanding of the physical mechanisms which regulate the energy loss of ions penetrating in solids is of crucial importance in controlling the depth profile of implanted dopant atoms and in determining the nature of lattice disorder in ion implanted solids as well. A transport calculation was developed in detail by Ziegler and Biersack [Ziegler1985] in the PRAL (Projected Range ALgorithm) code, which is part of the SRIM software package (The Stopping Ions and Ranges in Matter) [w-srim]. This kind of approach allows the calculations of a series of histories, which means that the paths of the ions in the target material are followed. Atom recoils and sputtering are taken into account as well, providing an evaluation of the implantation damage. Another advantage is that the implantation can be simulated for a wide range of targets, including composite materials and layered structures [Ziegler1985, Ziegler1992].

Fig. 2.4 shows 20 ion paths from SRIM Monte Carlo calculations for 100 keV P atoms in SiC, and the ion recoils generated by the nuclear collisions. It is possible to appreciate that the ion paths are irregular, due to the random nature of nuclear scattering.

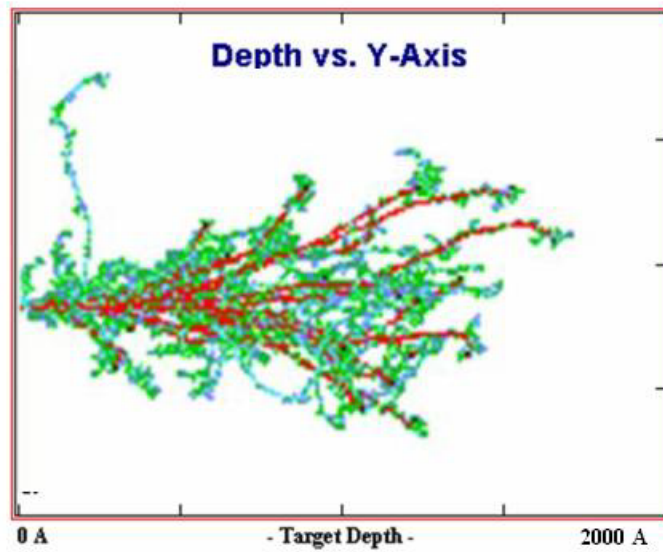


Figure 2.4. The paths of 20 P atoms implanted at 100 keV into SiC (red lines) and the atom recoils induced by the nuclear collisions of the P ions in the SiC lattice.

Fig. 2.5 shows the ion distribution obtained from the statistics of 15000, 45000 and 90000 ion histories.

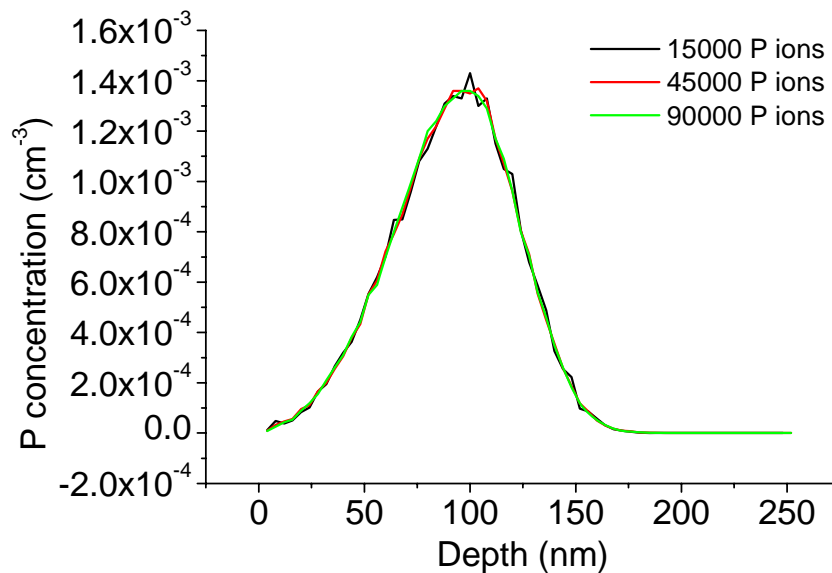


Figure 2.5. Ion implantation distribution for 100 keV P ions implanted in SiC. The profiles have been obtained with the SRIM Monte Carlo calculation following 15000 (black line), 45000 (red line) and 90000 histories (green line).

```

*****
Calculation using SRIM-2006
SRIM version ---> SRIM-2006.02
Calc. date ---> dicembre 13, 2006
*****

Disk File Name = SRIM outputs\Phosphorus in SiC

Ion = Phosphorus [15] , Mass = 30.974 amu

Target Density = 3.2100E+00 g/cm3 = 9.6419E+22 atoms/cm3
***** Target Composition *****
Atom   Atom   Atomic   Mass
Name   Numb   Percent  Percent
-----
  Si    14     050.00   070.05
  C     6      050.00   029.95
*****
Bragg Correction = 0.00%
Stopping Units = Mev / (mg/cm2)
See bottom of Table for other Stopping units

  Ion      dE/dx      dE/dx      Projected   Longitudinal   Lateral
Energy    Elec.      Nuclear    Range       Straggling     Straggling
-----
 10.00 keV 4.969E-01 2.170E+00   111 A       47 A           35 A
 20.00 keV 7.027E-01 2.165E+00   197 A       78 A           57 A
 30.00 keV 8.606E-01 2.079E+00   282 A      106 A           77 A
 40.00 keV 9.937E-01 1.981E+00   368 A      132 A           96 A
 50.00 keV 1.111E+00 1.888E+00   454 A      157 A          115 A
 60.00 keV 1.217E+00 1.801E+00   540 A      181 A          133 A
 70.00 keV 1.321E+00 1.722E+00   626 A      205 A          151 A
 80.00 keV 1.432E+00 1.650E+00   713 A      227 A          169 A
 90.00 keV 1.540E+00 1.585E+00   798 A      248 A          186 A
100.00 keV 1.639E+00 1.525E+00   884 A      267 A          203 A
110.00 keV 1.730E+00 1.470E+00   968 A      287 A          220 A
120.00 keV 1.814E+00 1.420E+00  1052 A      305 A          236 A
130.00 keV 1.892E+00 1.373E+00  1136 A      322 A          252 A
140.00 keV 1.964E+00 1.330E+00  1220 A      339 A          268 A
150.00 keV 2.031E+00 1.290E+00  1303 A      356 A          283 A
160.00 keV 2.094E+00 1.253E+00  1385 A      371 A          298 A
170.00 keV 2.152E+00 1.218E+00  1468 A      387 A          313 A
180.00 keV 2.207E+00 1.186E+00  1550 A      401 A          328 A
200.00 keV 2.309E+00 1.126E+00  1713 A      430 A          356 A
-----
Multiply Stopping by      for Stopping units
-----
3.2099E+01      eV / Angstrom
3.2099E+02      keV / micron
3.2099E+02      Mev / mm
1.0000E+00      keV / (ug/cm2)
1.0000E+00      Mev / (mg/cm2)
1.0000E+03      keV / (mg/cm2)
3.3291E+01      eV / (1E15 atoms/cm2)
1.4149E-01      L.S.S. reduced units
-----
(C) 1984,1989,1992,1998,2006 by J.P. Biersack and J.F. Ziegler

```

Figure 2.6. SRIM output text file for analytically derived stopping power, projected range and straggling of a P ion implanted in SiC.

As one can notice from fig. 2.6, SRIM calculates only the projected range and the straggling. The second and third moments of the distributions are not calculated. Moreover SRIM is time-consuming, since, as one can understand

from fig. 2.5, a wide number of ion histories is needed to generate a profile not affected by noise.

A faster approach allowed by the SRIM software is to calculate the first two moments of the ion distribution as a function of the incident ion energy and of the nuclear and electronic stopping power of the target. As an example a SRIM output file for analytically derived results is given in fig. 2.6 for a 100 keV P ion implanted into SiC. From these parameters one can calculate the ion distribution. There's a basic difference between the SRIM analytically derived parameters for the ion distribution and the parameters of the distribution extracted by fitting a SIMS profile: the former are derived by using a physical model [Ziegler1985], whereas the latter are calculated from experimental data.

The alternative way of simulating ion implantation profiles is convenient since the profiles generated are as accurate as the experimental data and it is faster once the database has been created. Since in SiC diffusion of species during the annealing does not take place, ion implantation processes are often multiple, i.e. the several ion energies and doses are employed, in order to obtain a flat profile of the implanted species. Thus, a faster simulation approach is convenient in case of SiC because of the complicated implantation schedules required.

The most common distribution functions used for describing ion implantation profiles are the ones of the Pearson family [Ashworth1990]. The ion implantation profiles into crystalline materials in random direction are best described by the Pearson IV distribution:

$$P_{IV} = \frac{1}{M} \exp\left[-n \arctan\left(\frac{x - R_p}{A} - \frac{n}{r}\right)\right] \times \left[1 + \left(\frac{x - R_p}{A} - \frac{n}{r}\right)^2\right]^{-m} \quad (2.5)$$

where

$$r = -\left(2 + \frac{1}{B_2}\right) \quad (2.6)$$

$$n = -ra(4B_0B_2 - a^2)^{-1/2} \quad (2.7)$$

$$m = -1/2B_2 \quad (2.8)$$

$$A = mra/n \quad (2.9)$$

$$a = \Delta R_p \gamma (\beta + 3) C \quad (2.10)$$

$$B_0 = -\Delta R_p^2 (4\beta - 3\gamma^2) C \quad (2.11)$$

$$B_2 = -(2\beta - 3\gamma^2 - 6) C \quad (2.12)$$

$$C = \frac{1}{2(5\beta - 6\gamma^2 - 9)}. \quad (2.13)$$

The expression 2.5 corresponds to a Pearson IV distribution when  $0 < \gamma^2 < 32$  and  $\beta > \beta_0$  where  $\beta_0$  is defined by:

$$\beta_0 = \frac{48 + 39\gamma^2 + 6(\gamma^2 + 4)^{1.5}}{32 - \gamma^2} \quad (2.14)$$

There are two ways to calculate a profile from the knowledge of the moments of its distribution. One is to create a database of all extracted moments from which the moments for a desired energy can be extrapolated, the other is to fit appropriate analytical function to the data and tabulate the parameters obtained from the fitting. Janson *et al.* [Janson2003] chose the second approach. They determined the energy dependence of the first four moments of ion implanted profile distributions by analysing a wide number of SIMS profiles and literature data in 4H- and 6H-SiC. They obtained the following fitting functions for the energy dependence of the distribution moments:

$$R_p = a_1 E_r^{a_2} E_r^{a_3 \ln E_r} E_r^{a_4 (\ln E_r)^2} \quad (2.15)$$

$$\Delta R_p = \frac{b_1}{1 + (b_2 / E)^{b_3}} \quad (2.16)$$

$$\gamma = (c_1 - c_2 \sqrt{E}) \exp\left(-\frac{E}{c_4}\right) - c_3 \exp\left(-\frac{c_4}{E}\right) \quad (2.17)$$

$$\beta = \left(d_1 + 2.5e^{-d_2/E}\right) \beta_0 \quad (2.18)$$

where  $E_r$  is the energy value (expressed in keV),  $\beta_0$  is defined by eq. 2.14, and the values of the fitting parameters are given in table 2.2 for several ions.

**Table 2.2. Least square fit parameters of Eqs. 2.15, 2.16, 2.17, and 2.18 to the distribution moments  $R_p$ ,  $\Delta R_p$ ,  $\gamma$  and  $\beta$  of the experimental and simulated implantation in Janson's study [Janson2003]**

<b>Ion</b>	$a_1$ (nm)	$a_2$	$a_3$ ( $10^{-3}$ )	$a_4$ ( $10^{-3}$ )	$b_1$ (nm)	$b_2$ (keV)	$b_3$	$c_1$	$c_2$ (keV $^{-1/2}$ )	$c_3$	$c_4$ (keV)	$d_1$	$d_2$ (keV)
$^1\text{H}$	16.3	0.76	38.3	7.1	61	5.6	0.99	1.24	1.35	1.4	21	1.4	$\infty$
$^2\text{H}$	16.4	0.85	38.9	8.1	105	11.4	0.96	0.26	0.44	1.3	151	1.5	241
$^7\text{Li}$	3.79	1.12	-27.8	0.3	120	43.4	1.07	1.26	0.44	0.1	245	1.5	10
$^{11}\text{B}$	1.39	1.53	-119	-5.7	124	116	0.76	-0.09	0.06	1.9	83	1.5	519
$^{14}\text{N}$	1.23	1.17	-26.0	0.6	147	297	0.84	-1.21	-0.04	2.8	109	1.5	269
$^{16}\text{O}$	3.47	0.62	72.6	6.5	120	108	1.07	1.62	0.32	0.9	692	1.5	15
$^{27}\text{Al}$	3.34	0.42	113.6	8.4	239	484	0.88	1.76	0.16	2.2	858	1.5	126
$^{31}\text{P}$	1.43	0.74	72.8	6.8	188	411	0.97	0.86	0.02	1.4	476	1.2	$\infty$
$^{69}\text{Ga}$	5.60	0.01	122.2	4.1	774	3220	1.11	1.00	0.02	0.0	190	1.1	$\infty$
$^{75}\text{As}$	0.84	1.15	-84.6	-7.3	1890	15200	0.87	3.60	0.08	0.7	392	1.1	$\infty$

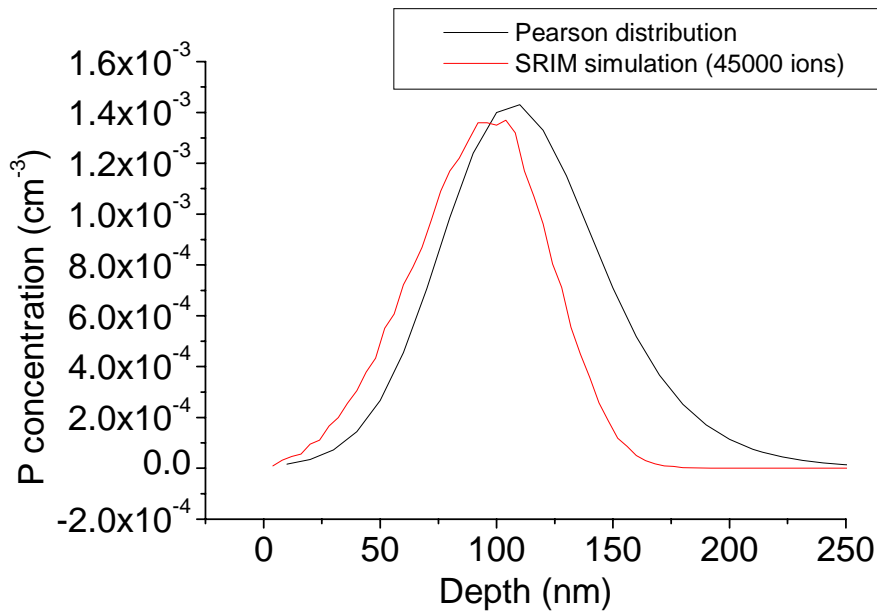


**Figure 2.7. Distributions of 100 keV P ions in SiC obtained by calculation of the Pearson IV distribution (black line) and by SRIM Monte Carlo calculation (red line).**

In this way the distribution of various implanted species can be calculated a-priori. The validity of such calculation has a lower energy limit since the simulated profiles are reliable when the Pearson distribution is not significantly curtailed by the surface [Ashworth1990].

As an example the calculation of the distribution of 100 keV P ions is reported in fig. 2.7. The profile generated by SRIM is reported for comparison.

The differences in the two simulated profiles can be ascribed to some uncertainties that both approaches have. In SRIM the nuclear stopping power is calculated on the basis of a universal potential [Ziegler 1985], obtained by the fitting of experimental values for several targets; the electronic stopping power is a rather complicated function of the incident ion mass, velocity and ionization; the stopping power values obtained for monoatomic targets are tabulated and the values of stopping power for composite targets, like SiC, are obtained analytically by taking into account the stoichiometry and density of the material. In the analytical approach possible error sources can reside in the determination of the SIMS profiles in SiC, in the fitting of the SIMS profiles to obtain the Pearson distribution parameters, and in the fitting of the parameters to obtain their energy dependence. Anyway the position of the peak of the distribution and the straggling yielded by both methods are comparable.

In this thesis the simulation of ion implantation profiles has been achieved with both methods. The data obtained by Janson *et al.*, have been used to create a generator of Pearson distributions.

## 2.2 Recovery of the ion implantation damage

The ion bombardment leaves some damage in the solid: the formation of primary defects, like vacancies, interstitials, antisites and Frenkel pairs, are the product of the ion cascade. The maximum damage distribution lies closer to the surface than the dopant distribution. It was demonstrated by Monte Carlo calculations that a vacancy rich region is extending closer to the surface, whereas an interstitial rich region is extending between  $R_p$  and  $2R_p$ . Moreover, after implantation the implanted atoms are not electrically active since they occupy interstitial positions. A post implantation thermal treatment is required in order to restore the lattice quality and to electrically activate the dopants [Bentini, Capano].

The main acceptor species in SiC are aluminum and boron. Aluminum is generally preferred because the level that it introduces has lower ionization energy with respect to boron, whereas boron is preferred in case of deep implants because of its lower atomic mass.

The main donor dopants in SiC are nitrogen and phosphorus. They have similar ionization energy. Nitrogen was in former times the favourite choice due to its lower atomic mass, that creates a lower amount of damage. Phosphorus has recently been preferred due to the higher electrical activation that can be achieved even with a low-temperature annealing.

### 2.2.1 Hot ion implantation

Problems of SiC ion-implantation technology include [Rao]: 1) incongruent evaporation of Si from SiC wafer during post-implantation annealing; 2) stoichiometric disturbances caused by ion-implantation; 3) difficulty in restoring the lattice. These problems result in poor implant electrical activation. Some of these problems are minimized by performing ion implantation at an elevated temperature. When ion implantation is carried out at high temperature defect migration is more likely and crystallization is enhanced [Ziegler 1992]. The crystal quality of a solid can be evaluated by RBS-C. In fig. 2.8 a comparison between the damage introduced by a room temperature  $P^+$  ion implantation and by a  $800^\circ\text{C}$  implantation is shown after annealing at  $1700^\circ\text{C}$  for 30 minutes in argon [Negoro].

The room temperature ion implantation process creates a nearly amorphous layer. Severe damage persists even after a  $1700^\circ\text{C}$  annealing. In the case of hot ion implantation the same annealing at  $1700^\circ\text{C}$  restores the lattice order to the virgin value. This trend is in accordance with the results obtained for other implanted species [Lazar, Inoue]. Phosphorus ion implantation is always performed at temperatures higher than  $500\text{-}600^\circ\text{C}$  [Rao]. Since most industrial implanters are not geared for implantation at so high a temperature, it is interesting to study the properties of P doped layer implanted at lower temperature.

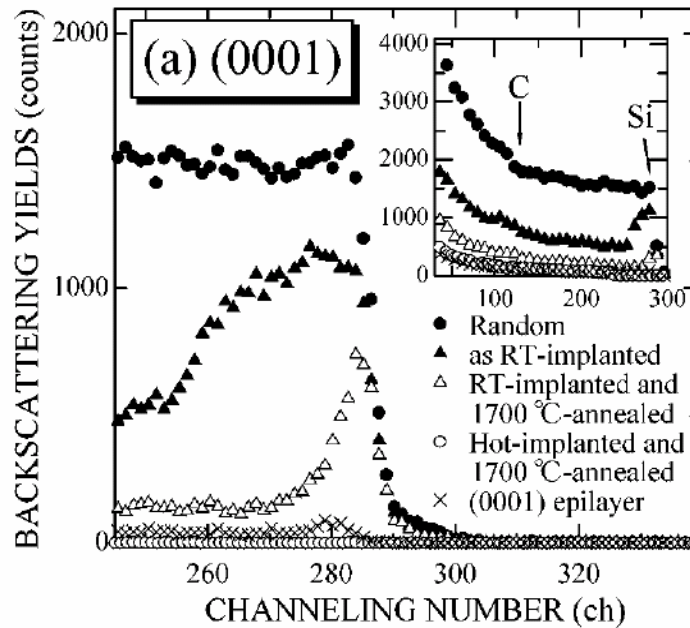
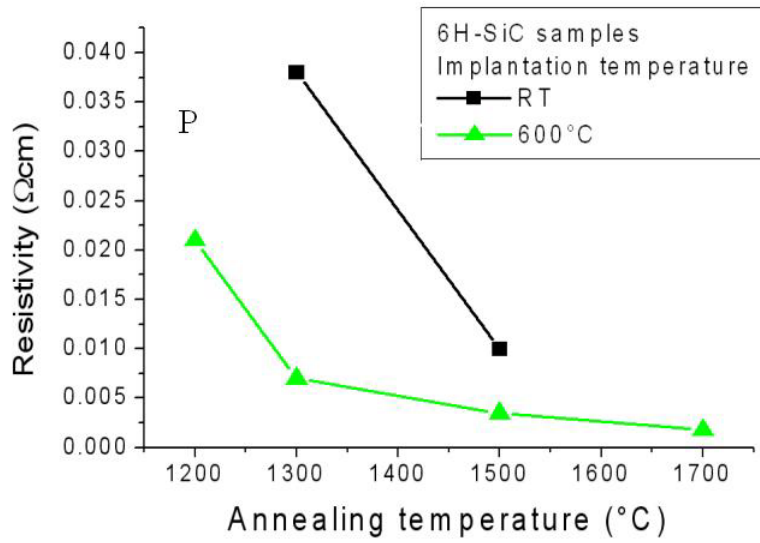


Figure 2.8. RBS-C spectra of P+ implanted samples at room temperature and at 800 °C.

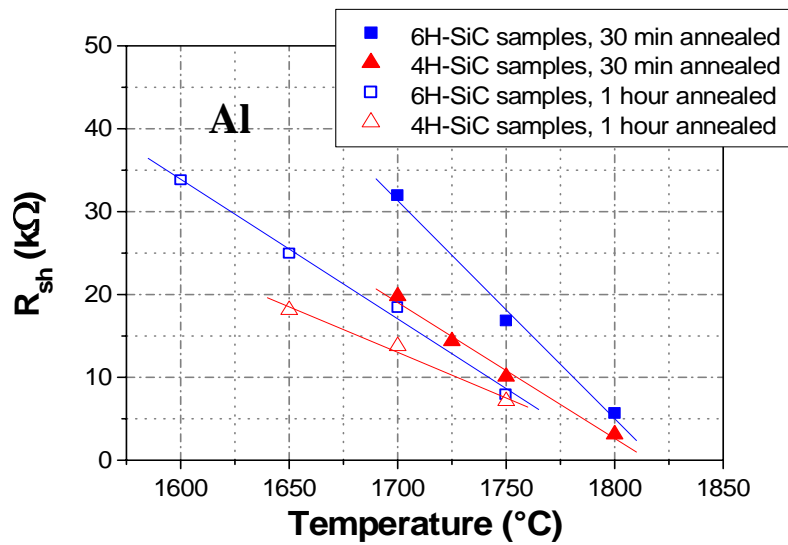
### 2.2.2 Annealing

The post implantation annealing is a necessary step in order to electrically activate the dopants. The annealing is generally performed at temperatures between 1200 °C and 1700 °C. The electrical activation at a certain annealing temperature is characteristic of each species, but the fraction of electrically active atoms increasing for increasing annealing temperature for every species. In fig. 2.9 the values of sheet resistance that can be obtained for phosphorus [Capano2000-2] (a) and aluminium [Lazar] (b) ion implantation as a function of the annealing temperature are reported.

It is evident from fig. 2.9 (a) that the implanted phosphorus atoms are electrically activated even by a low-temperature annealing. The drawback of performing the annealing at high temperature is the formation of furrow-like structures. The depth and width of the grooves increases with increasing annealing temperature and time. This effect is referred to as “step bunching”. It is probably due to the off-axis orientation of SiC crystals: during the annealing evaporation of Si species from the crystal surface occurs, and as they re-deposit, they tend to form macrosteps on the cut-off surface [Chen].



(a)



(b)

**Figure 2.9. Sheet resistance vs annealing temperature for high dose implanted samples. The data are referred to phosphorus (a) and aluminium (b) implantation.**

In order to achieve high donor concentrations phosphorus is a good choice. In fact, it was observed that high concentrations of implanted nitrogen tend to form precipitates, so that the electrical activation undergoes saturation for implanted concentrations higher than  $2 \times 10^{19} \text{cm}^{-3}$ . Such behaviour was not

observed for phosphorus implants, thus phosphorus is preferred in case of high concentration implants [Rao].

Annealing parameters, such as the annealing temperature, duration, and rate of temperature rise and fall, influence the electrical and morphological features of implanted layers. Effects of the heating ramp on surface morphology and electrically active dopants were reported for aluminium implants [Poggi2006], nitrogen implants [Raineri], and nitrogen and phosphorus co-implants [Blanqué]. The reported data suggest that faster heating rates determine increasing electrical activation, but also increasing step bunching. Fig. 2.10 shows data for this trend in case of aluminium implants and annealing at 1600 °C for 30 minutes in argon [Poggi2006].

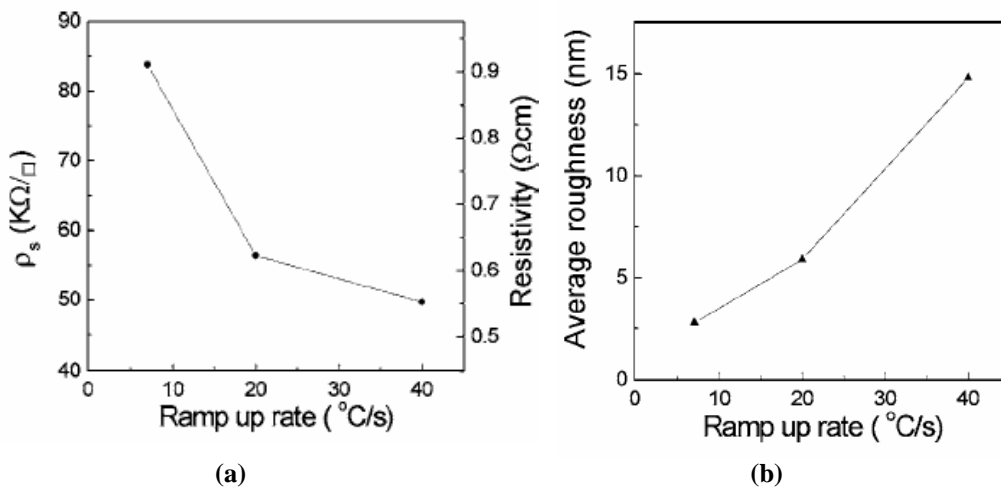


**Figure 2.10. Resistivity (a) and average roughness (b) vs annealing heating rate induced by a 1600 °C annealing in aluminium implanted SiC [Poggi 2006].**

The decrease of the sheet resistance can be due to: 1) an increase in the electrically active dopant concentration; 2) an increase of the free-carrier mobility due to a reduction of the residual implant damage.

A further effect of the heating ramp is the increase of the reverse leakage current of p<sup>+</sup>/n diodes with decreasing ramp rate. These results show that the early stages of the annealing cycle play a relevant role on the defects in the implant tail [Poggi2006].

## Chapter 3

### Fabrication of n<sup>+</sup>/p junctions in SiC

The possibility of fabricating n<sup>+</sup>/p junctions in SiC by lowering the implantation temperature to 300 °C and the annealing temperature to 1300 °C was investigated. The junctions were electrically characterized by current voltage (I–V) and capacitance voltage (C–V) measurements performed on the n<sup>+</sup>/p diodes. The defects introduced in the p-type layer under the implanted regions were investigated by comparing results of deep level transient spectroscopy (DLTS) measurements carried out both on the n<sup>+</sup>/p diodes and on Schottky diodes fabricated on the same wafer. The electrical activation of P atoms was evaluated by sheet resistance measurements on Van der Pauw geometries and TLM structures. An ohmic contact on the n<sup>+</sup> regions, made up of nickel annealed in vacuum at 900°C for 1 minute, was developed. The effect of this thermal treatment on the contact resistance was analysed by TLM measurements, whereas its effect on the series resistance of the diodes was studied by I–V measurements.

#### 3.1 Starting material

A 6H-SiC wafer purchased by CREE research was employed for this study. The substrate was p-type with acceptor concentration  $4.2 \times 10^{18} \text{ cm}^{-3}$ , cut 3.5° off-axis. The epilayer was 10 μm thick, with acceptor concentration equal to  $7.5 \times 10^{15} \text{ cm}^{-3}$ .

#### 3.2 Photolithographic steps

Junction fabrication in SiC needs a three photolithographic steps process. First, SiC etching for the realization of alignment marks. Second, definition of the implantation regions. Third, definition of the contact areas.

The first photolithography process is necessary because the implanted SiC is to be annealed at very high temperatures, higher than the melting point of whatever mask layer, be it silicon dioxide or metal. Thus, it is necessary to remove the implantation mask layer before annealing. In order to align the contact with the implanted regions the material is first etched and the following masks are aligned on the etched marks.

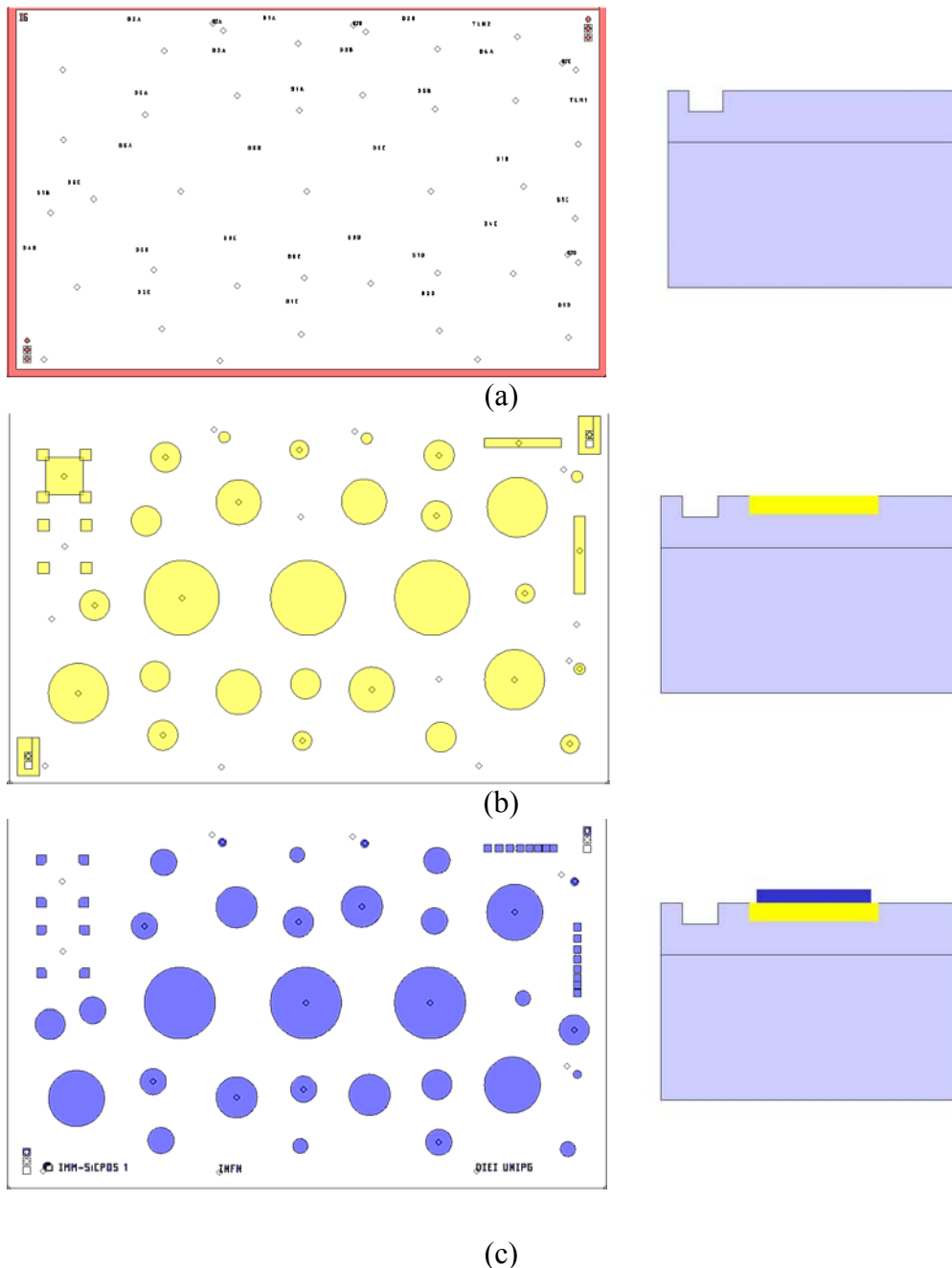


**Figure 3.1. Mask set employed in this study. Alignment mask (a); Implantation mask (b); Metal mask (c). Section views of the samples after the photolithographic steps related to each mask.**

The mask layout employed in this study is illustrated in fig. 3.1. In fig. 3.1 (a) the first mask for the alignment marks is shown, and the etched regions are in red. In fig. 3.1 (b) the implantation regions are shown in yellow. In fig. 3.1 (c) the metal mask is shown and the contact areas are in blue. As it can be noticed in fig. 3.1 (b) and (c), Schottky diodes can be fabricated on the p-type epilayer with the same metal used for the ohmic contacts on the  $n^+$  regions. Test structures, like Van der Pauw and TLM structures have been obtained as well.

### 3.3 Fabrication of n<sup>+</sup>/p diodes

The device fabrication took place in the clean room class 100 of IMM-CNR in Bologna.

First of all the wafer was degreased in boiling acetone and boiling isopropyl alcohol for 5 minutes. Then it was cleaned with a standard Piranha (HCl:H<sub>2</sub>O<sub>2</sub>:H<sub>2</sub>O=1:1:5) for 10 minutes, and with a dip in HF:H<sub>2</sub>O=1:10 for 30 s.

#### 3.3.1 Alignment marks

The alignment marks were obtained by Reactive Ion Etching (RIE) in SiCl<sub>4</sub> plasma. A photoresist film, 1.1 μm thick, was employed as a mask layer. The etching rates for this process were previously calculated to be 50 nm/min for SiC etching and 160 nm/min for photoresist etching. A 5 minute RIE process allowed us to obtain alignment marks 25 nm deep.

The photoresist was then removed by O<sub>2</sub> plasma etching, and Piranha cleaning and HF:H<sub>2</sub>O=1:10 for 30 s were performed.

#### 3.3.2 Ion implantation

The implantation areas were defined in a silicon dioxide mask layer, obtained by low temperature CVD deposition (LTO). The LTO, 600 nm thick, was annealed at 900 °C for 15 minutes in N<sub>2</sub> in order to have the same stoichiometry as a thermal oxide. The implantation areas were defined by using the mask shown in fig. 3.1 (b).

**Table 3.1. Energy and dose values employed in the P<sup>+</sup> ion implantation process.**

Energy (keV)	Dose (cm <sup>-2</sup> )
10	1.5 10 <sup>14</sup>
20	1.5 10 <sup>14</sup>
40	1.5 10 <sup>14</sup>
60	1.0 10 <sup>14</sup>
100	4.2 10 <sup>14</sup>
170	1.05 10 <sup>15</sup>
<b>Total dose</b>	<b>2.03 10<sup>15</sup> cm<sup>-2</sup></b>

The P<sup>+</sup> ion implantation was carried out at 300 °C according to the implantation schedule in Table 3.1. The energy and dose values were calculated by SRIM Monte Carlo simulation in order to obtain a P box profile 200 nm deep with uniform P concentration of 1×10<sup>20</sup> cm<sup>-3</sup>.

In fig. 3.2 the simulated P profile resulting from this implantation schedule is shown. The same profile calculated by constructing the Pearson IV distributions is reported as well.

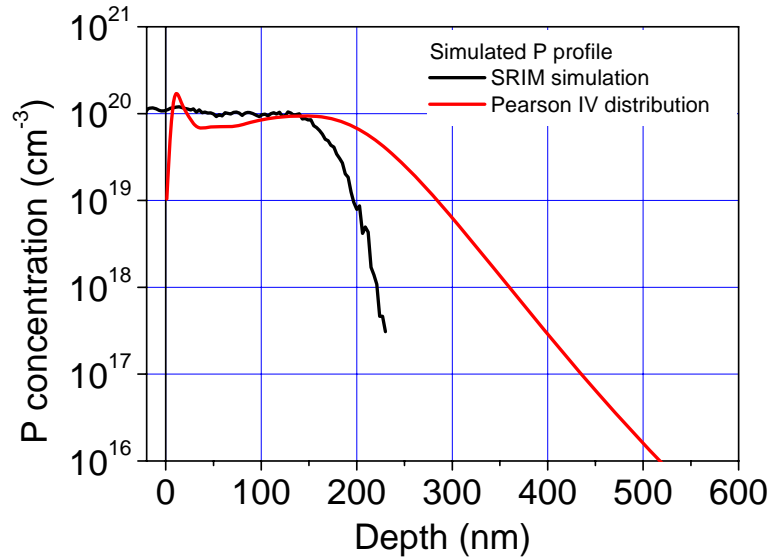


**Figure 3.2. SRIM (back curve) and Pearson IV (red curve) calculations of the P profile resulting from the implantation schedule in table 3.1.**

In order to have a low-resistance ohmic contact on the back of the wafer, the substrate p-type doping was reinforced by Al<sup>+</sup> implantation. Since for this process a high energy ion implanter was employed, a 400 nm thick SiO<sub>2</sub> stopping layer was deposited on the back of the wafer. The Al<sup>+</sup> ion implantation was carried out at 400 °C with energy and dose values illustrated in Table 3.2, in order to obtain an Al box profile 280 nm deep, with plateau concentration  $8 \times 10^{19} \text{ cm}^{-3}$ .

**Table 3.2. Energy e dose values of the Al implantation process on the back surface of the wafer.**

Energy (keV)	Dose (cm <sup>-2</sup> )
250	$7.2 \cdot 10^{14}$
350	$1.5 \cdot 10^{15}$
<b>Total dose</b>	$2.22 \cdot 10^{15} \text{ cm}^{-2}$

### 3.3.3 Annealing

The electrical activation of the dopants was achieved by annealing at 1300 °C for 20 minutes in a J.I.P.ELEC radiofrequency furnace.

The furnace is equipped with a Ar flux line, and with a vacuum turbo pump which allows pressure values around  $10^{-6}$  Torr. Several pumping cycles were performed before annealing to avoid oxygen presence in the chamber, and during the annealing a constant Ar flux equal to 150 sccm was provided, in order to have Ar overpressure and avoid oxygen contamination to occur.

The rate of temperature rise was around 40 °C/s, in order to have better P electrical activation, as explained in Chapter 2.

The rate of temperature fall depends on the thermal inertia of the furnace. A graphite susceptor was employed. The temperature in the centre of the susceptor was monitored by a pyrometer. Since RF furnaces are featured by high lateral thermal gradients [Ottaviani], a thick SiC disk was put on the cover of the susceptor, in order to have a better temperature uniformity between the centre and the borders. The wafer was cut into quarters before annealing to have more process variables. The quarters were annealed separately, and held in the centre of the susceptor by two pieces of polycrystalline SiC.

Since a good electrical activation of Al can be achieved by annealing at temperatures around 1600-1700 °C, we expect a partial Al activation. On the other hand, the back surface is completely covered with metal, thus a low contact resistance can be obtained even if the Al activation is low.

### 3.3.4 *Contacts*

The back contact was made up of a 80 nm thick Ti layer and a 350 nm thick Al layer, annealed at 1000°C in vacuum for 2 minutes in the J.I.P.ELEC furnace. The back surface of the samples was entirely covered with metal. The pressure during this treatment was between  $6 \times 10^{-6}$  Torr and  $2 \times 10^{-5}$  Torr.

The ohmic contacts on the n-type regions was made up of Ni. The Ni definition was achieved according to the mask in fig. 3.1 (c), employing the lift-off technique. The lift-off technique can be explained as follows:

- 1) The sample is covered with photoresist, and the contact geometries are etched in the photoresist
- 2) The metal is deposited on the photoresist and on the SiC surface, where the photoresist was etched.
- 3) The photoresist is removed. As a consequence the metal deposited on the photoresist layer is removed as well, whereas the metal on the SiC surface persists.

The lift-off technique was advantageous in this study because of the presence of a metal on the back surface of the samples. Since the front contact definition is achieved by photoresist etching (with a solvent), not metal etching (with and acid), the back metal is not damaged by this treatment.

The contact regions were defined in the photoresist, and a Ni layer 50 nm thick was deposited by electron beam.

After this step a first electrical characterisation of the junctions was performed by I-V and C-V measurements. The P electrical activation was evaluated by sheet resistance measurements. DLTS measurements were performed in order to study the electrically active hole traps in the epilayer under the implanted regions.

After the first characterisation the Ni was removed and re-deposited. A thermal treatment in the J.I.P.ELEC furnace at 900 °C for 1 minute in vacuum was performed in order to form NiSi<sub>2</sub>.

After this alloy treatment the diodes were electrically characterised again (by I-V, C-V and TLM measurements), and DLTS measurements and EBIC analyses were performed.

## Chapter 4

### Electrical characterizations: theory

#### 4.1 Characterization of electrical properties of doped layers

##### 4.1.1 Sheet resistance

Sheet resistance measurements are carried out in order to determine the concentration of carriers available for conduction in implanted layers.

The sheet resistance, i.e. the quantity that characterizes thin implanted layers, is defined as:

$$R_{sh} = \frac{\rho}{t} \quad (4.1)$$

Where  $\rho$  is the resistivity and  $t$  the thickness of the doped layer. It represents the resistance of a square of side  $l$  and thickness  $t$  of semiconductor (fig. 4.1): if a bias is applied to two sides, current flows in the layer, whose section is equal to  $t \times l$  and whose length is  $l$ .

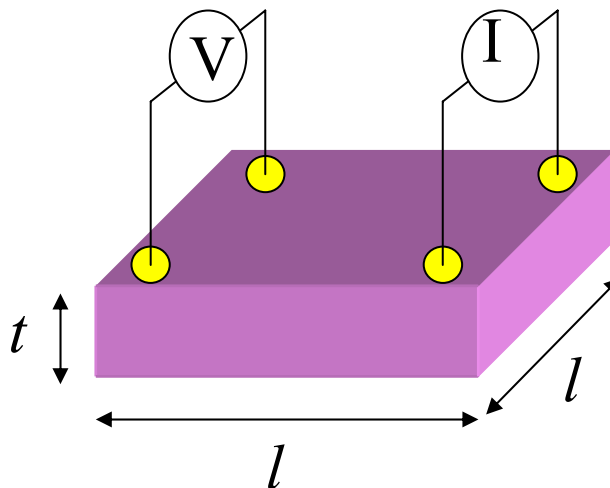


Figure 4.1. Schematic representation of a square of side  $l$  and thickness  $t$  subject to an applied bias.

The resistivity is the proportionality factor between the current density and the applied electric field in the layer

$$E = \rho J. \quad (4.2)$$

The resistivity is related to the microscopic properties of the material through:

$$\rho = 1/qn\mu; \quad (4.3a)$$

if conduction is due to both carriers

$$\rho = 1/q(n_e\mu_e + n_p\mu_p) \quad (4.3b)$$

where  $e$  stands for electrons and  $p$  for holes.

From sheet resistance measurements information on the conduction properties of the material can be drawn. The contributions of the mobility and of the concentration of carriers can not be isolated. The carrier mobility is thus generally determined by Hall effect measurements [Soncini].

Due to the incomplete ionization of dopants in SiC, the effective value of the electrically active dopants must be determined by high temperature Hall effect measurement, or Scanning Capacitance Microscopy (SCM) measurements.

#### 4.1.2 Sheet resistance measurements on Van der Pauw geometries

Sheet resistance measurements on Van der Pauw geometries are based on the Van der Pauw theorem [Van der Pauw]: given a flat sample of arbitrary shape and four contacts of arbitrary position along the circumference we define:

$$R_{ABCD} = \frac{V_D - V_C}{I_{AB}} \quad (4.4)$$

Where  $V_D - V_C$  is the potential difference between the adjacent contacts D and C and  $I_{AB}$  is the current between the adjacent contacts A and B. The quantity  $R_{BCDA}$  is defined similarly. It can be demonstrated that

$$\rho = \frac{\pi}{\ln 2} \frac{R_{ABCD} + R_{BCDA}}{2} f\left(\frac{R_{ABCD}}{R_{BCDA}}\right) \quad (4.5)$$

Where  $t$  is the thickness of the layer and  $f$  is a function of the ratio  $R_{ABCD}/R_{BCDA}$  and satisfies the relation

$$\frac{R_{ABCD} - R_{BCDA}}{R_{ABCD} + R_{BCDA}} = f \operatorname{arccosh}\left\{\frac{\exp(\ln 2 / f)}{2}\right\} \quad (4.6)$$

When  $R_{BCDA}$  and  $R_{ABCD}$  are almost equal,  $f=1$ .

### 4.1.3 Scanning Capacitance Microscopy measurements

SCM measurements provide information on electrically active dopants in implanted layers. In this technique the tip of an Atomic Force Microscope is biased with a dc signal and an ac signal is superimposed in order to measure a differential capacitance [Blood, w-ois, w-ntmdt].

The bias applied to the tip can be written as:

$$V_{tip} = V_{dc} + V_{ac} \sin(\omega t). \quad (4.7)$$

The principle of operation is based on the MOS capacitor physics between the nanometer-sized probe and the underlying semiconductor. A thin oxide is present on the semiconductor surface. The dopant concentration under the probe is related to the change in capacitance,  $dC$ , when bias applied to the probe changes the semiconductor surface from accumulation to inversion.  $dC$  is the difference between the accumulation and inversion (or deep-depletion) capacitance. Since a lower dopant concentration results in a lower inversion capacitance, thus a lower dopant concentration will give rise to a larger SCM or  $dC$  signal and viceversa [Kopanski].

By scanning the sample surface the map of electrically active dopants is obtained. By scanning the sample cross section the dopant profile is obtained. By comparing SIMS profiles and SCM profiles the fraction of electrically active dopants (*i.e.* the fraction of the implanted dopants promoted into substitutional position by the annealing) can be evaluated.

## 4.2 Electrical characterizations of a p-n junction

### 4.2.1 Properties of p-n junctions

A p-n junction is made up of two regions of semiconductor, one n-type, with donor density  $N_d$ , and one p-type, with acceptor density  $N_a$ . When they are put in contact a flow of electrons from the n region to the p region takes place, in order to contrast the concentration gradient in the two regions. In proximity of the junctions recombination processes take place and the ionised doping species remain fixed. Equilibrium is reached when the electric field determined by the fixed charge induces a flow of carriers equal and opposite to the one induced by the concentration gradient (fig. 4.2).

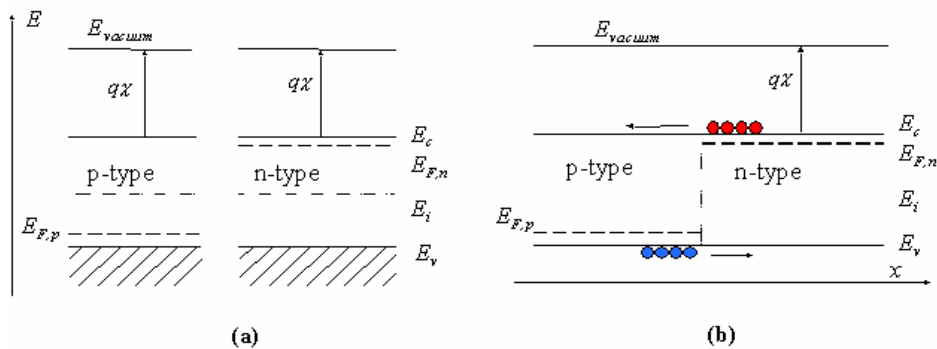


Figure 4.2. Band diagram of a p-n junction, before (a) and after (b) the contact between the two regions.

The internal potential difference determined by the fixed charge is defined built-in potential,  $\phi_i$ . It is equal to the difference between the Fermi energy in the n-type region and the Fermi energy in the p-type region.

When a negative bias is applied to the p-type region (reverse bias) majority carriers are swept away from the junction, and the band bending increases. This inhibits the current flow (fig. 4.3a). When a positive bias is applied to the p-type region (forward bias) majority carriers are injected into the junction and the band bending decreases. Thus, current flows through the junction (fig. 4.3b). Thus, a p-n junction is rectifying.

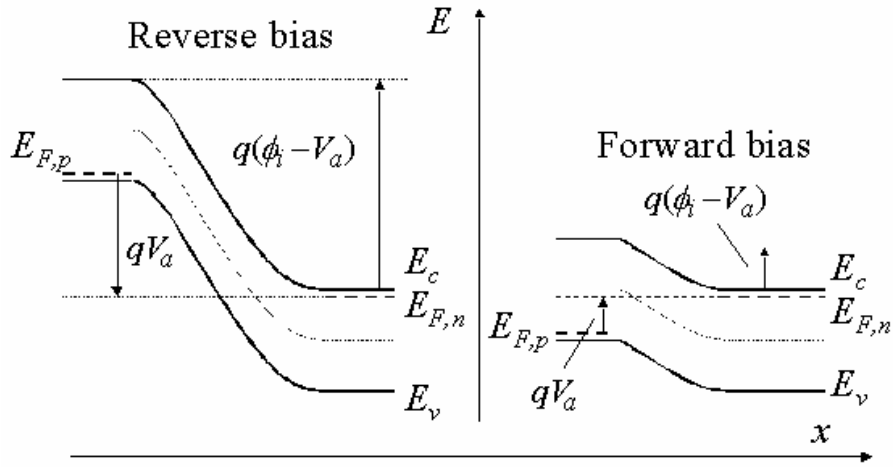


Figure 4.3. Band diagram of a p-n junction in reverse (a) and forward (b) bias.

#### 4.2.2 Current-voltage measurements

In this section the mechanisms that rule the current transport in a diodes are described. Current can be due to diffusion of carriers from a region to the other (Shockley equation) and to recombination and generation of carriers in the space charge region due to the presence of electrically active defects.

##### Diffusion current

The electron current is related to the carrier concentration and to the band bending.

$$J_n = q\mu_e \left( nE + \frac{kT}{q} \nabla n \right) = q\mu_e n (-\nabla \psi) + q\mu_e \frac{kT}{q} \left[ \frac{qn}{kT} (\nabla \psi - \nabla \phi_n) \right] = q\mu_e n \nabla \phi_n. \quad (4.8)$$

Similarly for hole current

$$J_p = q\mu_p n \nabla \phi_p. \quad (4.9)$$

In thermal equilibrium  $\phi_n = \phi_p = \phi$ , thus the diffusion current is zero. If a bias is applied  $\phi_n$  and  $\phi_p$  are no longer constant all over the junction. The internal potential difference is given by

$$V = \phi_p - \phi_n \quad (4.10)$$

The electron density at the boundary of the depletion layer on the p-side is thus given by

$$n_p = \frac{n_i^2}{p_p} \exp\left(\frac{qV}{kT}\right) = n_{p0} \exp\left(\frac{qV}{kT}\right) \quad (4.11)$$

Where  $n_{p0}$  is the free electron concentration in the neutral p-type region. Similarly

$$p_n = p_{n0} \exp\left(\frac{qV}{kT}\right). \quad (4.12)$$

From the continuity equation for the steady state we obtain

$$-U + \mu_e E \frac{\partial n_n}{\partial x} + \mu_e n_n \frac{\partial E}{\partial x} + D_n \frac{\partial^2 n_n}{\partial x^2} = 0 \quad (4.13)$$

$$-U - \mu_p E \frac{\partial p_n}{\partial x} - \mu_p p_n \frac{\partial E}{\partial x} + D_p \frac{\partial^2 p_n}{\partial x^2} = 0 \quad (4.14)$$

$$-\frac{p_n - p_{n0}}{\tau_a} + Da \frac{\partial^2 p_n}{\partial x^2} - \frac{n_n - p_n}{n_n / \mu_p + p_n / \mu_e} E \frac{\partial p_n}{\partial x} = 0 \quad (4.15)$$

where

$$D_a = \frac{n_n + p_n}{n_n / D_p + p_n / D_n} \quad (4.16)$$

and

$$\tau_a = \frac{p_n - p_{n0}}{U} = \frac{n_n - n_{n0}}{U} \quad (4.17)$$

are the ambipolar diffusion coefficient and lifetime.

In the low-injection conditions  $n_n \gg p_n$

$$-\frac{p_n - p_{n0}}{\tau_p} + D_p \frac{\partial^2 p_n}{\partial x^2} - \mu_p E \frac{\partial p_n}{\partial x} = 0. \quad (4.18)$$

In the neutral region the electric field is zero, thus

$$-\frac{p_n - p_{n0}}{\tau_p} + D_p \frac{\partial^2 p_n}{\partial x^2} = 0. \quad (4.19)$$

The solution of this equation with the boundary conditions yields

$$p_n - p_{n0} = p_{n0} \left( \exp\left(\frac{qV}{kT}\right) - 1 \right) \exp\left(-\frac{x - x_n}{L_p}\right) \quad (4.20)$$

with

$$L_p = \sqrt{D_p \tau_p}. \quad (4.21)$$

At  $x=x_n$

$$J_p = \frac{qD_p p_{n0}}{L_p} \exp\left(\frac{qV}{kT} - 1\right) \quad (4.22a)$$

$$J_e = \frac{qD_e n_{p0}}{L_e} \exp\left(\frac{qV}{kT} - 1\right) \quad (4.22b)$$

Thus

$$J = J_s \left[ \exp\left(\frac{qV}{kT}\right) - 1 \right], \quad (4.23)$$

with

$$J_s = \frac{qD_p p_{n0}}{L_p} + \frac{qD_e n_{p0}}{L_e} \quad (4.24)$$

This is the Shockley equation. It holds in the ideal case, when no traps are active in the band gap. In case of trap the generation-recombination of carriers at the traps must be considered [Sze].

*Generation-recombination current*

The generation-recombination current is due to traps in the band gap [Grove]. Its contribution is more important the higher is the band gap of the material, since it depends on the intrinsic carrier concentration, whereas the diffusion current is proportional to the square of the intrinsic carrier concentration.

The general expression for current in a p-n junction is

$$J_{gen-rec} = qWU \quad (4.25)$$

Where U is the generation rate in the semiconductor [Grove]:

$$U = \frac{\sigma_n \sigma_p v N_T (pn - n_i^2)}{\sigma_n [n + n_i \exp(\frac{E_T - E_i}{kT})] + \sigma_p [p + n_i \exp(\frac{E_i - E_T}{kT})]} \quad (4.26)$$

Different approximations are made, according to the bias conditions.

*Forward bias*

When the junction is forward biased majority carriers are injected: thus,  $np > n_i^2$  in the whole semiconductor. Though forward bias tends to have band bending reduced, the presence of a space charge region produces an electric field, which inhibits carrier cross the junction. Thus, current flow is ruled by the recombination of the injected carriers .

The following hypotheses are made:

$$\sigma_n = \sigma_p = \sigma$$

$$np > n_i^2.$$

Thus,

$$U = \frac{\sigma v N_T np}{n + n_i \exp(\frac{E_T - E_i}{kT}) + p + n_i \exp(\frac{E_i - E_T}{kT})}. \quad (4.27)$$

Since

$$n = n_i \exp\left(\frac{E_{Fn} - E_i}{kT}\right) \quad (4.28a)$$

$$p = n_i \exp\left(\frac{E_i - E_{Fp}}{kT}\right) \quad (4.28b)$$

and

$$V = \frac{E_{Fn} - E_{Fp}}{q} \quad (4.29)$$

thus

$$U = \frac{\sigma v N_T n_i^2 \exp(qV / kT)}{n_i \exp\left(\frac{E_{Fn} - E_i}{kT}\right) + n_i \exp\left(\frac{E_i - E_{Fp}}{kT}\right) + 2n_i \cosh\left(\frac{E_i - E_T}{kT}\right)}. \quad (4.30)$$

In the space charge region  $E_i$  is halfway between  $E_{Fn}$  and  $E_{Fp}$ ,

$$E_i = \frac{E_{Fp} + E_{Fn}}{2}. \quad (4.31)$$

The recombination rate is maximum when the recombination centre is near the intrinsic level, i.e. when the recombination centre is near midgap. The recombination rate becomes therefore

$$U = \frac{\sigma v N_T n_i \exp(qV / kT)}{2 \left[ \exp\left(\frac{qV}{2kT}\right) + 1 \right]} \quad (4.32)$$

$$U = \frac{1}{2} \sigma v N_T n_i \exp(qV / 2kT). \quad (4.33)$$

Since the recombination current is given by:

$$J = qWU. \quad (4.34)$$

Then

$$J_{rec} = \frac{1}{2} qW \sigma v N_T n_i \exp(qV / 2kT) \quad (4.35)$$

The recombination current depends on the trap concentration and cross section.

#### *Reverse bias*

In the case of a reverse biased junction the main process is generation of carriers in the space charge region, because of the reduction in carrier concentration ( $np \ll n_i^2$ ). Eq. 4.26 becomes:

$$U = -\frac{\sigma v N_T n_i}{\exp\left(\frac{E_T - E_i}{kT}\right) + \exp\left(\frac{E_i - E_T}{kT}\right)} \quad (4.36)$$

with the hypothesis  $\sigma_n = \sigma_p = \sigma$

Also in case of reverse bias  $U$  is maximum for a trap near midgap.  
If we define

$$\tau = \frac{\exp\left(\frac{E_T - E_i}{kT}\right) + \exp\left(\frac{E_i - E_T}{kT}\right)}{\sigma v N_T} \quad (4.37)$$

then

$$U = -\frac{n_i}{\tau} \quad (4.38)$$

The reverse generation current is thus given by

$$J_{gen} = qW \frac{n_i}{\tau} \quad (4.39)$$

The reverse current increases with increasing reverse bias due to the dependence

$$W = (V_{bi} + V)^{1/2} \quad (4.40)$$

Thus, taking into account the two contributions, the *total current* in a diode is thus given by

$$J_f = J_{diff} + J_{rec} = J_s \left[ \exp\left(\frac{qV}{kT}\right) - 1 \right] + \frac{1}{2} qW \sigma v N_T n_i \exp\left(\frac{qV}{2kT}\right) \quad (4.41a)$$

in forward bias, and

$$J_r = J_{diff} + J_{rec} = J_s \left[ \exp\left(\frac{qV}{kT}\right) - 1 \right] + qW \frac{n_i}{\tau} \quad (4.41b)$$

in reverse bias.

Fig. 4.4 represents the I-V curve of a diode with respect to the ideal behaviour. In forward bias recombination current is the dominant contribution at low voltages. As the applied bias increases the diffusion current becomes comparable and higher. For this reason the current of a real diode is often expressed by

$$J = J_s \left[ \exp\left(\frac{q(V_a - IR_s)}{nkT}\right) - 1 \right]. \quad (4.42)$$

$n$  is the ideality factor of the diode, and  $R_s$  is the series resistance, which takes into account the contact resistance and the epilayer resistance. The series resistance produces a difference between the applied bias and the effective bias across the junction, but its effect can be neglected at low currents [Sze]. From the I-V curve of a p-n diode the values of  $J_s$ ,  $n$  ed  $R_s$  can be calculated.  $J_s$  is obtained by the extrapolation of the current at zero bias:

$$J_s = \lim_{v \rightarrow 0} J \quad (4.43)$$

$n$  is given by

$$n = \frac{q}{kT} \frac{\partial V}{\partial \ln J} \quad (4.44)$$

in the exponential region.

And  $R_s$ :

$$R_s = \lim_{V \rightarrow \infty} \frac{\partial V}{\partial I} \quad (4.45)$$

in the high current region.

In reverse bias, in the presence of generating defects, the current increases with increasing bias because of the effect of the dependence of the depletion layer width on the applied bias.

For high values of applied reverse bias, an avalanche multiplication mechanism is generated, and a high current crosses the junction. The threshold value is defined breakdown voltage,  $V_{bd}$ . When the applied bias is higher than  $V_{bd}$  the carriers accelerated by the high electric field, have enough energy to ionise the atoms of the lattice. Electron-hole pairs are created and the avalanche mechanism is generated.

If the threshold value for the electric field to have avalanche multiplication of carriers is  $E_{crit}$ , then the breakdown voltage is related to the epilayer doping and thickness through the relation [Grove]:

$$V_{bd} = E_{crit} W_{epy} - \frac{qN_a W_{epy}^2}{2\epsilon_s}. \quad (4.46)$$

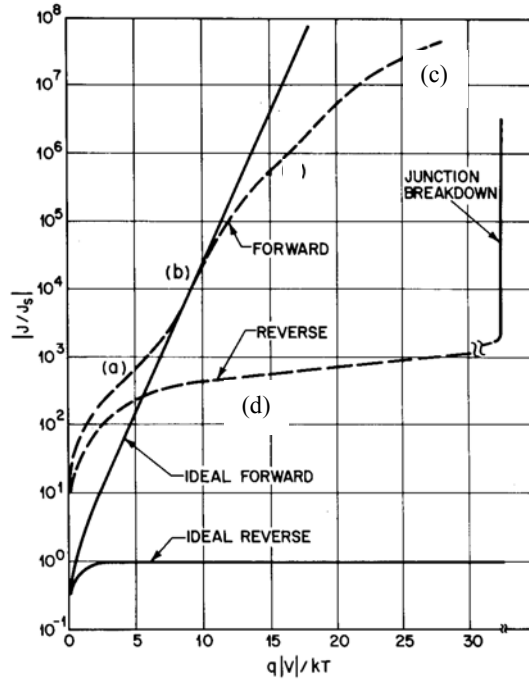


Figure 4.4. I-V curve of a p-n junction. The mechanisms of current transport can be observed. In forward bias: recombination of carriers in the space charge region (a), diffusion current (b), series resistance contribution (c). In reverse bias the current is higher than its ideal value predicted by the Shockley equation because of the generation of carriers in the space charge region (d) [Sze].

### 4.2.3 Capacitance voltage measurements

The space charge region of a p-n junction can be considered a parallel plate capacitor. They differ mainly in the dependence of the stored charge on the applied bias. In a p-n junction the charge depends on the applied bias, thus we can define a differential capacitance per unit area:

$$C(V_a) = \left| \frac{\partial Q(V_a)}{\partial V_a} \right|. \quad (4.47)$$

The relationship between the charge  $Q$  and the applied bias can be found by solving the Poisson equation for the junction:

$$\frac{\partial^2 \phi}{\partial x^2} = -\frac{\rho}{\epsilon_s} \quad (4.48)$$

where  $\rho$  is the charge density and  $\epsilon_s$  is the dielectric permittivity of the semiconductor.

The depletion approximation, *i.e.* the transition region between the space charge region and the neutral region can be neglected, is assumed to be valid.

From (4.48) two equations are obtained, one for the n-type region and one for the p-type region:

$$\frac{\partial^2 \phi}{\partial x^2} = qN_d \quad (4.49a)$$

$$\frac{\partial^2 \phi}{\partial x^2} = -qN_a \quad (4.49b)$$

By solving these equations the extension of the depletion region is found as a function of the applied bias, both in the n-type region and in the p-type region (eqs. 4.50a and 4.50b).

$$x_n = \left( \frac{2\epsilon_s}{q} \frac{N_a}{N_d} \frac{1}{N_a + N_d} (\phi_i - V_a) \right)^{1/2} \quad (4.50a)$$

$$x_p = \left( \frac{2\epsilon_s}{q} \frac{N_d}{N_a} \frac{1}{N_a + N_d} (\phi_i - V_a) \right)^{1/2} \quad (4.50b)$$

Since

$$Q_n = qN_d x_n \quad (4.51a)$$

and

$$Q_p = qN_a x_p \quad (4.51b)$$

the capacitance of the space charge region is given by

$$C = \left( \frac{q\epsilon_s}{2(\phi_i - V_a)} \frac{N_a N_d}{N_a + N_d} \right)^{1/2} \quad (4.52)$$

By comparing eqs. (4.52) and (4.50) the dependence of the capacitance per unit area of a p-n junction is the same as for a parallel plate capacitor, but in a p-n junction the charge, and, consequently, the capacitance, depend on the applied bias.

In eq. (4.52) the quantity  $1/C^2$  shows a linear dependence on the applied bias  $V_a$ :

$$\frac{1}{C^2} = a + bV_a \quad (4.53)$$

Where the intercept with the  $y$  axis gives the built-in potential

$$\phi_i = \frac{aq\epsilon_s}{2} \frac{N_a N_d}{N_a + N_d} ; \quad (4.54)$$

The slope is related to the doping concentration:

$$b = -\frac{2}{q\epsilon_s} \frac{N_a N_d}{N_a + N_d} . \quad (4.55)$$

In a  $n^+/p$  junction,  $N_d \gg N_a$ ; the value of the doping density in the lightly doped region, in this case the p-type region, can thus be obtained:

$$N_a = -\frac{2}{q\epsilon_s b} . \quad (4.56)$$

By solving the Poisson equation for different values of the applied bias the doping profile in the lightly doped region can be obtained [Sze].

### 4.3 Capacitance-voltage measurements on Schottky diodes

The depleted region of a Schottky diode can be considered as a parallel plate capacitor. The difference between a p-n junction and a Schottky barrier lies in the fact that in a Schottky barrier the depletion region is located only in the semiconductor. Since the quantity of stored charge depends on the depletion layer width, a differential capacitance can be defined:

$$C(V_a) = \left| \frac{\partial Q(V_a)}{\partial V_a} \right| . \quad (4.57)$$

The relationship between the stored charge and the applied bias can be found by solving the Poisson equation in the full depletion approximation:

$$\frac{\partial^2 \phi}{\partial x^2} = -\frac{\rho}{\epsilon_s} . \quad (4.58)$$

For a Schottky barrier on a p-type material, the capacitance per unit area is:

$$C = \left( \frac{q\epsilon_s}{2(\phi_i - V_a)} N_a \right)^{1/2} . \quad (4.59)$$

Since  $1/C^2$  is linearly dependent on the a applied bias:

$$\frac{1}{C^2} = a + bV_a \quad (4.60)$$

the barrier height is related to the intercept with the y axis,  $a$ , through the relations:

$$\phi_i = \frac{1}{2} q \epsilon_s N_a a \quad (4.61)$$

and

$$\phi_b = \phi_i + \frac{kT}{q} \ln \frac{N_v}{N_a} \quad (4.62)$$

whereas the slope is related to the acceptor doping [Sze]:

$$N_a = \frac{2}{q \epsilon_s b}. \quad (4.63)$$

#### 4.4 Characterization of electrically active defects in semiconductors: DLTS

Impurities and defects introduce energy levels in the band gap of a semiconductor. These are usually divided into two classes, shallow and deep states. Shallow levels are hydrogenic impurities at which the electron is weakly bound by a Coulomb potential in an extended state, with the effective mass of the appropriate band edge. In the case of deep level the impurity potential is strongly localized, and the electrons are tightly bound. The terms shallow and deep are referred to the energy level of the defect in the band gap, since the energy level of deep centres is deeper in the band gap than the energy level of shallow impurities [Blood].

The study of deep centres needs techniques sensitive to low defect concentrations, able to distinguish between majority- and minority-carrier traps, to provide information about the concentrations, energy levels and capture rates of the traps [Lang 1974]. These techniques are mostly based on the study of transient phenomena related to carrier capture and emission at the centres. In a p-n junction or in a Schottky diode a pulsed bias induces a transient of the junction capacitance. By monitoring the transient response as a function of temperature information on defect energy level, concentration, and capture rate are caught.

##### 4.4.1 Physics of carrier capture and emission at a trap

The dynamic occupancy at a deep centre is determined by capture of majority and minority carriers, and emission of majority and minority carriers. Capture

processes are characterized by the capture cross section  $\sigma_{n,p}$ , related to the carrier concentration  $n$  and to the carrier thermal velocity  $\langle v_{n,p} \rangle$ . If the total trap concentration is  $N_T$  and if  $n_T$  are the traps occupied by electrons at any instant, the number of electrons captured by the unoccupied traps in the time interval  $\Delta t$  is:

$$\Delta n_T = \sigma_n \langle v_n \rangle n (N_T - n_T) \Delta t \quad (4.64)$$

and the electron capture rate is

$$c_n = \sigma_n \langle v_n \rangle n \quad (4.65a)$$

whereas the hole capture rate is

$$c_p = \sigma_p \langle v_p \rangle p. \quad (4.65b)$$

Carrier emission is characterized by the emission rate  $e_{n,p}$ . Thermal emission rates are proportional to the Boltzmann factor,  $\exp(-\Delta E/kT)$ , where  $\Delta E$  is the difference in energy between the trap and the conduction/valence band.

$$e_n = \frac{\sigma_n \langle v_n \rangle N_C}{g} \exp\left(-\frac{\Delta E}{kT}\right) \quad (4.66a)$$

$$e_p = \frac{\sigma_p \langle v_p \rangle N_V}{g} \exp\left(-\frac{\Delta E}{kT}\right). \quad (4.66b)$$

The occupancy of the state is determined by the competing emission and capture processes. The net change of electron occupancy at a trap is given by

$$\frac{dn_T}{dt} = (c_n + e_p)(N_T - n_T) - (e_n + c_p)n_T \quad (4.67)$$

Where  $n_T$  is the number of occupied states and  $N_T$  is the total concentration of traps.

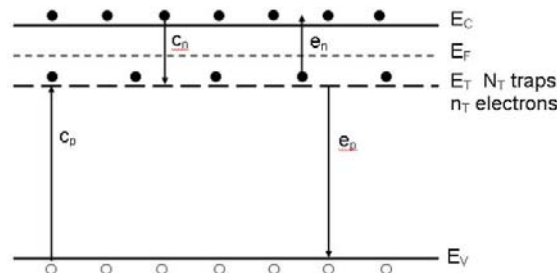


Figure 4.5. Capture and emission processes at a trap

Fig. 4.5 illustrates the capture and emission processes that take place at a deep level with energy  $E_T$ , and density  $N_T$ , occupied by  $n_T$  electrons.

Let us consider a  $n^+/p$  diode, that is the case analysed in this thesis. The junction behaviour is completely general, thus a Schottky diode will behave in the same way. Since the depletion region is primarily in the lightly doped side of the junction, the discussion is focused only on the traps in the lightly doped p-type material of a  $n^+/p$  diode. When the diode is reverse biased, the capture rates are zero because no mobile carriers are available for capture. The steady-state occupation of the level is given by

$$n_T = \left[ \frac{e_p}{e_n + e_p} \right] N_T. \quad (4.69)$$

Traps can be divided into electron traps or hole traps. Electron traps tend to be empty and thus capable of capturing electrons, whereas hole traps tend to be occupied by an electron in order to have a hole recombine with the trapped electron (capture a hole). Consequently for electron traps  $e_n \gg e_p$  and for hole traps  $e_p \gg e_n$ .

The equilibrium state can be reached from two initial conditions, i.e. all the traps are initially occupied or all the traps are initially empty. For the first case:

$$n(t) = N_T \quad t < 0 \quad (4.70a)$$

$$n(t) = N_T (1 - \exp(-c_n t)) \quad t > 0. \quad (4.70b)$$

For the second case

$$n(t) = 0 \quad t < 0 \quad (4.70c)$$

$$n(t) = N_T \exp(-e_n t) \quad t > 0. \quad (4.70d)$$

When a bias pulse is applied to the junction carriers are introduced, and the steady state occupancy is perturbed. The bias pulse also produces a capacitance change in the junction. Two main types of bias pulses can be distinguished: majority-carrier pulses, which momentarily reduce the capacitance and introduce only majority carriers; minority-carriers pulses, that drive momentarily the junction into forward bias, and minority and determine majority carrier injection. When the bias pulse is removed the capacitance returns to its quiescent value (figure 4.6). The sign of capacitance change depends on whether the occupation of the traps had been increased or decreased by the pulse. For majority carrier injection the capacitance is reduced after the bias pulse, because compensating carriers are trapped in the space charge region, thus, the transient induced by majority carrier traps is

negative. An increase in occupation by minority carriers causes an increase in capacitance, thus a transient induces by minority-carrier traps unloading is positive. Figure 4.6 is a schematic diagram of the trap occupation in a n<sup>+</sup>/p diode in the quiescent state (a,d), during the pulse (b,e), and after the bias pulse (c,f), for majority and minority carrier traps.

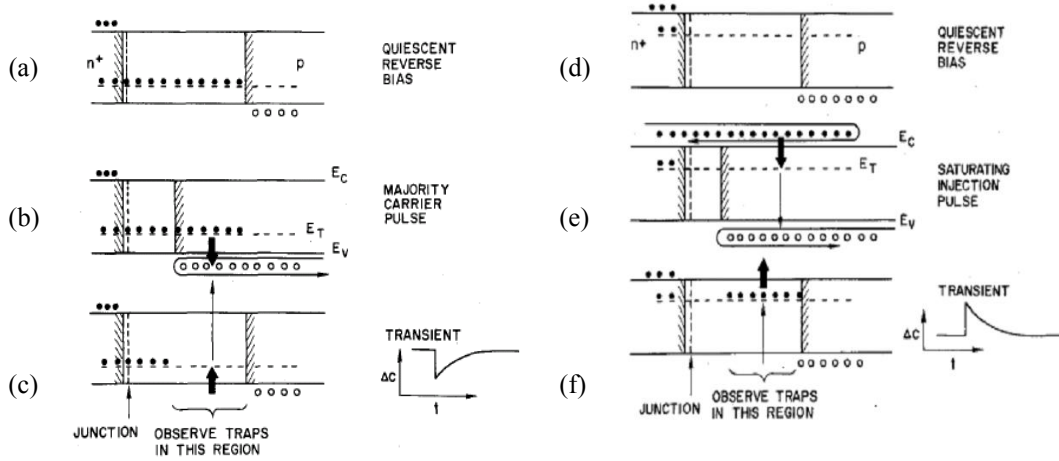


**Figure 4.6. Electron (a,b,c) and hole traps (d,e,f) in a n<sup>+</sup>/p junction in the quiescent state (a,d), during a minority carrier injection pulse (b) or a majority carrier injection pulse (e), and after the injection pulse, during the transient (c,f).**

The transient response provides information on trap-loading procedures. The concentration of the traps is obtained from the transient amplitude. The concentration of hole traps in a n<sup>+</sup>/p diode is given by the relationship

$$N_T = 2 \frac{\Delta C}{C} (N_A - N_D) \quad (4.71)$$

Where  $\Delta C$  is the capacitance change at the instant zero  $C$  is the capacitance in the quiescent state, and  $N_A - N_D$  is the apparent acceptor concentration on the p-side of the junction where the trap is observed.

#### 4.4.2 Majority carrier traps spectroscopy by DLTS

The DLTS technique is based on measurements of capacitance transients as a function of temperature. An apparatus capable of measuring the capacitance signal at two instants during the transient is employed.

The diode is reverse biased at a voltage  $V_r$  and is then filled for a time  $t_f$ . A majority carrier transient is produced by filling the traps maximum to zero bias, whereas a minority carrier transient can be produced by filling the traps with a slightly positive bias, in case of a p-n junction, or with a light pulse in case of a Schottky diode.

The bias is periodic with a period  $t_r$ , as shown in fig. 4.7a. During the pulse, majority carriers are injected into the depletion layer and traps are filled. When the bias is set to  $V_r$  again, carriers are emitted at a rate  $e_p$  producing an exponential transient (figure 4.7b).

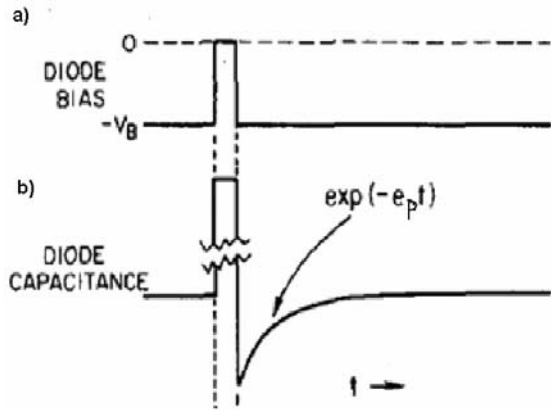


**Figure 4.7. Periodic bias pulse applied to the junction (a), and consequent exponential transient (b).**

The capacitance transient in its general form can be written as

$$C(t) = C(\infty) + \Delta C_0 \exp(-t/\tau). \quad (4.72)$$

Thus the signal is given by

$$S = \Delta C_0 [\exp(-t_1/\tau) - \exp(-t_2/\tau)] \quad (4.73)$$

where  $t_1$  and  $t_2$  are the instants at which the capacitance is measured, and  $\tau$  is the time constant equal to  $e_p^{-1}$ . The maximum signal is obtained when the time constant  $\tau$  is equal to a preset time constant  $\tau_{ref}$ .

$$\tau(T) = \tau_{ref} = (t_2 - t_1) [\ln(t_2/t_1)]^{-1}. \quad (4.74)$$

The dependence of  $e_p$  on the junction temperature (see eq. 4.66b), is illustrated in fig. 4.8.

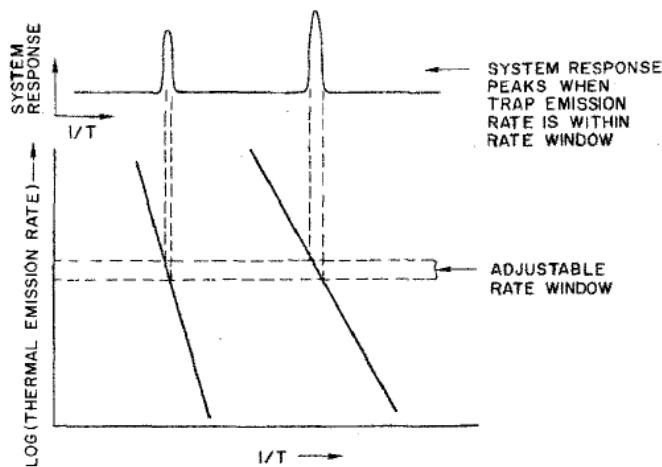


**Fig. 4.8. Relationship between the temperature dependent emission rate of a trap and peak temperature.**

Consider two traps, featured by  $E_1$  and  $\sigma_1$  and  $E_2$  and  $\sigma_2$  respectively. As temperature increases the emission rate  $e_p$  increases and a peak occurs when  $\tau=e_p^{-1}$  passes through  $\tau_{ref}$  for each trap. The DLTS output as a function of temperature is illustrated in figure 4.9. For a given  $\tau_{ref}$  the peak temperatures  $T_{pk1}$  and  $T_{pk2}$  are characteristic of each trap. By varying the  $t_1$  and  $t_2$  the peak position of each trap shifts (as can be seen in fig. 4.8) and  $e_p$  can be obtained as a function of temperature. The height of the peak maximum is related to the trap concentration (eq. 4.71).

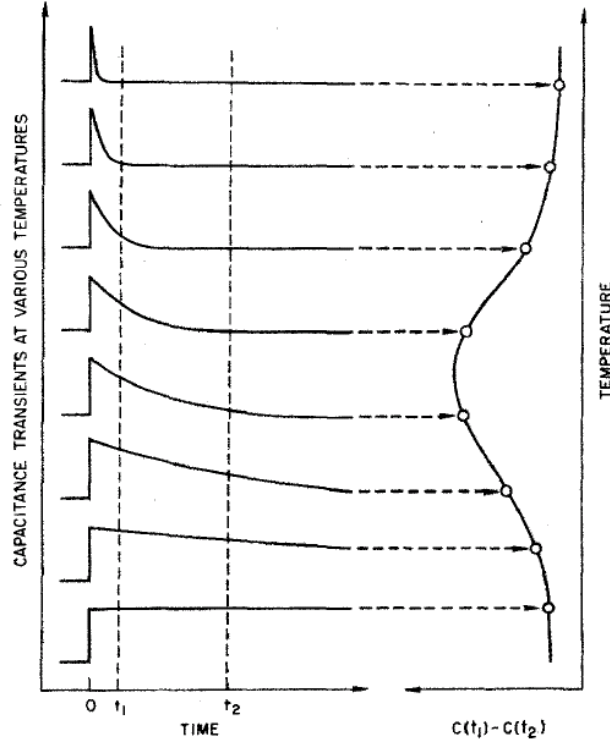


**Figure 4.9.** Dependence of the transient on temperature, and DLTS signal related to the rate window.

By repeating the scan with different rate windows, i.e. by changing the instants  $t_1$  and  $t_2$  in fig. 4.9, sets of values of  $I$  and  $T_{pk}$  are obtained. From these values the trap energy and apparent capture cross section can be extracted by considering the linear dependence of the quantity  $\ln(T^2/e_p)$  on the reciprocal temperature (see eq. 4.66b).

$$e_p = \frac{\sigma_p \langle v_p \rangle N_V}{g} \exp\left(-\frac{\Delta E}{kT}\right). \quad (4.66b)$$

The product  $\langle v_p \rangle N_V$  is proportional to  $T^2$ , thus  $\ln(T^2/e_p)$  is linearly dependent on the reciprocal temperature:

$$e_p = \sigma_p \gamma T^2 \exp(-\Delta E/kT). \quad (4.76)$$

The trap energy is related to the slope of the line,  $B$ :

$$\Delta E = 1000kB \quad (4.77)$$

whereas the capture cross section is related to the intercept with the  $y$  axis,  $A$ ;

$$\sigma = \frac{1}{\gamma \exp(-A)} \quad (4.78)$$

## 4.5 Scanning electron microscopy

Scanning electron microscopy is a useful tool for a high-resolution analysis of surfaces. The variety of interactions between electrons and solids allows a versatile way of characterization.

In a SEM electrons are used for analysis. An electron gun provides electrons by thermoionic or field emission. The electron beam, which typically has an energy ranging from a few hundred eV to 50 keV, travels towards the sample passing through a series of magnetic lenses designed to focus the beam to very fine spot. The focused beam passes through pairs of scanning coils in the objective lens, which deflect the beam in a raster fashion in order to scan a rectangular area of the sample surface. The electron beam is focused by one or two condenser lenses into a beam with a very fine focal spot. When the beam hits the sample surface the electron beam is deflected in various directions and spreads in a volume, known as the interaction volume. Interactions in this region lead to the emission of secondary electrons which are detected to produce an image. Several types of interactions take place, thus leading to several types of images produced by backscattered electrons, secondary electrons, transmitted electrons, or Auger electrons. Other phenomena caused by the incident beam are formation of electron-hole pairs, leading to electron beam induced conductivity, and cathodoluminescence. The signal is then revealed by a detector and an image is formed and presented on the screen of a Cathode Ray Tube. The correspondence between the spots excited by the beam and pixels on the CRT is the essential feature of a SEM [Armigliato].

### 4.5.1 Beam-sample interaction

An accelerated electron incident on a solid undergoes two main kinds of interaction:

Elastic diffusion, which deflects the electrons without changing their energy.

Anelastic diffusion, in which electron lose energy, but do not change their direction. The latter is the process that produces all types of signal except for backscattered electrons. The electrons of the external orbitals, the most weakly bound, are expelled from the solid. Since these electrons have low

energies, only the ones generated near the surface have energy enough to overcome the surface barrier of the material and get out of the solid.

Due to the wide nature of events that take place in the beam solid interaction, the physical model of the interaction is rather complex. An analytical expression of the decrease in energy per unit length is [Armigliato]

$$-\frac{dE_m}{dx} = 2\pi e^4 N_0 \frac{Z}{A} \frac{\rho}{E_m} \ln \frac{1.1666 E_m}{J} \quad (4.79)$$

where  $e$  is the electron charge,  $\rho$  is the material density,  $Z$  is the atomic number,  $A$  is the atomic weight,  $N_0$  is the Avogadro number,  $E_m$  is the mean energy of the beam (keV), at the length  $x$  measured along the effective path of the electron, and  $J$  is the mean ionization potential of the hit material.

The term  $I$  represents the mean energy loss of the incident beam for each anelastic interaction, and increases with  $Z$ .

The elastic scattering can be divided into two contributions: Rutherford diffusion, by the coulomb potential of the nucleus, and multiple diffusion, which consists in a series of small angle deviations along the path, due to the coulomb interaction with the nuclei screened by the electrons. The maximum distance of an electron before a high angle deviation varies with  $Z$ . Thus, electrons penetrating into a solid with a low atomic number have high angle diffusion probability lower than electrons penetrating into a solid with high atomic number. As a consequence the interaction volume has a drop-shape for solids with low atomic numbers, and hemispherical for solids with high atomic numbers, as illustrated in figure 4.10 [Armigliato].

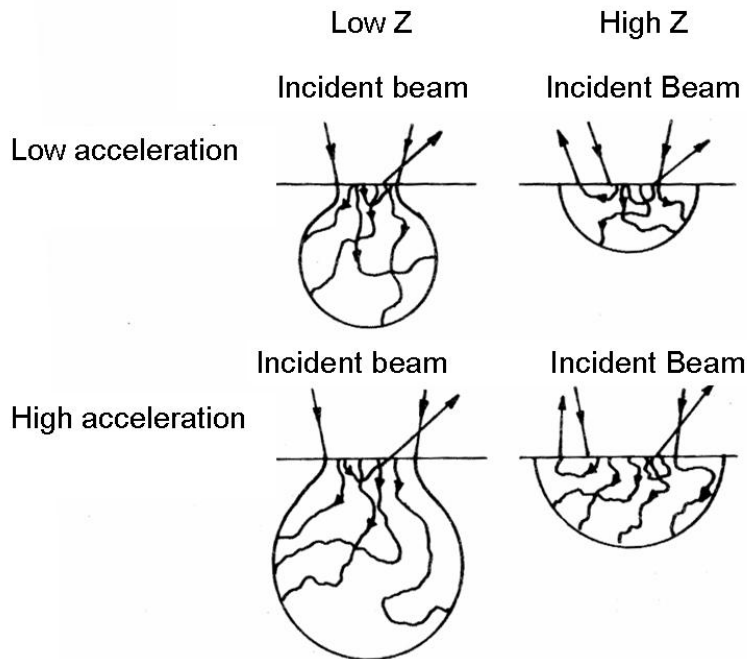


**Fig. 4.10. Interaction volumes of the incident beam with a solid as a function of the beam energy in case of low and high atomic number**

The full penetration range of electrons is expressed by the empirical relation [Maximenko]:

$$R = \frac{4.28 \times 10^{-6}}{\rho} E_m^{1.75} \quad (4.80)$$

Where  $\rho$  is expressed in  $\text{gcm}^{-3}$  and  $E_m$  in keV.

#### 4.5.2 Images by secondary electrons

Images by secondary electrons are the most frequently used to analyse sample surfaces. Since secondary electrons have low energy (<50 eV) it is possible to detect only electrons that originate within a few nanometers from the surface. The electrons are detected by a photomultiplier, and the resulting signal is rendered into a two-dimensional intensity distribution. The brightness of the signal depends on the number of secondary electrons reaching the detector. If the beam enters the sample perpendicular to the surface, then the activated region is uniform about the axis of the beam and a certain number of electrons "escape" from within the sample. As the angle of incidence increases, the "escape" distance of one side of the beam will decrease, and more secondary electrons will be emitted. Thus steep surfaces and edges tend to be brighter than flat surfaces, which results in images with a well-defined, three-dimensional appearance. On the contrary cavities tend to be darker because of the shadow effect of the surrounding area.

The number of secondary electrons depends on the beam energy and on the atomic number of the target. Thus, different sample compositions can be revealed by SEM.

#### 4.5.3 Electron beam induced current

The nature of the SEM's probe, energetic electrons, makes it uniquely suited to examine the optical and electronic properties of semiconductor materials. The high-energy electrons from the SEM beam will inject charge carriers into the semiconductor. Thus, beam electrons lose energy by promoting electrons from the valence band into the conduction band, leaving behind holes.

If the sample contains an internal electric field, such as in a p-n junction, the SEM beam injection of carriers will cause electron beam induced current (EBIC) to flow.

The current is revealed through a circuit illustrated in fig. 4.11.

When a beam hits a solid the currents that are formed are: the beam current  $I_p$ , the secondary electron current  $I_s$ , the backscattered electron current  $I_b$ , and a current of absorbed electrons  $I_a$ .  $I_a$  is produced by the fact that  $I_p - I_b - I_s \neq 0$ , thus the tendency of the sample to get charged is balanced by the current  $I_a$ , flowing from the sample to the mass of the circuit.

$$I_a = I_p - (I_b + I_s) \quad (4.81)$$

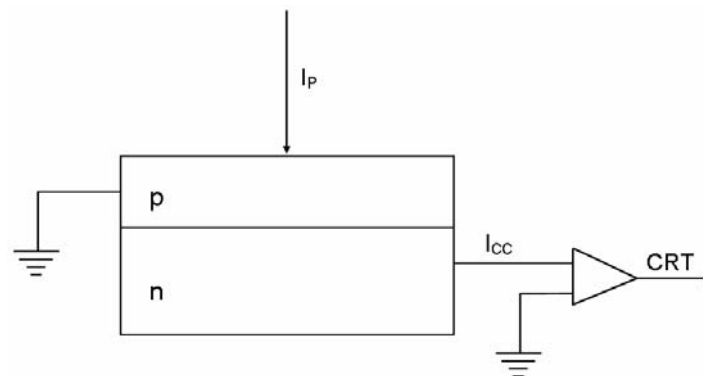


**Figure 4.11. Equivalent circuit for an EBIC measurement on a p-n junction.**

This relationship shows that  $I_a$  is complementary to the current of emitted electrons  $I_b + I_s$ . This does not necessarily mean that the contrast in EBIC images is the opposite as in SEM images. In fact, the EBIC contrast is also related to variations in the collection efficiency, due to recombination centres or variations in the internal electric field that separates the charges. A comparison between secondary and EBIC images allows a study of nanoscale features and defects.



## Chapter 5

### Electrical characterizations

The experimental results for the complete characterization of the process described in chapter 3 are reported. Sheet resistance measurements and SCM measurements were used to evaluate the electrical activation of the implanted phosphorus. AFM and SEM micrographs are reported to illustrate the effect of the annealing on surface morphology. The electrical performance of the diodes were evaluated by I-V measurements with the ohmic contact on the  $n^+$  regions was made up of nickel as deposited. C-V measurements on the  $n^+/p$  diodes and on the Schottky diodes were carried out in order to measure the apparent acceptor concentration in the epilayer and under the implanted regions.

The effect of the alloy treatment for the formation of nickel silicide was analysed. TLM measurements were carried out to measure the contact resistivity of the diodes. A comparison between the I-V curves of the diodes before and after the alloy treatment was made to evaluate the change in the series resistivity of the diodes produced by the better ohmic contact. The I-V curves of the diodes underwent deterioration after the alloy treatment, thus DLTS and some EBIC analyses were made in order to understand the origin of such behaviour.

Finally, the analysis of the electrically active defects in the p-type epilayer is reported.

#### 5.1 Experimental setup

The I-V and C-V measurements were carried with an automatic, computer controlled instrumentation made up of:

MM6620: For wafer movement and contact (prober, Micromanipulator)

K707: Switching matrix (Keithley 707)

K90: Apparatus made up of 4 current and voltage source-measure units (Keithley 238) and a trigger unit (Keithley 2361). This apparatus was employed for I-V measurements. The minimum current sensitivity is 100 fA

K82 Apparatus for C-V measurements, made up of a voltage source (Keithley 230) and a C-V analyser (Keithley 590) and a interconnection system (Keithley 5951). The maximum sensitivity is 0.1 fF.

DLTS measurements were carried out with a setup from SULA Technologies. Temperature control was tuned by a Lakeshore 330. The measurements were

carried out in air. For low temperature measurements liquid nitrogen was employed for sample cooling.

EBIC analyses were performed in a Philips 515 Scanning Electron Microscope.

## 5.2 Devices and test geometries

Fig. 5.1 shows the layout of a die in the sample. The sample was made up of a periodic repetition of this layout. Different types of devices can be identified.

- $n^+/p$  diodes
  - D1: 250  $\mu\text{m}$  diameter. 4 devices/die
  - D2: 400  $\mu\text{m}$  diameter. 4 devices/die
  - D3: 600  $\mu\text{m}$  diameter. 4 devices/die
  - D4: 800  $\mu\text{m}$  diameter. 3 devices/die
  - D5: 1000  $\mu\text{m}$  diameter. 3 devices/die
  - D6: 400  $\mu\text{m}$  diameter. 4 devices/die
  - D7: 150  $\mu\text{m}$  diameter. 4 devices/die
- Schottky diodes
  - S1: 400 $\mu\text{m}$  diameter. 4 devices/die
- VdP: Van der Pauw structure 450 $\mu\text{m}$ ×450 $\mu\text{m}$ . 1 device/die
- TLM: TLM structure. The pads of the TLM structures were 100 $\mu\text{m}$ ×100 $\mu\text{m}$ . The distances between consecutive pads were: 3, 5, 15, 25, 35, 45, 55  $\mu\text{m}$ . The distance of each pad from the border of the implanted region is 25  $\mu\text{m}$ . 1 device/die.

The diodes of circular shape, and different diameter were electrically characterised by I-V and C-V measurements, before and after the formation of nickel silicide.

The characterization of the process was carried out on the test geometries (VdP, TLM and Schottky diodes) in order to monitor different process parameters.

The electrical activation of the dopants was evaluated by sheet resistance measurements on Van der Pauw structures and SCM measurements on blanket  $P^+$  implanted samples.

TLM structures were employed for the characterization of the nickel and nickel silicide contacts on the  $n^+$  regions.

The study of the electrically active defects in the material, either native or introduced by processing, was carried out by DLTS measurements on  $n^+/p$  diodes and on Schottky diodes.

EBIC analyses were performed to investigate the presence of localised regions with different conduction properties in the diodes.

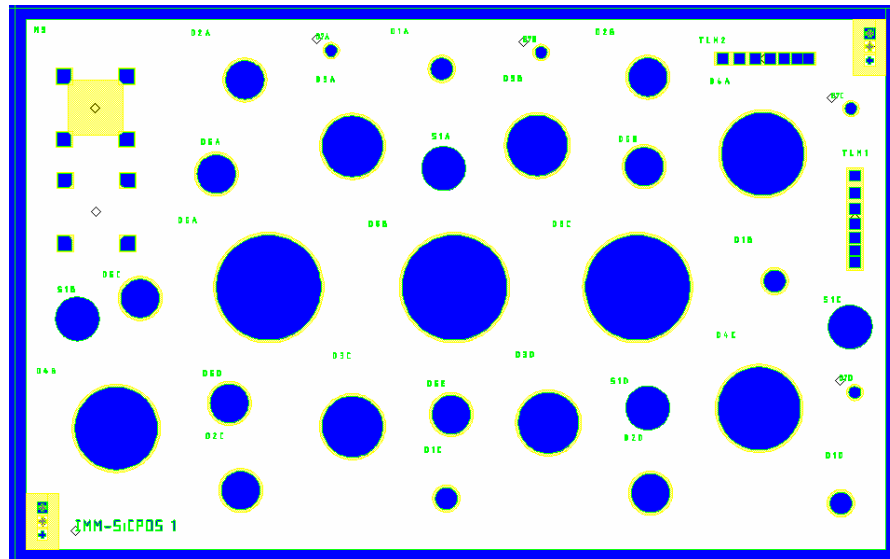


Fig. 5.1. Layout of a die in the sample. The  $n^+$  implanted regions are yellow, the emitter contacts are grey.

### 5.3 Dopant activation

The post implantation annealing is a necessary step in order to electrically activate ion implanted dopants. The fraction of electrically active atoms increases with increasing annealing temperature. Fig. 5.2 shows the values of sheet resistivity obtained on samples implanted and annealed at different temperatures.

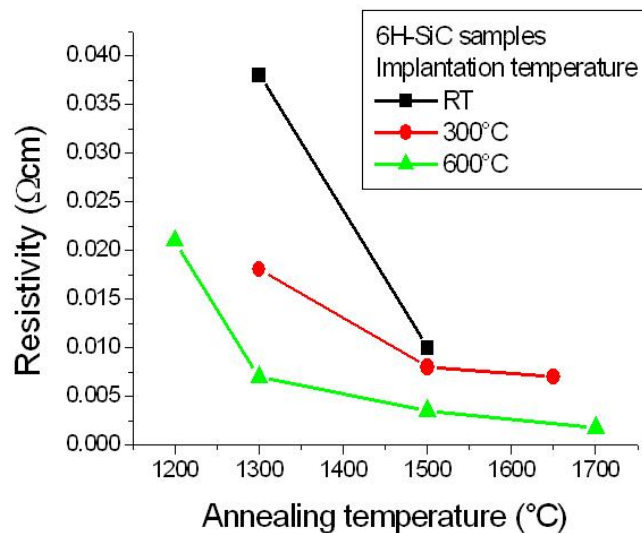
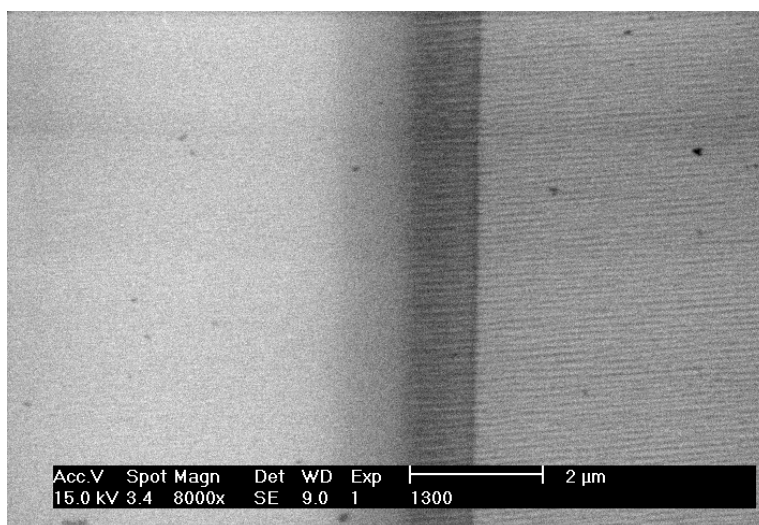
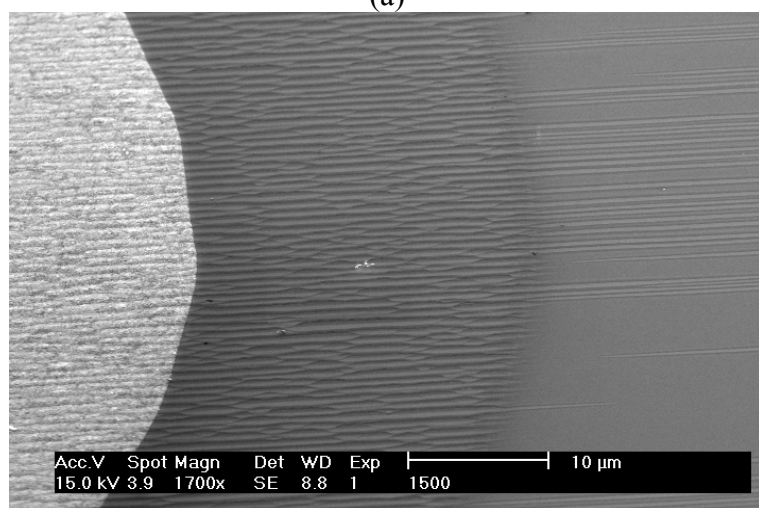


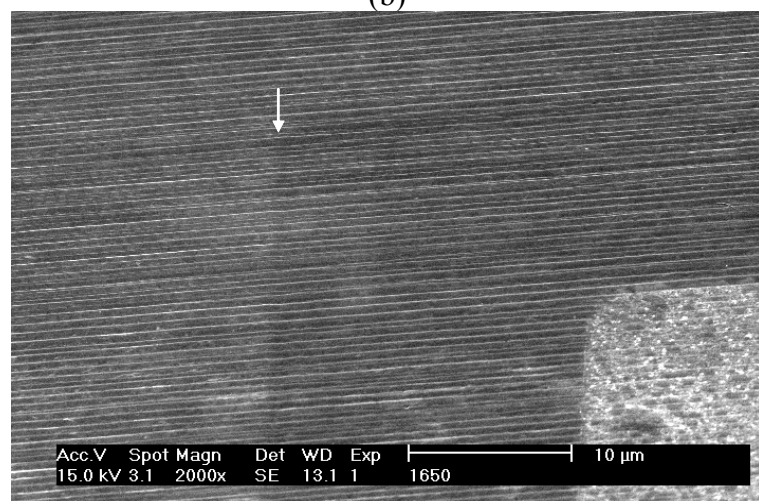
Figure 5.2. Resistivity vs annealing temperature of samples implanted with P at room temperature (black), 300 °C (red) and 600 °C (green) , [Poggi2004, Capano, Pensl].



(a)



(b)



(c)

**Figure 5.3. SEM micrographs of the surfaces of the samples annealed at (a) 1300 °C, (b) 1500 °C and (c) 1650 °C for 20 minutes in argon**

Fig. 5.3 shows the effect of the annealing temperature on SiC surfaces implanted at 300°C according to implantation schedule reported in Chapter 3 and annealed at 1300 °C (a), 1500 °C (b), and 1650 °C (c) for 20 minutes in argon [Poggi2004]. The step bunching phenomenon is nearly undetectable by SEM in the 1300 °C annealed sample. The implanted region (on the right) is featured by a light surface roughening, whereas the unimplanted surface is smooth. The 1500 °C annealed sample is step bunched in the implanted region (on the left), and furrows start propagating into the unimplanted region as well. The 1650 °C annealed sample is completely step bunched, with no difference between the implanted (right) and unimplanted (left) regions. In order to avoid step bunching, performing the annealing at temperature lower than 1500 °C is mandatory, for this implantation dose.

Taking into account the aim of lowering the annealing temperature phosphorus is more convenient than nitrogen because high dopant concentration can be achieved even with a low- temperature annealing. Phosphorus implanted layers to a concentration equal to a  $1 \times 10^{20} \text{ cm}^{-3}$  show sheet resistance values lower than  $600 \Omega/\text{sq}$  after annealing at 1200 °C [Capano2000-2].

In fig. 5.4, AFM micrographs of the surface in fig. 5.3 (a) is shown.

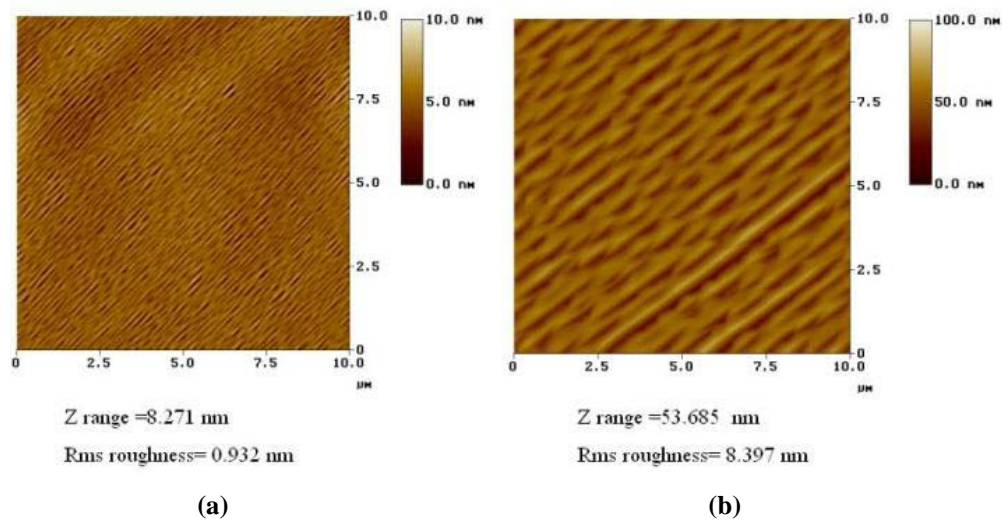


**Figure 5.4 AFM micrographs of the surfaces of two samples implanted to the same dose and annealed at 1300 °C (a) and 1400 °C (b). AFM micrographs were taken at the IMM-section of Catania.**

Step bunching and electrical activation of the dopants can be influenced by further parameters, like the ramp of temperature rise and fall. In fact, it was shown for N and P co-implants [Godignon], and Al implants [Poggi2006] that surface roughness increases, but sheet resistance decreases, with increasing ramp up rate. For N implants [Raineri] it was also shown that if a Rapid Thermal Annealing (RTA) at relatively low temperature precedes an annealing at high temperature and very low ramp up, the surface roughness decreases and the electrical activation increases with respect to those obtained

for the single annealing step with very low ramp up rate.

For phosphorus ion implantation it was observed that the use of a fast heating rate is detrimental for the surface smoothness. Figure 5.5 shows AFM micrographs of three samples, annealed at 1400 °C for 20 minutes, different only in the rate of temperature rise. It is evident that for a given annealing temperature, in this case 1400 °C, the surface roughness increases with increasing heating rate, in agreement with the results obtained for the post implantation annealing of implanted Al [Poggi2006]. These data also show that the surface smoothness is not degraded by a thermal treatment up to 1100 °C with a very fast ramp up, thus the critical temperature for the insurgence of surface roughness is in the range 1100-1400 °C.

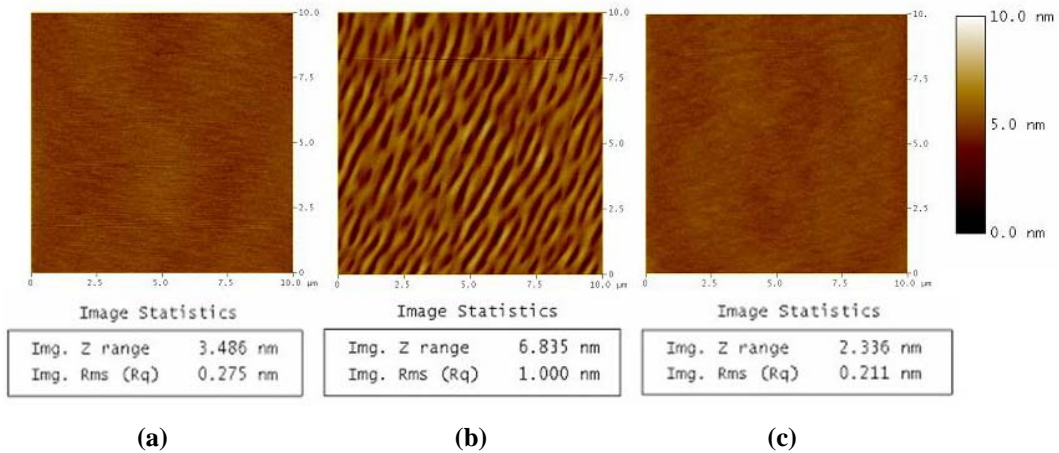


**Figure 5.5.** AFM micrographs of the samples annealed at 1400 °C for 20 minutes in argon. (a) ramp rate equal to 0.05 °C/s, (b) ramp rate equal to 40 °C/s, (c) RTA pre-treatment at 1100 °C before performing the annealing at 1400 °C. The ramp of the second annealing was 0.05 °C/s.

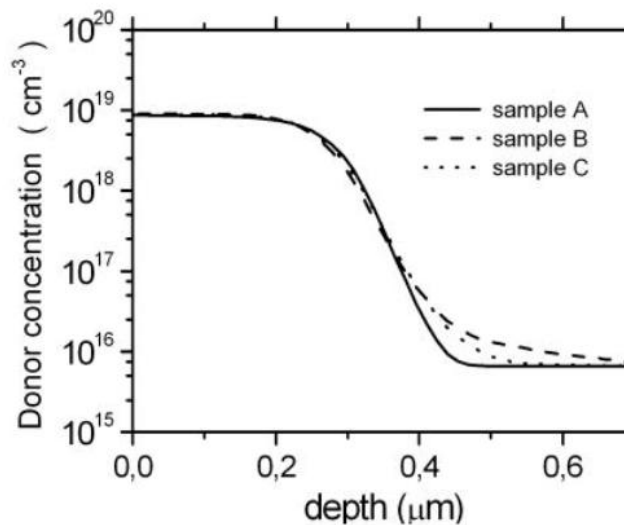


**Fig. 5.6.** SCM profiles of the electrically active P in the implanted layers subject to the different annealing rates.

SCM analyses (fig. 5.6) pointed out that the fraction of electrically active P atoms is about 13% of the total implanted fluence, and does not depend on the annealing process. SCM also shows that both a faster ramp up and a RTA pre-treatment at 1100 °C for 2 minutes have no considerable effect on the electrical activation of P.

## **5.4 Electrical characterizations of the diodes with the emitter contact in nickel as deposited**

### *5.4.1 Current-voltage measurements*

Current voltage measurements were carried out on the n<sup>+</sup>/p diodes in order to test their electrical performance. About 100 diodes of different area were characterized.

Some typical features of the I-V characteristics were identified. In forward bias the diodes were divided into three groups.

- 1) Diodes with forward I-V curve that can be analysed according to the Shockley-Read-Hall theory; the ideality factor calculated for these diodes was around 2-2.2 in the low current region. In the high current region the ideality factor was 1.4-1.6 before the series resistance contribution became dominant.
- 2) Diodes that show a moderate excess current in the low-current region. In the high current region the ideality factor was 1.4-1.6 before the series resistance contribution became dominant.
- 3) Diodes with high excess current; in this case the current is higher than the ideal Shockley Read Hall current for the whole exponential region, before the series resistance became dominant.

A schematic illustration of these trends is shown in figure 5.7. In reverse bias the diodes were divided into groups depending on the value of the current density at 100 V reverse bias. In a small group the current density is of the order of  $10^{-9}$ - $10^{-8}$  Acm<sup>-2</sup>, most diodes have current density around  $10^{-7}$ - $10^{-6}$  Acm<sup>-2</sup>, and a small group has current density equal to or higher than  $10^{-5}$  Acm<sup>-2</sup>.

The histograms in fig. 5.8 show the statistics of the values of the ideality factor in the low-current range (a), of the reverse leakage current (b), and of the leakage current density (c) at 100V reverse bias . The data in each histogram are referred to groups of diodes of the same area.

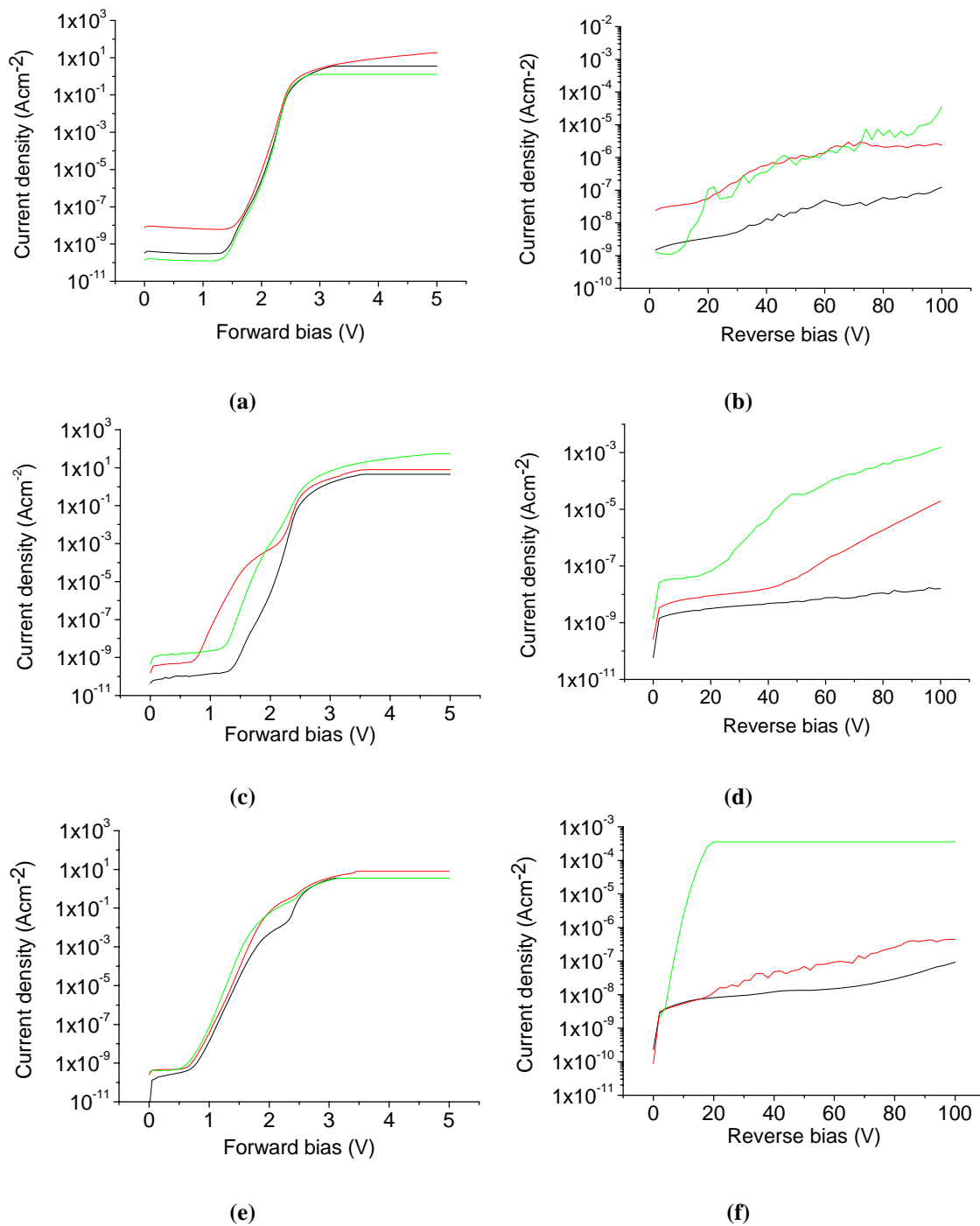


**Figure 5.7. J-V curves of diodes representative of the three groups. In forward bias: first group (a), second group (c), third group (e). For each group the reverse J-V curves are reported, in (b,d,f). The colours represent the division in groups according to the reverse current density at -100V:  $J < 10^{-7} \text{ Acm}^{-2}$  (black),  $10^{-7} \text{ Acm}^{-2} < J < 10^{-5} \text{ Acm}^{-2}$  (red), and  $J > 10^{-5} \text{ Acm}^{-2}$  (green).**

As the area of the devices increases:

- 1) The number of diodes that show excess current increases
- 2) The mean value of the reverse current density at -100 V ranges between  $10^{-7}$  and  $10^{-6} \text{ Acm}^{-2}$ , with a slight trend to increase with increasing area

3) The number of diodes that show breakdown at  $V < 100$  V increases. The theoretical breakdown value for these diodes is 1700 V.

The trend in 1) indicates that material plays a relevant role in the excess forward current, since as the diode area increases the probability of containing defects (either native or ion implantation induced) increases as well. Fig. 5.9 shows the map of the electrical behaviour of the devices. The devices marked with a yellow star have high forward excess current, whereas the pink squares indicate diodes in which breakdown occurs at reverse bias lower than 100V. The position in the wafer is a key parameter (fig. 5.9): diodes located in the same regions in the wafer show similar I-V curves. From this it can be inferred that diodes located in regions with a high density of defects show poor I-V characteristics.

As shown in fig. 5.7 (e,f), diodes featured by forward excess current can have either low or high reverse leakage current. This can indicate that the defects responsible of the excess current in forward bias are located near the junction, at the tail of the implanted region. Thus, residual implantation damage could be the cause of this phenomenon.

The diodes that do not present excess forward current have ideality factor equal to 2-2.2 in the low current range, which indicates that the dominant conduction mechanism is recombination of carriers through deep levels present in the band gap. As the current increases the ideality factor decreases to 1.4-1.6, which means that recombination and diffusion of carriers are both significant for electrical conduction. As current increases further, the sheet resistance contribution becomes dominant.

In reverse bias the current undergoes a slight increase with the applied bias, which indicates the presence of generation centres in the band gap over the whole depth of the epilayer.

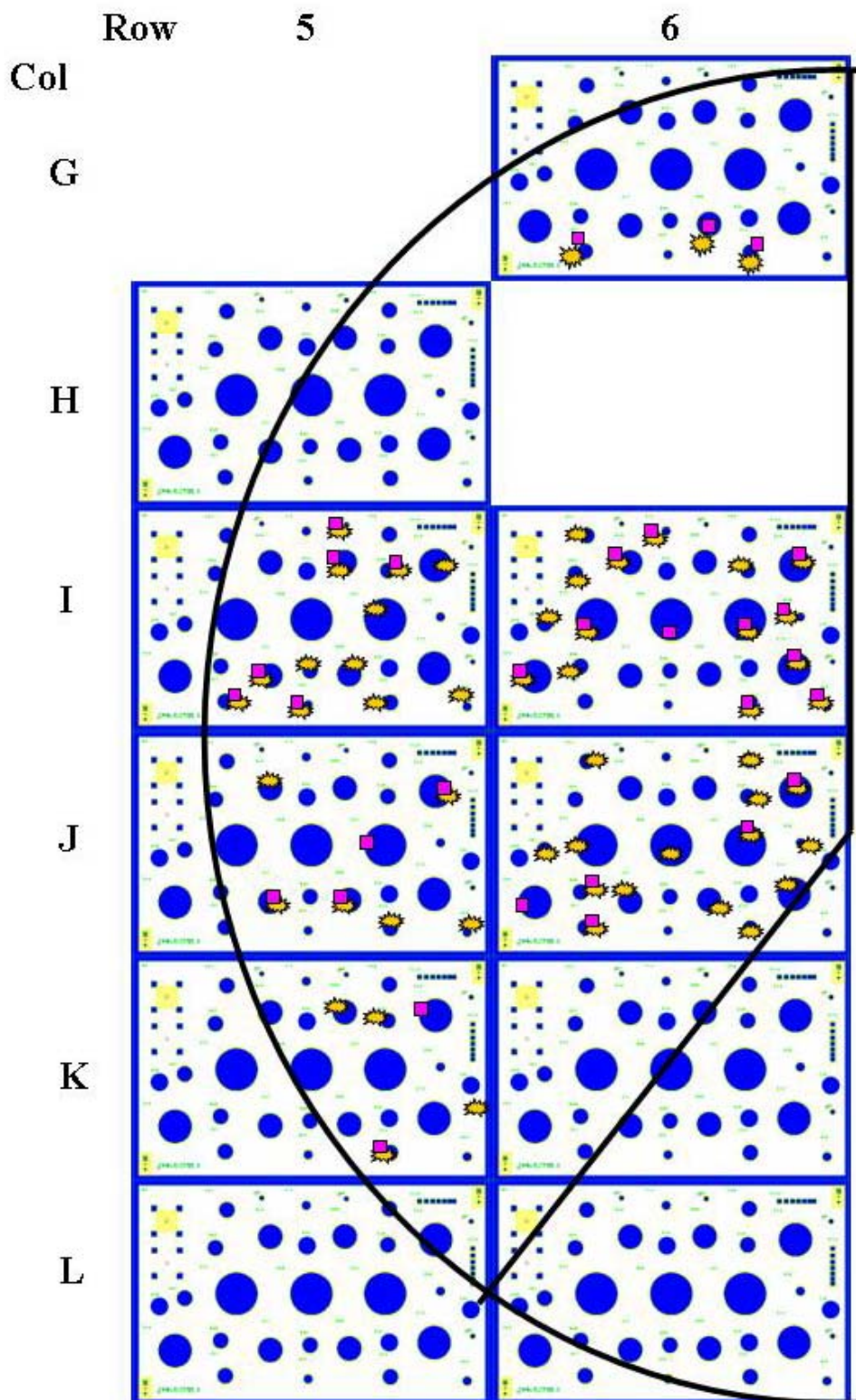


Figure 5.9. Layout of the sample. The devices that show high forward excess current are marked by a yellow star, the diodes that have breakdown at  $V < -100$  V are marked by a pink square.

### 5.4.2 Capacitance-voltage measurements

C-V measurements were performed on both  $n^+/p$  diodes and Schottky diodes all over the sample.

The C-V curves of the diodes were analysed in order to obtain a map of the uniformity of the apparent acceptor concentration in the epitaxial layer. A comparison of the apparent acceptor concentration profiles in the  $n^+/p$  and in the Schottky diodes allowed an evaluation of the extension of the implant tail in the epilayer.

In figure 5.10 the average values of the apparent acceptor concentration measured on the Schottky diodes are shown in a map of the sample.

The measured acceptor concentration is not uniform all over the wafer. The trend is the apparent acceptor concentration to increase in the dies of column 5 with respect to the dies of column 6, and with increasing line (from G to K), which means that it decreases the more the measured device is far from the flat.

	Col 5	Col 6	Col 7
G			$N_a = 7.3$
H	$N_a = 8.2$		
I	$N_a = 7.1$	$N_a = 6.8$	
J	$N_a = 7.1$	$N_a = 6.2$	
K	$N_a = 7.2$		

**Figure 5.10. Map of the apparent acceptor concentration in the epilayer.**

In figure 5.11 an example of the C-V curves obtained for these diodes is shown. The trend of the apparent acceptor profile not to be uniform all over the wafer is evident.

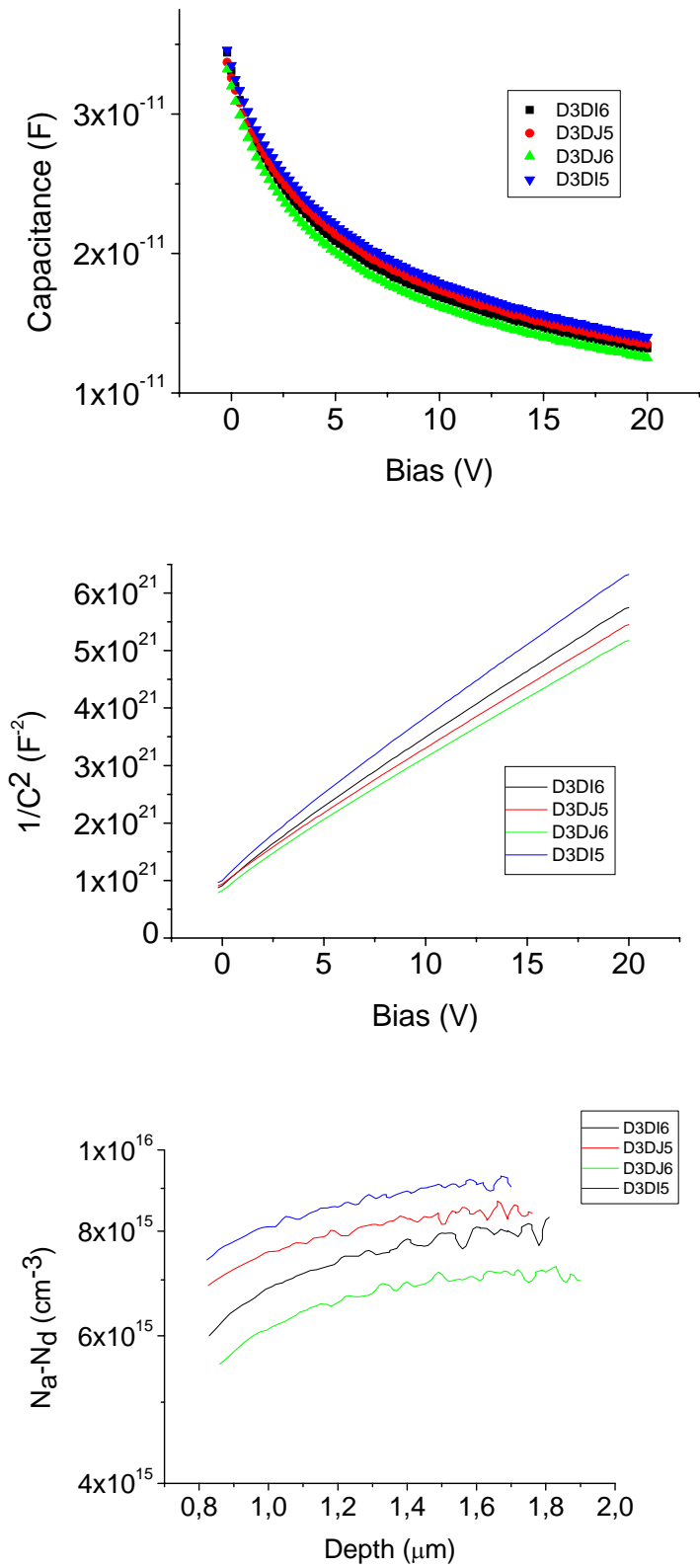


**Fig. 5.11.** C-V and  $1/C^2$  curves, and  $N_a$  vs depth profiles of some n<sup>+</sup>/p diodes. The position of the die in the wafer is reported.

The aim of the measurements on the n<sup>+</sup>/p diodes was to obtain a profile of the apparent acceptor concentration in the epitaxial layer under the implanted regions. A comparison of the profiles obtained on the n<sup>+</sup>/p diodes and on the Schottky diodes is shown in fig. 5.12. It is evident that a slight compensation in correspondence of the implant tail is present in our n<sup>+</sup>/p diodes. The nominal value for this epilayer was  $7.5 \times 10^{15} \text{ cm}^{-3}$ . The measured acceptor concentration measured in the Schottky diodes is in quite good agreement with this value, whereas in the n<sup>+</sup>/p diodes the apparent acceptor concentration approaches the nominal value only at depth higher than 1.2  $\mu\text{m}$ . The presence of an implant tail is also confirmed by the SIMS profile of the implanted phosphorus (fig. 5.13). In fig. 5.13 the presence of the implant tail is evident even though phosphorus could be revealed only in concentration higher than  $10^{17} \text{ cm}^{-3}$ .

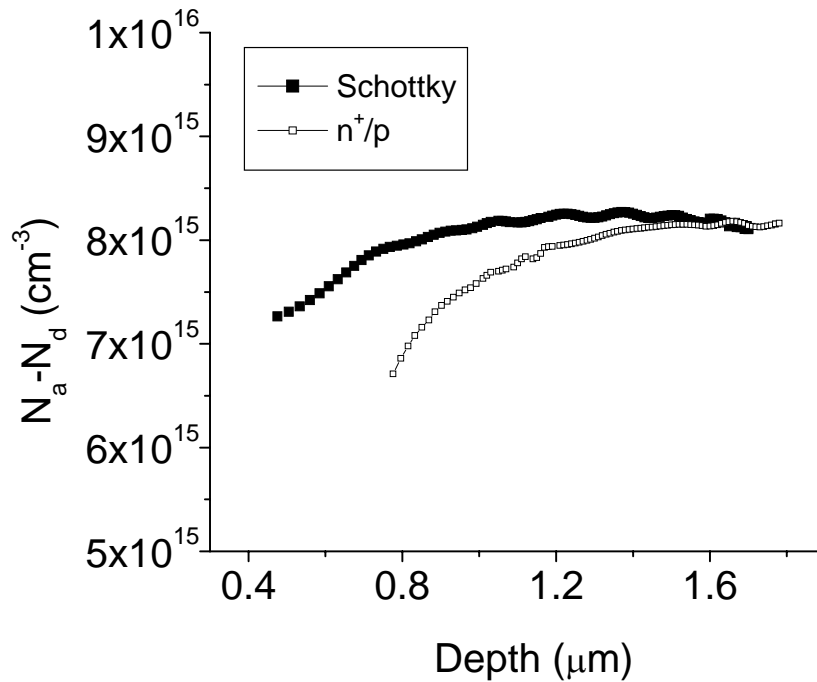


**Figure 5.12.** Apparent acceptor profile in the epitaxial layer, measured in a Schottky diode (full squares) and under an implanted region, measured in a n<sup>+</sup>/p diode (open circles).

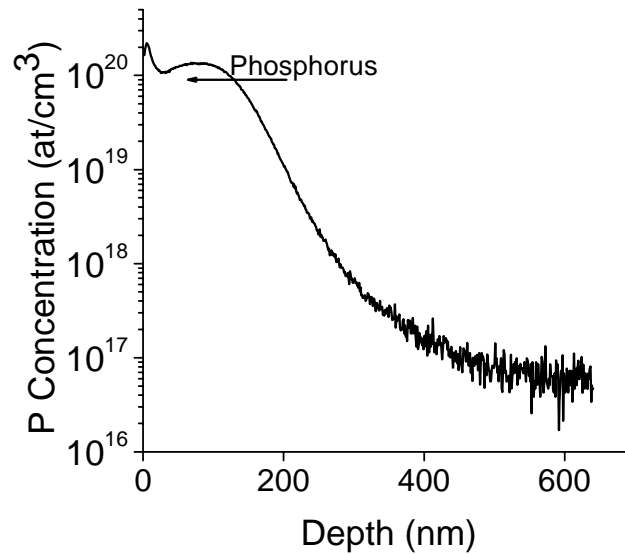


**Figure 5.13.** SIMS profile of the P atoms, compared with the simulated profile. SIMS analyses were carried out in Trento at ITC-irst (Trento)

## **5.5 Electrical characterizations of the diodes with the emitter contact in nickel silicide**

After the first electrical measurements the diodes underwent an annealing at 900°C for 1 minute in vacuum in order to form nickel silicide. This alloy treatment was done in the aim of achieving a low-resistance ohmic contact. It was demonstrated [Roccaforte, La Via, Moscatelli] that nickel silicide is a good candidate for the scope.

The diodes were the characterized by I-V measurements and C-V measurements. Contact resistance measurements were carried out on the TLM structures. Comparison of the DLTS spectra of the diodes with the emitter in nickel as deposited and in nickel silicide were done to investigate if the alloy treatment induced any changes in the defect structure of the diodes. EBIC analyses were performed to investigate the presence of localised highly conductive regions in the diodes.

### *5.5.1 Effect of nickel silicide on the contact resistance: TLM measurements*

TLM measurements were performed after the alloy treatment for the formation of nickel silicide on the TLM structures present in the H5 I5 J5 K5. Though several triangular features were observed near the TLM structure of

die H5, the values of contact resistivity and sheet resistance obtained on this structure are comparable to the ones obtained on the others.

In fig. 5.14 the resistance measured as a function of the distance between the pads is shown.

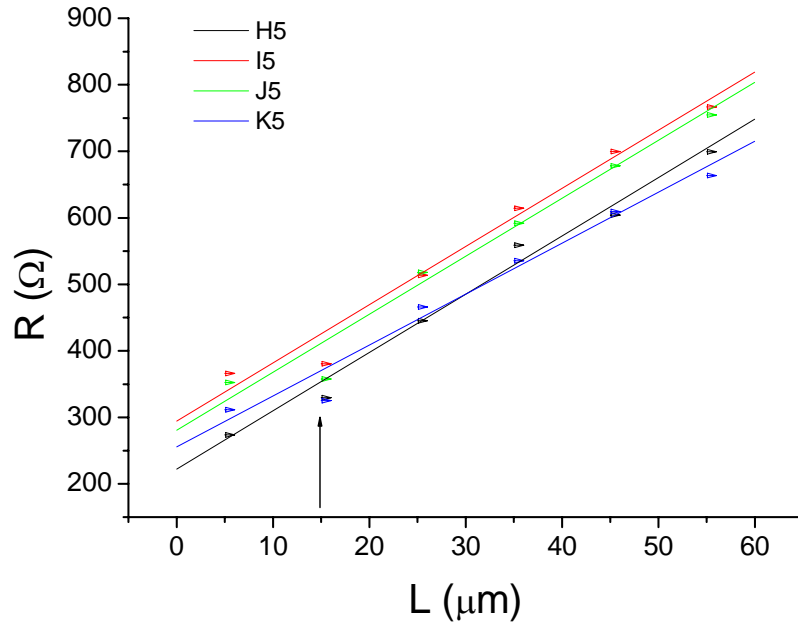


**Figure 5.14. R vs L plot. The measurements were carried out in the dies: H5, I5, J5 and K5. The arrow marks the measurements that scatter from the best fit line.**

It is evident from this plot that the resistance measured at 15μm distance is far from the linear fit. Thus, this value was neglected in our analysis (fig. 5.15).

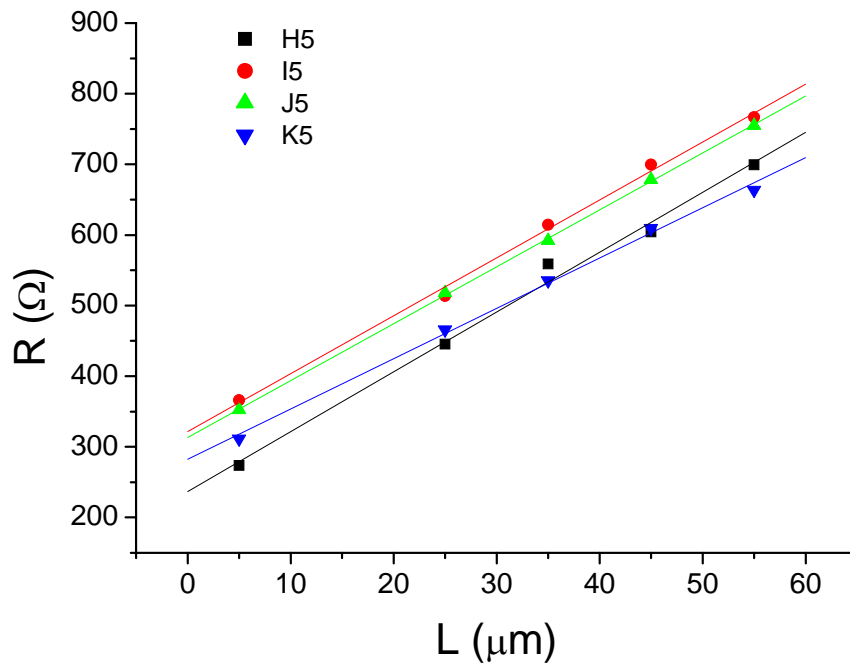


**Figure 5.15. R vs L plot. The value at 15 $\mu$ m distance were neglected.**

Table 5.1 shows the values of the contact resistance and of the sheet resistance. The sheet resistance obtained by TLM measurements is compared with the one obtained by measurements on VdP structures.

**Table 5.1. Results of Sheet resistance and contact resistance obtained from TLM measurements in the dies H5, I5, J5 and K5. The values of sheet resistance obtained from measurements on VdP structures is reported for comparison.**

Die	R <sub>sh</sub> VdP ( $\Omega$ )	R <sub>c</sub> ( $\Omega$ )	R <sub>sh</sub> TLM( $\Omega$ )
H5	1120	168	1270
I5	1150	160	1229
J5	1130	157	1208
K5	988	141	1067

The contact resistivity is 0.001-0.002 $\Omega$ .

Sheet resistance measurements on TLM structures give higher values than measurements on VdP structures.

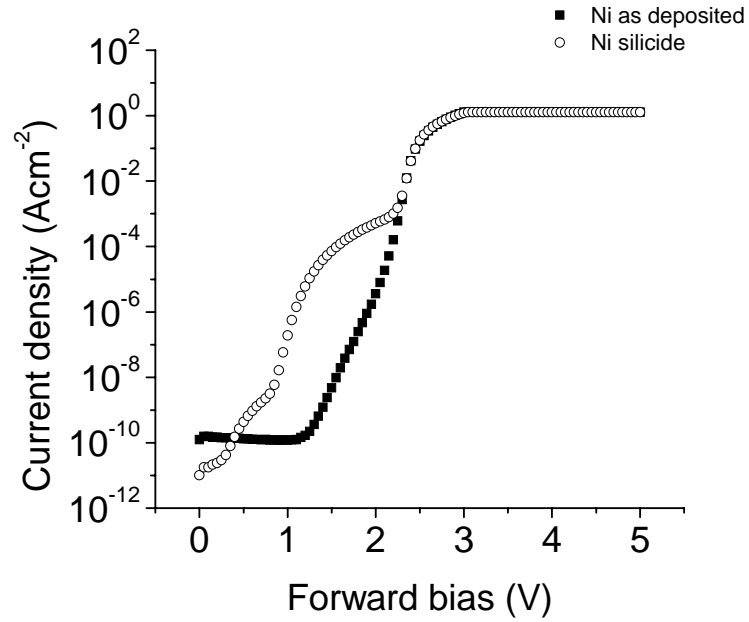
An attempt of performing these measurements was made also before the alloy treatment, but we could not obtain reliable values. This indicates that the emitter contact made up of Ni as deposited was not ohmic or highly resistive. Since TLM measurements on the contact made up of nickel silicide were reliable, we can conclude that this treatment had positive effect on the contact resistance.

### 5.5.2 Current- voltage measurements

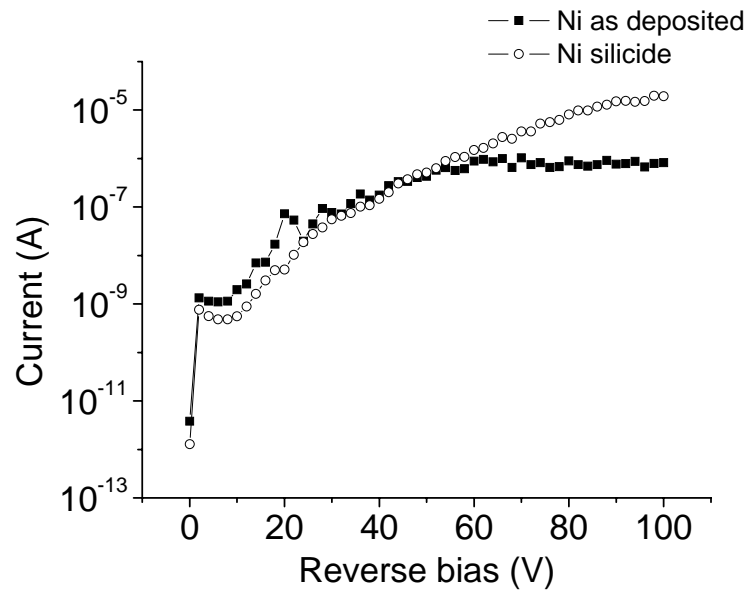
By comparing the values of the series resistivity of the n<sup>+</sup>/p diodes calculated from I-V measurements before and after the alloy treatment we observe that the silicidation makes the series resistance more uniform, yielding values ranging from 45 $\Omega$  for the diodes of 1mm diameter to 150  $\Omega$  for the diodes of 150 $\mu$ m diameter. The lowering of the series resistance is not evident in all the diodes. In the ones that had low series resistance even before the alloy treatment the value of the series resistance does not decrease further. A rough estimation of the contribution of the epilayer on the series resistance was made, obtaining values of the order of 50-100  $\Omega$  for the smallest diodes (D7) and around 2 for the biggest diodes (D5). This indicates that the epilayer gives a quite dominant contribution to the series resistance in the small diodes, whereas there is some different limiting factor to the reduction of the series resistance in the bigger diodes.

The alloy treatment induces also a change in the I-V curves of the diodes. In forward bias the excess current increases in many diodes, to an extent that varies for time to time. In reverse bias the leakage current increases as well, for high reverse bias values (higher than 50V). In fig. 5.16 an example of

increase of the forward excess current and of the reverse leakage current is shown.



(a)



(b)

**Figure 5.16. (a) Forward and (b) reverse J-V curves of the diodes. The black squares are the J-V curves of the diodes with the emitter contact in nickel as deposited, the open circles are the J-V curves the same device after the formation of nickel silicide.**

Two hypotheses were made on the cause of this change:

- 1) The further annealing induces the formation of electrically active defects, which act as generation-recombination centres in the current transport.
- 2) The reaction for the formation of nickel silicide consumes the  $n^+$  regions in one or more points, and a small Schottky diode in parallel with the  $n^+/p$  junction is responsible of the increase of the current.

The first hypothesis is supported by the fact that during the reaction for the formation of nickel silicide changes occur in the material: as an example, a carbon layer is formed and carbon at the interface Ni/SiC and vacancies are left in the material [Nikitina, LaVia 2003, Han]. These could act as generation recombination centres. Silicon atoms out diffusion, and consequent formation of voids in the material, was also reported [Heera]. An element against this hypothesis is that these defects should be concentrated towards the surface, and act mainly in the low-bias region of the reverse curve.

The latter is supported by the form of the forward I-V curve, since there is a rapid increase and then a plateau, similar to the I-V curve of a highly resistive Schottky diode. As its series resistance increases, the current flow through the  $n^+/p$  diode becomes the dominant contribution to the current. In reverse bias the Schottky diode is rectifying, thus we can not appreciate its contribution to the current, at least at low bias. With increasing reverse bias the leakage current of the Schottky diode increases, thus its contribution can be observed. Both hypotheses were tested. The formation of defects was investigated by DLTS, the presence of a localised region with different conduction properties was investigated by EBIC analyses.

#### *Results of the DLTS analyses*

In order to investigate the possibility that the alloy treatment induced the formation of defects we compared the spectra of diodes with the emitter contact in nickel and in nickel silicide.

Since the defects, if any, must have been towards the surface, the diodes were reverse biased at 5 V filled to zero bias for 10 ms. In this way the hole traps in a region between 0.7 and 1.1  $\mu\text{m}$  under the electrical junction were revealed. The measurements were carried out in a temperature range between 150 and 500 K.

In figure 5.17 a comparison between typical spectra of the diodes with the emitter contact in nickel and of the diodes with the emitter contact in nickel silicide is shown. There is no evidence of new kinds of defect, nor of any changes in the defect concentrations.

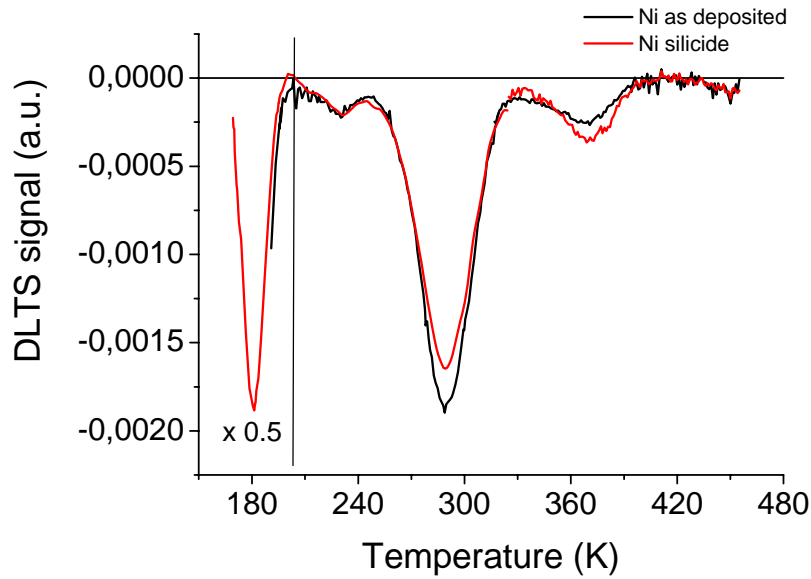
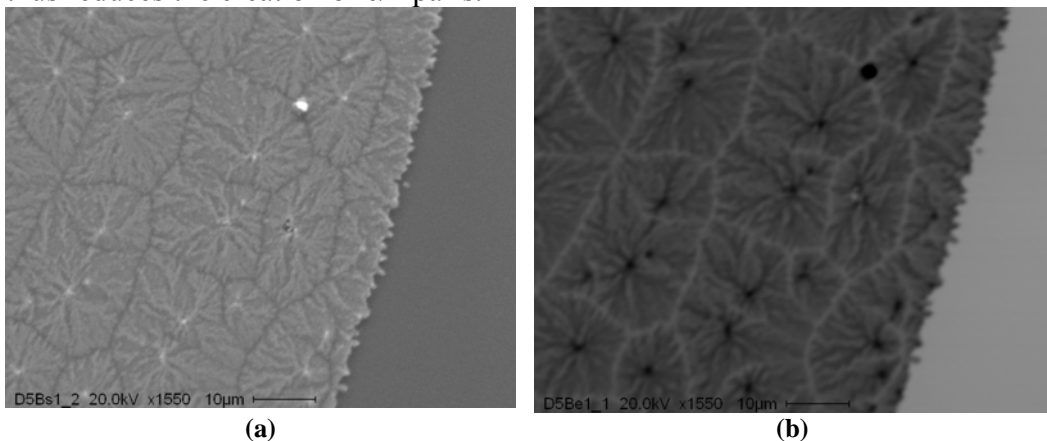


**Figure 5.17.** DLTS spectra of the diodes with the emitter contact in nickel (black line) and in nickel silicide (red line). Rate window  $46.51 \text{ s}^{-1}$ .

*Results of the EBIC analyses*

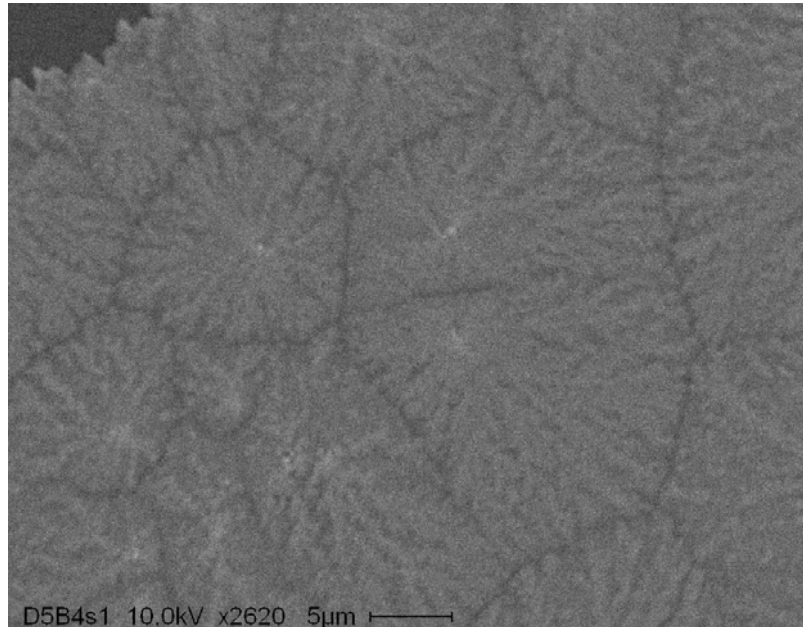
The presence of localised regions with different conduction properties was investigated through EBIC analyses. Several diodes were analysed, either showing excess current after the formation of nickel silicide or not.

Fig. 5.18 shows a SEM and an EBIC image of a portion of metal. The metal surface is rough, with brighter points that represent regions where the metal is thicker, and dark regions where the metal is thinner. In the EBIC image the contrast is the opposite because a higher mass of metal stops electrons and, thus reduces the creation of e/h pairs.

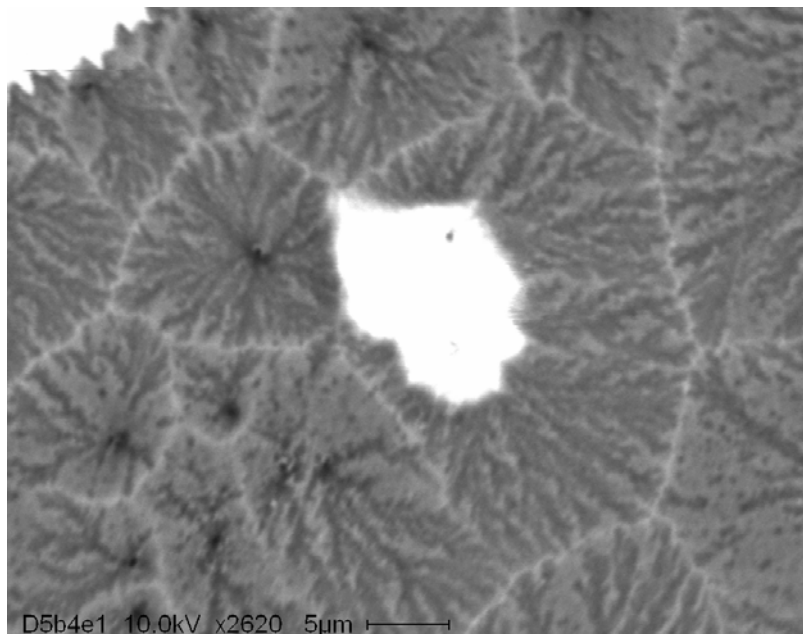


**Figure 5.18.** SEM (a) and EBIC (b) micrographs of a portion of metal on the  $n^+/p$  region after the alloy treatment.

In fig. 5.19 the SEM and EBIC images of a highly conductive region are shown. The localised highly conductive region appears very bright with respect to the rest. The SEM image does not reveal any difference in the metal surface. Similar regions can be seen in diodes in which formation of excess current occurs after the formation of nickel silicide, and were not observed in diodes where the current remains the same.



(a)



(b)

**Figure 5.19. SEM (a) and EBIC (b) images of a localised highly conductive region in a diode where excess current appears after nickel silicide formation. Beam energy 10 kV, magnification 2620x.**

A detailed analysis (fig. 5.20) revealed the influence of the metal pattern on the current through this region as well. The contrast given by the difference between the current through the two regions increases with decreasing beam energy, which indicates that the origin of the contrast is located towards the surface, probably at the Ni/SiC interface.

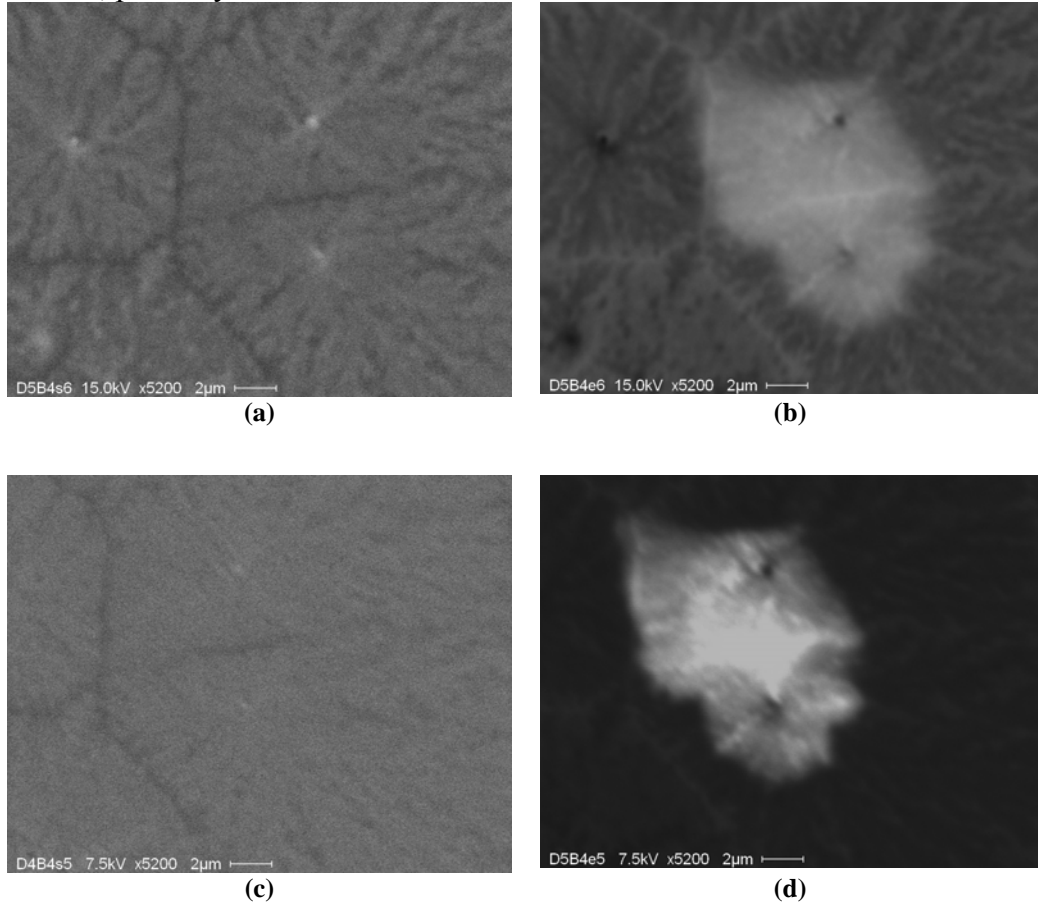


**Figure 5.20. SEM (a,c) and EBIC (b,d) images of the conductive area at 15 kV (a,b) and 7.5 kV (c,d) beam energy and 5200x magnification.**

### 5.5.3 Capacitance-voltage measurements

The C-V curves of the diodes before and after the silicidation did not undergo any change. This also indicates that the main changes do not occur in the SiC epilayer.

### Defects introduced by the ion implantation process

The investigation of ion implantation related defects was carried out by DLTS. These measurements allowed an identification of the hole traps in the epilayer. A comparison between the spectra of the  $n^+/p$  diodes and of the

Schottky diodes made it possible to identify the electrically active defects in the epitaxial layer and under the ion implanted regions. Since the long implant tail probably extends into the investigated regions, DLTS is a suitable technique for such analyses. The devices analysed were  $n^+/p$  diodes and Schottky diodes, with the emitter contact and the Schottky barrier made up of nickel silicide. This does not influence our results since no changes occurred in the DLTS spectra of the diodes before and after the alloy treatment.

Several diodes were characterized in the temperature range 150-650 K in order to explore energy values from the valence band edge to around midgap. This is because midgap levels are the most effective in the generation and recombination processes involved in the current transport. The Arrhenius plots were obtained by using emission rates ranging between 4.651 and 2326  $s^{-1}$ .

Different conditions of reverse bias and filling pulse were employed in order to study the depth dependence of the defect concentrations.

Fig. 5.21 shows a comparison of typical DLTS spectra obtained on the  $n^+/p$  diodes and on the Schottky diodes.

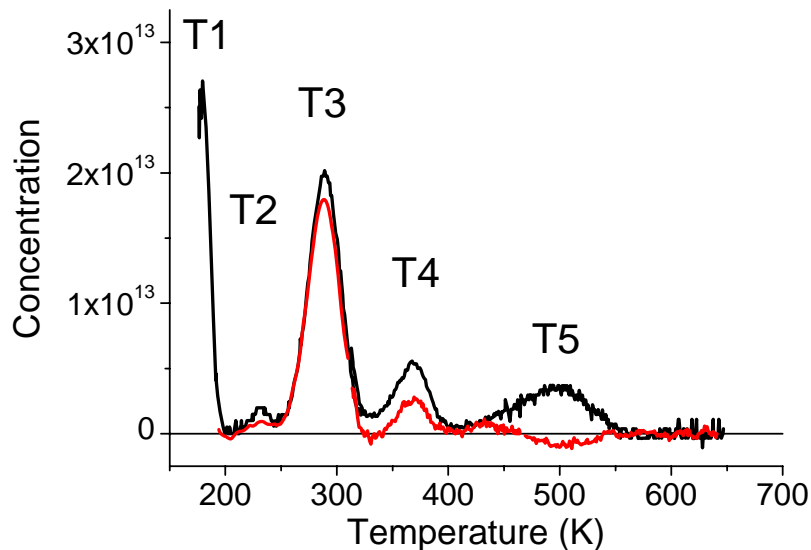


**Figure 5.21.** DLTS spectra of a  $n^+/p$  diode (black line) and a Schottky diode (red line). The diodes were reverse biased at 10V and filled to zero bias for 10ms. Rate window 46.51  $s^{-1}$ .

The DLTS spectra of the Schottky diodes differ from the ones of the  $n^+/p$  diodes because of presence of a broadened high temperature peak in the  $n^+/p$  diodes. We can infer that this peak is related to defects introduced by the ion implantation process.

Five peaks can be distinctly identified in the  $n^+/p$  diodes. Fig. 5.22 shows their Arrhenius plot.

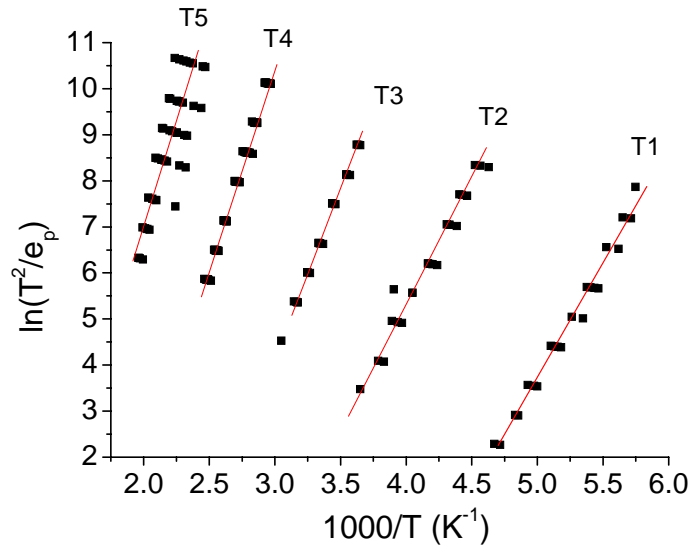


Figure 5.22. Arrhenius plot of the deep levels found in the diodes.

Table 5.2. Energy level, capture cross section, concentration and possible identification of the deep centers observed, extracted from the Arrhenius plot.

Trap	Apparent activation energy $E_T - E_V$ (eV)	Apparent capture cross section $\sigma$ (cm <sup>2</sup> )	Concentration @ -10,0,-10 V $N_T$ (cm <sup>-3</sup> )	Possible identification
T1	0.35	-	-	Shallow B [Lebedev]
T2	0.43	$1.2 \times 10^{-15}$	$7.0 \times 10^{12}$	P4 [Mitra]
T3	0.56	$2.8 \times 10^{-15}$	$7.3 \times 10^{13}$	Boron D-center [Lebedev, Rybicki]
T4	0.80	$2.0 \times 10^{-14}$	$1.5 \times 10^{13}$	De2 Di3 [Ghaffour]
T5	1.1	-	-	-

Table 5.2 summarizes the results for trap energy, apparent capture cross section, and concentration. From comparison with literature data an identification of the deep centres detected was attempted and is also reported. The determination of cross section and concentration of the level T1 was made difficult by the carrier freeze out, which causes the deformation of its peak. However, an approximate estimation of its activation energy is  $E_V + 0.35$  eV. This energy level is similar to that of the shallow boron acceptor caused by a B atom that displaces a Si atom in the Si sublattice [Lebedev]. Trap T2 was detected in very low concentration. The origin of this trap is unknown but a centre with similar energy and capture cross section, labelled P4, was detected by Mitra *et al.* [Mitra] in 6H-SiC MISFETs fabricated by N

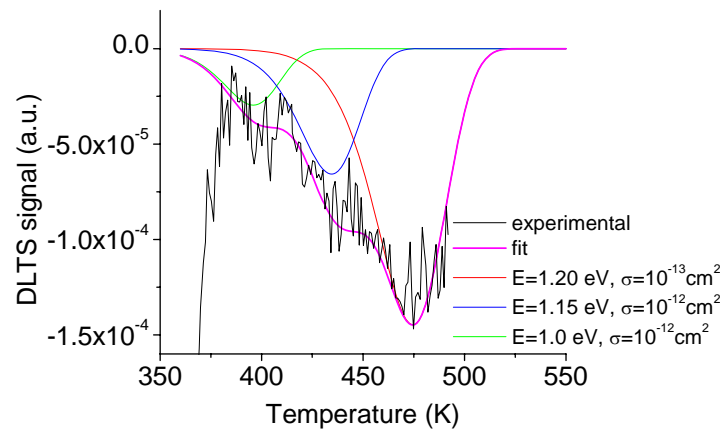
ion implantation. Trap T3 is related to the boron D-centre [Lebedev]. Trap T4, was located at  $E_V+0.80$  eV. Defects with similar energy and capture cross section were observed in N doped  $n^+/p$  diodes [Ghaffour, Mitra, Rybicki] and in Schottky diodes made on p-type SiC. In particular, Ghaffour *et al.* detected a deep level in both N implanted and epitaxial  $n^+/p$  diodes, named De2 and Di3, respectively, very similar in energy and capture cross section to the deep level at  $(E_V+0.80)$  eV found here.

The extraction of the parameters of trap T5 from the Arrhenius plot was made difficult by the fact that its peak was broadened and the peak position and height varied from a diode to another. Anyway we could estimate its energy level to be around 1.1 eV above the valence band edge. The values obtained from the Arrhenius plot for the capture cross section were unreliable.

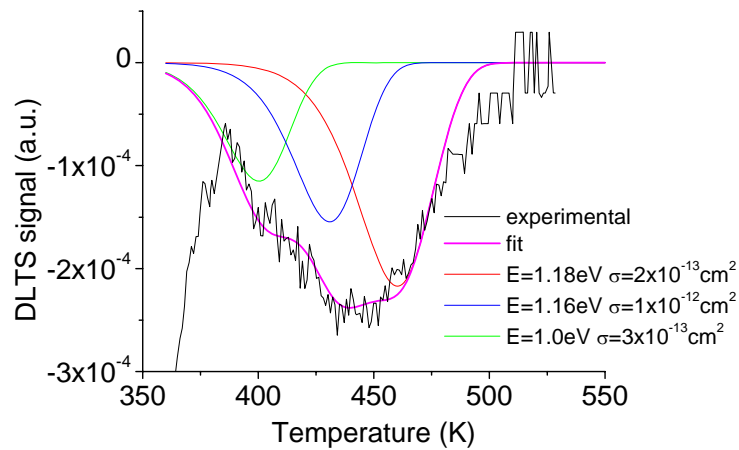
The analysis of trap T5 was carried out in several conditions of reverse bias and filling pulse and fitting procedure was employed. It was observed that this peak is in agreement with the DLTS spectra generated by considering a set of deep levels close in energy and capture cross section. In fig. 5.22 an example of fit of peak T5 is shown for two different diodes. The fit is in quite good accordance with the experimental data by considering three deep levels, namely A, B, and C, present in different concentration from one diode to another. In table 5.3 the fit parameters for the two devices are shown. It can be observed that the energy and capture cross section values are not exactly the same for both diodes. This can depend on the difficulty in resolving the peaks, but it also indicates that the energy levels of the defects that give rise to trap T5 are not sharp because in a damaged crystal the local environments of each lattice site are not exactly the same. Such behaviour was previously observed in amorphous silicon by Lang *et al.* [Lang1985]. In an amorphous material a single energy level gives rise to a distribution of levels. In this case trap T5 is generated by a discrete set of levels, probably because the material is not amorphous, but only damaged.

**Table 5.3. Energy, capture cross section and concentration of the deep levels used as fit parameters un fig. 5.22**

	E (eV)		$\sigma$ (cm <sup>2</sup> )		$N_T$ (cm <sup>-3</sup> )	
	D5B_I6	D4C_J5	D5B_I6	D4C_J5	D5B_I6	D4C_J5
A	1.20	1.18	$3 \times 10^{-13}$	$2 \times 10^{-13}$	$1.0 \times 10^{12}$	$1.5 \times 10^{12}$
B	1.15	1.16	$7 \times 10^{-13}$	$1 \times 10^{-12}$	$5 \times 10^{11}$	$1.0 \times 10^{12}$
C	1.0	1.0	$5 \times 10^{-13}$	$3 \times 10^{-13}$	$2 \times 10^{11}$	$8 \times 10^{11}$



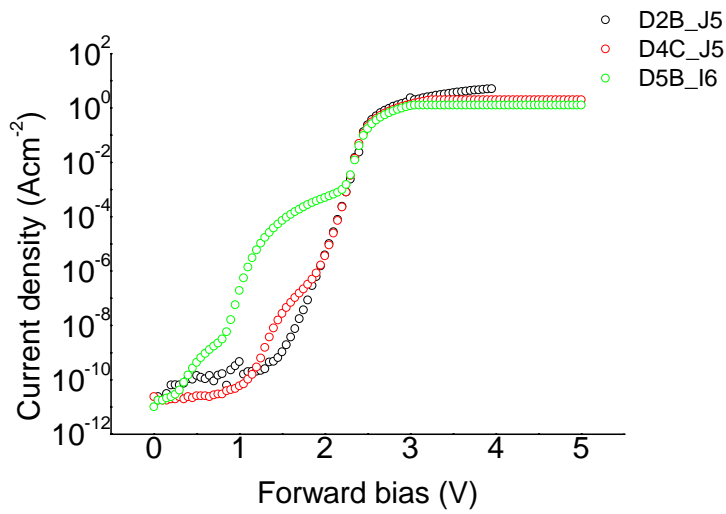
(a)



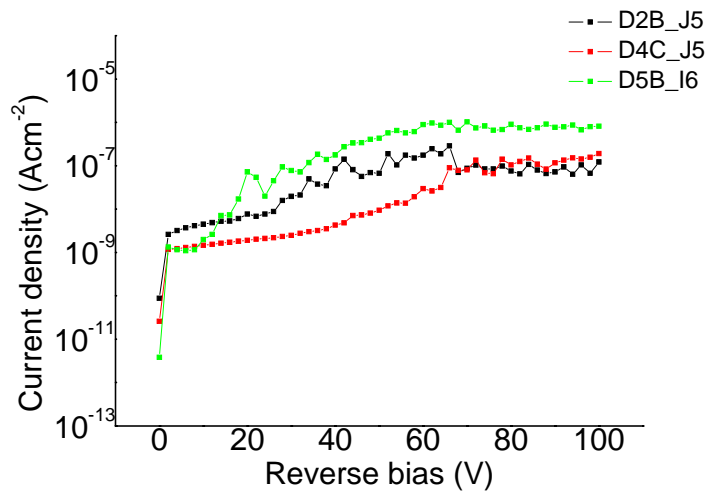
(b)

**Figure 5.22. Fit of the peak related to trap T5 in two different diodes**

In order to attempt a correlation between current transport and defects the analysis of trap T5 was made on several diodes. The diodes chosen had good electrical characteristics before the formation of nickel silicide. The deterioration of the J-V curves of the diodes is not attributed to any change in the defects of the material.



(a)



(b)

**Figure 5.23. Forward (a) and reverse (b) current of the diodes whose DLTS spectrum is shown in fig. 5.24 after the alloy treatment.**

We could not observe a unique behaviour of trap T5. The height and broadness of the peak varied from a diode to another. In fig. 5.24 an example of the possible shapes of the peak is shown.

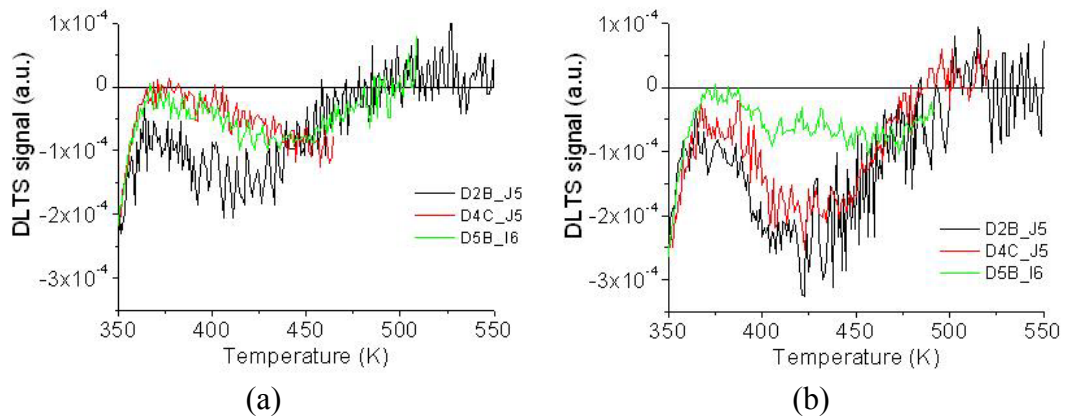


**Figure 5.24. DLTS spectra of the diodes at  $-10$  V reverse bias (a) and  $-5$  V reverse bias (b) in correspondence of trap T5. The diodes were filled to zero bias for 10 ms.**

Even if this level (set of levels) is located around midgap, its effect on the I-V characteristics of the diodes can not be proved. In fact, the leakage current density of all the diodes measured by DLTS was around  $10^{-7}$ - $10^{-6}$  Acm<sup>-2</sup>. Thus, the differences in the DLTS spectra can hardly be related to differences in the reverse leakage current. In forward bias the diodes had no excess current, when the emitter contact was made up of nickel as deposited. After the formation of nickel silicide the forward excess current increases in the diodes D4C\_J5 and D5B\_I6, but it did not increase in D2B\_J5. Thus, the differences in the peak position and height of the high temperature peak can not be related to the presence of forward excess current.

An identification of these traps can not be made, since no traps close in energy and capture cross section have been reported. From the increasing of the trap concentration with decreasing reverse bias (i.e. when the investigated region is closer to the junction interface), and from its absence in the Schottky diodes, it can be inferred that trap T5 is related to ion implantation. One more evidence of such correlation is the fact that trap T5 is made up of a set of levels, as it was observed also in heavily implanted materials [Lang1985]. Anyway phosphorus participation in this trap is not likely. First, because trap T5 was detected up to  $1.5 \mu\text{m}$  under the electrical junction, a depth much higher than the penetration depth of the implanted phosphorus. Second, because the most probable configuration for P atoms in SiC is in substitutional position in the Si sublattice ( $P_{\text{Si}}$ ). This configuration corresponds to a shallow donor level, that is not the present case. Thus, trap T5 is more likely related to lattice disorder created by the ion implantation and not completely removed by the low-temperature annealing.

In a small group of diodes one more deep level was observed. Its peak was a shoulder of the peak of trap T4. In fig. 5.25 the DLTS spectrum of a diode that contained T4a is shown in different conditions of reverse bias and filling pulse.

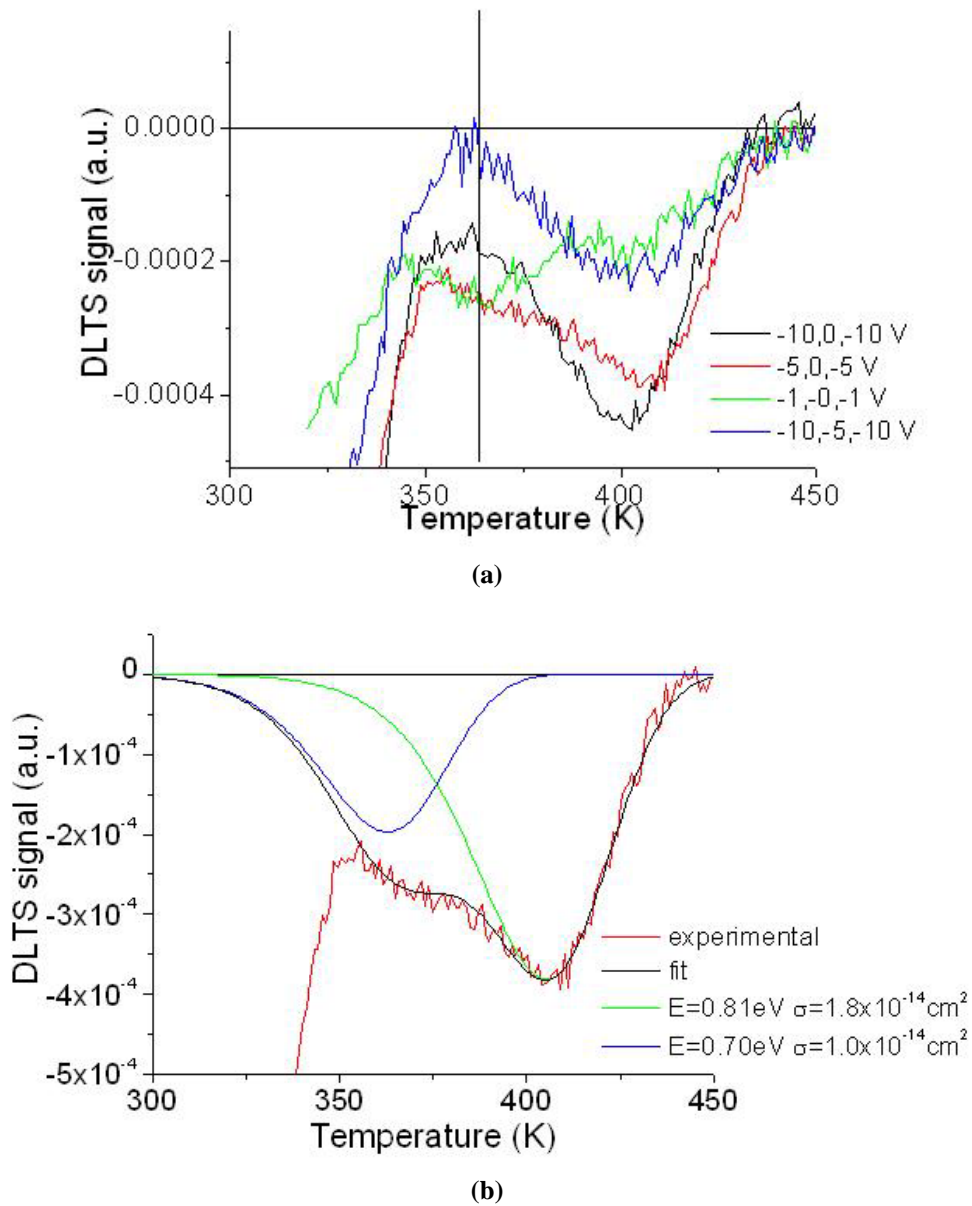
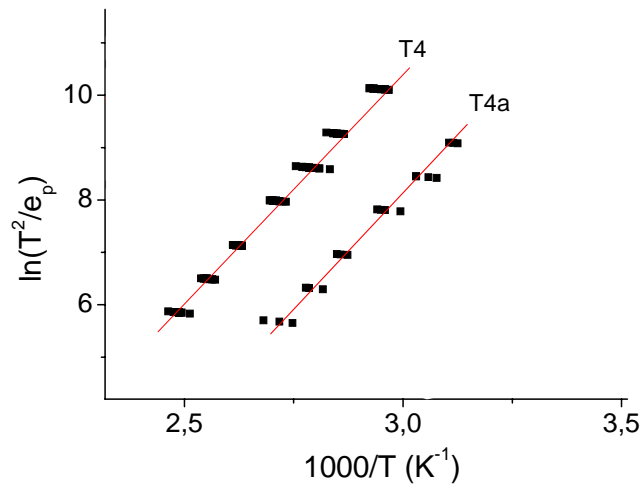


Figure 5.25. (a) DLTS spectrum of a diode in which the peak of trap T4a is visible. The diode was reverse biased at 10 V (black, blue), 5 V (red) 1 V (green) and filled to zero bias (black, red, green) or -5 V (blue). Rate window  $465.1\text{ s}^{-1}$ . (b) the same spectrum obtained for -5V reverse bias and 0 V filling pulse compared with the fit. The reported spectra correspond to  $4651\text{ s}^{-1}$ .



**Figure 5.26. Arrhenius plot of traps T4 and T4a.**

The trend to have an increase of the DLTS signal for decreasing reverse bias indicates that a high concentration of the defect related to trap T4a is located towards the surface of the sample.

By fitting this peak we found energy 0.70 eV and capture cross section  $1 \times 10^{-14} \text{ cm}^2$ . The influence of this deep level on the current transport was none, since it was found in diodes with different types of I-V curve. This result was expected since this peak is too near in energy to the valence band to be effective as a generation-recombination centre.

The identification of this peak is unknown. Since it is located near the surface a correlation with the ion implantation process is possible. A correlation with the silicidation could be excluded since this deep level was found both in diodes with the emitter contact made up of nickel and made up of nickel silicide. The correlation with ion implantation is also confirmed by the decrease of the signal generated by T4 with decreasing investigated depth in the diodes where T4a is visible. This may indicate that T4 and T4a are related to the same defect complex, whose energy undergoes slight variation depending on the local environment of the defect.



## Conclusions

A process of P<sup>+</sup> ion implantation suitable for industrial applications was proposed and characterized. The ion implantation was carried out at 300 °C in order to have a partial recrystallization of the lattice during the ion implantation and to achieve compatibility with industrial ion implanters. The post implantation annealing was performed at 1300 °C for 20 minutes in argon. The rate of temperature rise was 40 °C/s.

The electrical activation of the implanted phosphorus and the surface morphology were characterized for several annealing cycles.

Annealings were performed at temperatures ranging from 1300 °C to 1650 °C. Linear ramp rates from 0.05 °C/s to 40 °C/s, and the employment of a RTA pre-treatment before the annealing were also studied. Despite the increase of the electrical activation of the implanted species with increasing annealing temperature, the lowest annealing temperature yielded good sheet resistivity values, around 0.02 Ωcm. Furthermore the rms value of the surface roughness was lower than 1nm, that is a quite good morphology. A 1400 °C annealing yields a roughness around 9 nm, a ten times higher value.

The current voltage characteristics of the diodes were affected by the presence of defects in the material. The dependence of the electrical performance of the devices on their location in the wafer gives a hint that the anomalous I-V curves could be due to native defects. C-V measurements performed on the n<sup>+</sup>/p diodes and on the Schottky diodes revealed the presence of a slight compensation in correspondence of the implant tail, up to a depth of 1.2 μm under the electrical junction. DLTS measurements were carried out on the n<sup>+</sup>/p diodes and on the Schottky diodes in order to study the electrically active defects present in the epilayer and to find the ones related to the ion implantation process. Boron contamination and two deep levels attributed to native defects at 0.43 eV and 0.8 eV were revealed. A deep level at 0.7 eV was revealed in some diodes, probably related to the ion implantation, at depths lower than 1.2 μm. Its concentration increased closer to the electrical junction, but its average value was around 5×10<sup>11</sup>cm<sup>-3</sup> between 0.7μm and 1.2 μm under the implanted regions. A set of levels deep in the band (ranging from 1.0 to 1.25 eV) gap was attributed to lattice disorder created by the ion implantation process as well. These were present in very low concentration, and did not affect the I-V characteristics of the diodes. Even though residual defects introduced by ion implantation were left after the low-temperature annealing, their concentration was very low compared to the doping (7.5×10<sup>15</sup>cm<sup>-3</sup>) density and to the concentration of the native defects, and their effect on the electrical performance of the junctions could be neglected. Moreover the low-temperature annealing yields good electrical activation preserving the surface morphology. The absence of step bunching allows the

growth of good quality oxide on the surface, thus this process can be successfully employed for the fabrication of n-channel surface MOSFETs.

## References

- [Adjaye] Adjaye J, Mazzola MS, Los AV. *Mat. Sci Forum* 457-460, p. 1247 (2006)
- [Armigliato] Armigliato A, Valdrè U, *Microscopia Elettronica a scansione e microanalisi*, Univ. Bologna
- [Arora] Arora ND, Hauser JR, Roulston DJ, *IEEE Trans Electron Devices* ED29, p. 292 (1982)
- [Ashworth1990] Ashworth DG, Oven R and Mundin B, *J. Appl. Phys.* 23, p. 870 (1990)
- [Bakowski] Bakowski M, Gustafsson U, Lindefelt, *Phys Status Solidi A* 162, p. 421 (1997)
- [Bentini] Bentini G, Galloni R, *Impiantazione ionica*. Cooperativa libraria universitaria editrice, 1982
- [Blanqué] Blanqué S, Pérez R, Mestres N, Contreras S, Camassel J and Godignon P, *proceedings of ICSCRM 2005*, p. 795
- [Blood] Blood P, Orton JW. *The electrical characterization of semiconductors: majority carriers and electron states*. Academic Press, London (1992)
- [Bockstedte] Bockstedte M, Mattausch A and Pankratov O, *Mat. Sci. Forum* 457-460 p. 715 (2004)
- [Capano2000] Capano M, Cooper J, Melloch MR, Saxler A, Mitchel W, *Mat Sci Forum*, 338-342, p 703 (2000)
- [Capano2001] MA. Capano, *Applied Surface Science* 184, p. 317 (2001)
- [Capano2000-2] Capano M A, Santhakumar R , Venugopal R, Melloch MR and Cooper J A Jr., *J. Electron Mater*, 29, p. 210 (2000)
- [Chen] W. Chen and M. A. Capano *J. Appl. Phys.* 98, p. 114907 (2005)
- [Choyke] Choyke W J, Matsunami H and Pensl G, *Silicon carbide recent Major advances* Springer, Berlin (2004)
- [Nikitina] Nikitina, I P, Vassilevski, K V, Wright N G, Horsfall A B,

- O'Neill A G, Johnson C M, J Appl Phys, 97, p. 083709 (2005)
- [Eckstein1991] Eckstein W, *Computer simulation of ion-solid interactions*, Springer, Berlin (1991)
- [Ghaffour] Ghaffour K, Lauer V, Souifi A, Guillot G, Raynaud C, Ortolland S, *et al.* Mat Sci Eng B, 66, p. 106 (2001).
- [Groove] Groove AS. *Physic and Technology of Semiconductor Devices*. John Wiley and Sons, (1967)
- [Han] Han SY, Lee JL, J Electrochemical Soc, 149, p. G189 (2002)
- [Harris] Harris GL. *Properties of silicon carbide*. Inspec, (1995)
- [Heera] Heera V, Pankin D, Skorupa W, Appl Surf Sci 184 p. 307 (2001)
- [Inoue] Inoue N, Itoh A, Kimoto T, Matsunami H, Nakata T, Inoue M, J Electr Mat 26 p. 165 (1997)
- [Janson2003] Janson MS, Linnarsson MK, Hallén A and Svensson BG, J. Appl. Phys. 93, p. 8903 (2003)
- [Kopanski] Kopanski J, Marchiando JF, Berning D W, Alvis R, and Smith H E, J. Vac. Sci. Technol. B 16, p. 339 (1989)
- [La Via] La Via F *et al.*, Microelectronic Engineering, 60, p. 269 (2002)
- [La Via 2003] La Via F, Roccaforte F, Raineri V, Mauceri M, Ruggiero A, Musmeci P, Calcagno L, Castaldini A, Cavallini A, Microelectronic Engineering 70, p. 519 (2003)
- [Lang1974] Lang DV, J Appl Phys, 45 p. 3023 (1974)
- [Lang1985] Lang D V, Phys Rev B 25 p.5285 (1985)
- [Lazar] M.Lazar *et al.*, Mat. Sc. Forum 389-393, p. 827 (2001)
- [Lebedev] Lebedev AA. Semiconductors 33, p. 107 (1999)
- [Maximenko] Maximenko S I, and Sudarshan T S, J. Appl. Phys. 97, p. 074501 (2005)
- [Millman] Millman J, Grabel A. *Microelectronics*. Mc Graw-Hill , New York (1987).
- [Mitra] Mitra S, Rao MV, Papanicolaou N, Jones K, Derenge M, Holland OW., J Appl Phys, 1 p. 69 (2000)
- [Moscatelli] F. Moscatelli *et al.*, Proceedings of the ECSCRM 2002
- [Negoro] Negro Y, Kimono T, Miyamoto N, Matsunami H, Appl Phys Lett 80 p. 240 (2002)
- [Ohno] Ohno T, Kobayashi N, J appl Phys 89 (2001)
- [Ottaviani] Ottaviani L *et al.*, Appl Surf Sci, 184, p. 330 (2001)
- [Pécs] Pécs B, Appl Surf Sci 184 p.287 (2001)

- [Peréz] Peréz R, Ph. D. thesis
- [Poggi2002] Poggi A, Nipoti R, Cardinali G C and Moscatelli F: Mat. Sci. Forum, 433-436, p. 621 (2003)
- [Poggi2004] Poggi A, Nipoti R, Moscatelli F, Cardinali GC, Canino M. Mat Sci Forum, 457-460 p. 945 (2004)
- [Poggi2006] Poggi A, Nipoti R, Bergamini F, Solmi S, Canino M and Carnera A, Appl. Phys. Lett. 88, p. 162106 (2006)
- [Raineri] Raineri V, Calcagno L, Giannazzo F, Goghero D, Musumeci F, Roccaforte F and La Via F, Mat Sci Forum, 433-436, p. 375 (2003)
- [Rao] Rao MV. Solid-state Electronics, 47 p.213 (2003)
- [Roccaforte] Roccaforte F *et al.*, Appl Surf Sci, 184, p. 295 (2001)
- [Ruff] Ruff M, Mitlehner H, Helbig R, Trans. Electron Devices, 41, p. 1040 (1994)
- [Rybicki] Rybicki GC., J Appl Phys, 78, p. 2996 (1995)
- [Schaffer] Schaffer WJ, Negley CH, Irvine KG, Palmour JW, Mat Res Soc Symp vol. 339, p.595 (1994)
- [Schaffer-2] Schaffer WJ, Kong HS, Negley CH, Palmour JW, Inst. Phys. Conf. Ser. vol 137 p.155 (1994)
- [Soncini] G. Soncini. *Tecnologie microelettroniche*. Boringhieri (1986)
- [Svensson] Svensson BG et al., Mat Sci. Forum 527-529 pp. 781 (2006)
- [Sze] Sze S M *Physics of semiconductor devices* Wiley, New York (1969)
- [Sze-2] ] Sze S M *Semiconductor device Physics and technologys* Wiley, New York (1985)
- [w-colorado] [www.colorado.edu/~bart/book](http://www.colorado.edu/~bart/book)
- [w-cree] [www.cree.com](http://www.cree.com)
- [w-ntmdt] [http://www.ntmdt.ru/SPM-Techniques/Principles/AFM/Many-pass\\_techniques/Scanning\\_Capacitance\\_Microscopy\\_mode48.html](http://www.ntmdt.ru/SPM-Techniques/Principles/AFM/Many-pass_techniques/Scanning_Capacitance_Microscopy_mode48.html)
- [w-oist] <http://ois.nist.gov/nistpubs/technipubs/recent/search.cfm?dbibid=17725>
- [Wong] Wong-Leung J, Janson M S and Svensson B G, J. Appl. Phys. 93, p. 8914 (2003)
- [Baliga] Baliga B J, *IEEE Electron Device Lett.*, 10 455 (1989)
- [w-srim] [www.srim.org](http://www.srim.org)
- [Ziegler1985] J.F. Ziegler, J.P. Biersack and U. Littmark, *The stopping power and ranges of ion matter*, Pergamon Press, New York, (1985)

[Ziegler1992] J.F. Ziegler, *Handbook of ion implantation technology*,  
*North Holland*, Amsterdam (1992)

## List of publications by the author

### **Analysis of the electrical activation of P<sup>+</sup> implanted layers as a function of the heating rate of the annealing process**

M. Canino, F. Giannazzo, F. Roccaforte, A. Poggi, S. Solmi, V. Raineri, R. Nipoti 4-7 Sept 2006, Newcastle upon Tyne, UK  
Postre presentation at the VI ESCSRM,

### **Ion implanted p<sup>+</sup>/n 4H-SiC junctions: effect of the heating velocity on the post implantation annealing**

R. Nipoti, A. Carnera, M. Canino, A. Poggi, F. Bergamini, S. Solmi, M. Passini  
Mater. Res. Soc. Symp. Proc. Vol. 911 (2006)

### **Effects of heating ramp rates on the characteristics of Al implanted 4H-SiC junctions**

A. Poggi, F. Bergamini, R. Nipoti, S. Solmi, M. Canino, A. Carnera  
Applied Physics Letters 88 (2006) 162106

### **Correlation between current transport and defects in n<sup>+</sup>/p 6H-SiC diodes**

M. Canino, A. Castaldini, A. Cavallini, F. Moscatelli, R. Nipoti, A. Poggi  
Materials Science Forum, Vols. 527-529 (2006) pp.811-814  
Poster presentation at the X ICSCRM, 27-23 Sept. 2005, Pittsburgh, Pennsylvania

### **Current analysis of ion implanted and not terminated p<sup>+</sup>/n 4H-SiC junctions: post-implantation annealing in Ar ambient**

R. Nipoti, F. Bergamini, F. Moscatelli, A. Poggi, M. Canino, G. Bertuccio  
Materials Science Forum, Vols. 527-529 (2006) pp.815-818

### **Ar Annealing at 1600°C and 1650°C of Al<sup>+</sup> Implanted p<sup>+</sup>/n 4H-SiC Diodes: Analysis of the J-V Characteristics Versus Annealing Temperature**

F. Bergamini, F. Moscatelli, M. Canino, A. Poggi, R. Nipoti  
Materials Science Forum, Vols. 483-485 (2005) pp.625-628

### **n<sup>+</sup>/p diodes Realized in SiC by 300°C Phosphorus ion implantation: electrical characterizazion as a function of temperature**

M. Canino, A. Castaldini, A. Cavallini, F. Moscatelli, R. Nipoti, A. Poggi  
Materials Science Forum, Vols. 483-485 (2005) pp.649-652  
Poster presentation at the V ECSCRM, 2-6 Sept. 2004, Bologna, Italy

**Ni-Silicide contacts to 6H-SiC: contact resistivity and barrier height on ion implanted n-type and barrier height on p-type epilayer**

F. Moscatelli, A. Scorzoni, A. Poggi, M. Canino, R. Nipoti  
Materials Science Forum, Vols. 483-485 (2005) pp.737-740

**SiC donor doping by 300°C Phosphorus implantation: characterization of the doped layer properties in dependence of the post-implantation annealing temperature**

A. Poggi, R. Nipoti, F. Moscatelli, G. C. Cardinali, M. Canino  
Materials Science Forum, Vols. 457-460 (2004) pp.945-948